Università Campus Bio-Medico di Roma
School of Engineering

PhD Course in Biomedical Engineering
(XXIV - 2009/2011)

pHRI in Assistive and Rehabilitation Robots: Neural Constraints and Compliant Joints/Actuators Design

Nevio Luigi Tagliamonte

Supervisors
Prof. Eugenio Guglielmelli
Dr. Dino Accoto

PhD Program Coordinator
Prof. Giulio Iannello

March 2012

pHRI in Assistive and Rehabilitation Robots: Neural Constraints and Compliant Joints/Actuators Design

A thesis presented by

Nevio Luigi Tagliamonte

in partial fulfillment of the requirements for the degree of

Doctor of Philosophy

in Biomedical Engineering

Università Campus Bio-Medico di Roma

School of Engineering

Supervisors

Prof. Eugenio Guglielmelli

Dr. Dino Accoto

PhD Program Coordinator

Prof. Giulio Iannello

March 2012

Committee:

Prof. Giulio Iannello (Università Campus Bio-Medico di Roma)

Prof. Riccardo Pietrabissa (Politecnico di Milano)

Prof. Salvatore Andrea Sciuto (Università degli studi ROMA TRE)

Reviewer:

Prof. Hermano Igo Krebs (Massachusetts Institute of Technology)

To my parents and my sister

Abstract

The development of robotic systems for physical Human-Robot Interaction (pHRI) in rehabilitation and assistive applications demands advanced solutions in terms of mechanical structure, actuation system and control strategies to face several issues such as safety, dynamical adaptability and biomechanical compatibility.

To cope with the complex features of the human body and of the neural adaptation mechanisms, one should ideally be capable of *designing the interaction*, i.e. of introducing external artifacts effectively providing the desired assistance while optimally interacting with the user. Successful designs can be pursued if neural mechanisms underlying human motor control are understood and if proper components are embedded in the robotic artifacts to enhance intrinsic dynamics: on the one hand the features of physiological motion and neuromotor strategies adopted to perform motor tasks have not to be hindered; on the other hand, body dynamics can be supplemented and enriched by external agents making desired complex behaviors emerge as a form of *constructive perturbation*.

This thesis contributes to the improvement of pHRI in the design of assistive and rehabilitation robots with respect to these two research fields.

The topic of human intrinsic motor strategies and possible influence of robots perturbations is addressed presenting a work on human wrist movements during kinematically redundant pointing tasks in free motion

and during interaction with a state-of-the-art robot for post-stroke neurorehabilitation. Starting from the demonstration that human natural motion is perturbed by the robot during assessment, the effects of system mechanical impedance reduction are analyzed, using a direct force control scheme to minimize human-robot interaction forces. The work demonstrates the possibility of using a simple control approach to cope with neural strategies in performing motor tasks, which are not properly taken into account in current design of rehabilitation robots.

The topic of robots designs leveraging potentialities of intrinsic structural properties is addressed starting from the analysis of double actuation compliant systems used to vary impedance in different application fields. A classification and a critical comparison of possible architectures are carried out to provide guidelines for future designs of actuators. On this basis, a new actuation system, Variable Impedance Differential Actuator (VIDA), is proposed: an electromechanical model of the actuator is developed and performances are evaluated in simulations. A compact rotary Series Elastic Actuator (SEA), suitable to be used in wearable robotics applications, is also presented. Components are described and experimental characterization of prototypes, in terms of torque-angle characteristic of the elastic element and of torque/impedance control schemes, are reported. Moreover, a purely mechanical rotary passive ViscoElastic Joint (pVEJ) is presented. It includes two functionally distinct submodules, a torsion spring and a torsion damper connected in parallel. The modularity of the system allows to have a generic stiffness-angle characteristics by substituting a single component. Damping coefficient can be regulated through a valve. Characterization of the developed prototype using a custom dynamometric test-bed is reported. The active and passive joints developed and tested within this work are suitable to be included in assistive robots to exploit properties of passive low-impedance components.

Acknowledgments

I want to express my gratitude to all people who supported me in facing all the difficulties encountered during these three years of PhD research, with scientific, practical and personal contributions.

First of all, I want to thank Prof. Eugenio Guglielmelli for providing me the possibility of working on very interesting topics in the field of rehabilitation and assistive robotics, and of experiencing highly formative research opportunities. Many thanks also to Dr. Dino Accoto for his precious daily scientific and personal support, for revising my work and for continuously putting his trust in me. Thanks to my colleagues and friends Fabrizio Sergi and Giorgio Carpino, with whom I stood shoulder to shoulder for three years, sharing happiness and troubles.

I owe thanks to Dr. Domenico Formica for providing me many answers to many questions and for supervising me in the work with the wrist robot, together with Dr. Domenico Campolo, whose advice was always fundamental. Thanks also to Maria Scorcia for her help with experimental tests.

Many thanks to Prof. Auke Jan Ijspeert, who hosted me for three months in the Laboratory of Bioinspired Robotics (BioRob) of the École Polytechnique Fédérale de Lausanne (EPFL) and who supervised me in a very qualified, professional and kind manner. Thanks also to people at BioRob, especially Massimo Vespignani, Jesse van den Kieboom, Konstantinos Karakasiliotis and Alessandro Crespi.

Thanks to all the people in the Laboratory of Biomedical Robotics and Biomicrosystems, in particular to Antonella Benvenuto, Maria Teresa Francomano, Eugenia Papaleo and Fabrizio Taffoni, for their friendly and trustful moral support, to Alessandro Zompanti for his photos, and to Flavia Salvadori for the help in all

administrative and bureaucratic matters.

I also want to thank my colleagues and friends who shared with me these years of PhD researches: Antonino Salerno, Sara Maria Giannitelli, Liliana Liverani and Alessio Gizzi.

My heartfelt thanks go to my 'brothers' Gerardo and Antonio, whose support was just unmeasurable. I am also grateful for the affection of many true friends: Annalisa, Daniele, Davide, Francesco, Girolamo, Valentina, and Libera, Michela, Antonella and Diego, Francesco, Gaetano, Giovanni, Rosario. Warm thanks to Sabrina, who strongly and affectionately helped me to face the difficulties of these last months, and who always showed enthusiasm and appreciation for my work.

I am grateful to my family and, in particular, to my parents and my sister who expressed their love in continuously encouraging and supporting me in all possible ways. I hope I could made them proud of me.

Nevio Luigi Tagliamonte
Rome, March 2012

Contents

Nevio Luigi Tagliamonte

Nevio Luigi Tagliamonte

Nevio Luigi Tagliamonte

List of Tables

Nevio Luigi Tagliamonte

List of Figures

Nevio Luigi Tagliamonte

Nevio Luigi Tagliamonte

Nevio Luigi Tagliamonte

Nevio Luigi Tagliamonte

Nevio Luigi Tagliamonte

List of Acronyms

AA	Adduction/Abduction
ACSEA	Adjustable Compliant Series Elastic Actuator
AE	Absolute Encoder
AMASC	Actuator with Mechanically Adjustable Series Compliance
ANLES	Actuator with Non-Linear Elastic System
ASD-Mechanism	Adjustable Stiffness and Damping Mechanism
AwAS	Actuator with Adjustable Stiffness
CAN	Controller Area Network
CPT	Counts Per Turn
CS	Circular Spline
DAJ	Double Actuator Joint
DEA	Differential Elastic Actuator
DECMMA	Distributed Elastically Coupled Macro-Mini Parallel Actuator
Dm	Damping module
DM^2	Distributed Macro-Mini
DOF	Degree Of Freedom
EOM	Extra Ocular Muscle
ER	ElectroRheological
FC	Force-Controlled robot
FE	Flexion/Extension
FEM	Finite Element Method

FPGA	Filed Programmable Gate Array
FS	Flexible Spline
FSJ	Floating Spring Joint
HD	Harmonic Drive
HDAU	Hybrid-type Dual Actuation Unit
HH	HandHeld device
IE	Incremental Encoder
IR	Impedance Regulator
KTM	Kinematic Transmission Mechanism
LASAT	Linear Adjustable Stiffness Artificial Tendon
LOPES	Lower extremity Powered ExoSkeleton
MIA	Mechanical Impedance Adjuster
MACCEPA	Compliance and Controllable Equilibrium Position Actuator
MESTRAN	MEchanism for varying Stiffness via changing TRasmission ANgle
MR	MagnetoRheological
MVS	Modular Variable Stiffness
NI	National Instruments
PA	Position Actuator
PaCMMA	Parallel-Coupled Micro-Macro Actuator
pHRI	physical Human-Robot Interaction
PPAM	Pleated Pneumatic Artificial Muscle
PR	Position Regulator
PS	Pronation/Supination
pVEJ	passive ViscoElastic Joint
QA-Joint	Quasi Antagonistic Joint
RD-Joint	Redundant Drive Joint
RMS	Root Mean Square
SADU	Serial-type Dual Actuator Unit
SCA	Series Clutch Actuator

SEA	Series Elastic Actuator
SISO	Single-Input-Single-Output
Sm	Stiffness module
SM	Stiffness Modulator
SMA	Shape Memory Alloy
UR	Unpowered Robot
VIA	Variable Impedance Actuator
VIDA	Variable Impedance Differential Actuator
VIJ	Variable Impedance Joint
VPDA	Variable Physical Damping Actuator
VSA	Variable Stiffness Actuator
VSJ	Variable Stiffness Joint
VS-Joint	Variable Stiffness Joint
VSM	Variable Stiffness Mechanism
WG	Wave Generator
WEDM	Wired Electrical Discharge Machining
ZPD	Zero gains PD control

Chapter 1

Introduction

Traditional applications for robotics in industrial structured environment have experienced in the last twenty years a drastic extension to human domain, demanding safety and adaptability to many different interaction modalities rather than high accuracy, power and repeatability.

Machines for physical assistance to humans are sought to reduce fatigue and stress, increase human capabilities, substitute lost motor functions, supply physical rehabilitation therapy, thus generally improving the quality of life, especially in the contemporary context of 'ageing societies'. Due to the need of a safe and effective physical Human-Robot Interaction (pHRI), many design challenges arise from both mechanical, sensors and control standpoints.

Rehabilitation robotics aims at developing devices for assisted motor therapy and functional assessment of patients with reduced physical and/or cognitive abilities. They are intended as therapeutic tools for temporary use and are designed to maximize the clinical effectiveness of the therapy, improving both patients' functional recovery and efficiency of the entire clinical process.

The increasingly diffusion of robotics in the area of rehabilitation medicine is due to: *i)* the necessity of objective evaluation and quantitative comparative analysis of the impact of different therapeutic approaches. In this sense robotics technology provides tools for assessing human behavior which are much more accurate, precise, and repetitive than simple human observer's capabilities. This is of crucial importance

for enabling appropriate diagnoses, corrections of clinical strategies, and for identifying indicators of the recovery process; *ii)* the need to take over some of physically demanding tasks performed by healthcare operators, especially in the case of severely disabled patients who need strong physical assistance even in simple exercises. The use of robotic systems can allow physical therapists to mainly concentrate on the quality of the delivered therapy, also possibly supervising multiple subjects, and/or increasing the duration and the frequency of the exercise sessions; *iii)* the possibility of optimizing patient's functional recovery exploiting neural reorganization processes (*neuroplasticity*) if activity-dependent rehabilitation therapy is imparted, involving execution of goal-directed and repetitive exercises with some pre-defined constraints. In particular, the active role of the patient permits the whole sensorimotor coordination system to be stimulated and trained, including high-level brain functionality (i.e. imagination, planning, and anticipation of motor actions). In this perspective, rehabilitation robots provide the patient with the minimum level of physical and/or cognitive support needed to start, execute, and complete a prescribed task, while complying with some imposed temporo-spatial constraints.

Assistive robotics aims at developing solutions for promoting independent living of people suffering from developmental, cognitive and physical disabilities or simply from age-related neuromotor decay, by providing the required support for daily task-related activities, e.g. in manipulation and/or locomotion applications. Assistive robots have to be used in a lifelong perspective so they need to be minimally obtrusive and highly acceptable in daily life scenarios. Moreover, a high level adaptability to a wide range of operative conditions is needed: e.g. adaptation to different objects, tasks, environments in robotic devices for manipulation (external arms or active prostheses) or adaptation to several dynamical conditions during locomotion in mobility aids (starting, stopping, velocity changing, stairs climbing, sitting, etc.). In all these cases user's state, activity and intention have to be detected and a flexible, personalized assistance has to be provided, still guaranteeing the necessary power support for tasks completion. These aspects are critical especially in the case of wearable robots, i.e. active orthoses, typically with anthropomorphic features, which are worn by the user and operate alongside human limbs. In particular, gait assistance

wearable robots have to cope with the highly complex dynamics of walking, and with requirements posed by wearability (compact and lightweight design, adjustability to different individuals) and actuation systems performances (high torque- and power-to-mass ratio).

It is evident that the presented robots operate in continuous physical interaction with the human body. For this reason major design challenges are posed not only by the need for an extreme level of safety and dependability, but also by the necessity of harmonizing robot action in constrained motion with users, adapting it in a highly flexible fashion to human dynamically varying behavior.

Assistive and rehabilitation robots typically have to implement 'assistance as needed' strategies, so to compensate for subjects motor insufficiencies only when necessary and, in case of rehabilitation, still promoting their active role to properly stimulate the whole set of sensorimotor control functionalities. Motor training sometimes requires to challenge the patient through haptic interaction, using timely- and/or spatially-varying force fields for opposing or favoring motion in predefined directions. On the other hand, robots are required to be fully transparent to the subject motion when he is capable of executing a task or when his motion parameters have to be assessed excluding as much as possible perturbations to physiological behavior.

The complex nature of the presented pHRI aspects poses major technical challenges in the design of rehabilitation and assistive robots.

To cope with features of the human body and of the neural adaptation mechanisms, high dynamical adaptability is required. The potentialities of biomechatronic approach can be exploited to design harmonically both mechanical structures and elaborate interaction control schemes. In a way, once fixed the user characteristics and a predefined physiological behavior to be achieved, one should be ideally able to *design the interaction*, i.e. to introduce an external artifact effectively providing the desired assistance or therapeutic support while optimally interacting with the user: on the one hand intrinsic features of physiological motion and neuromotor strategies adopted by the brain during motor tasks have not to be perturbed by the machine; on the other hand, body dynamics can be supplemented and enriched by external

agents giving rise to desired complex behaviors.

These two aspects of robots design further enlarge the well established focuses on biomechanical and kinematic compatibility which have been and are being widely investigated in current research. Fig. 1.1 schematically reports the contributions that these two particular research aspects can provide to current methodologies for the optimization of pHRI in assistive and rehabilitation robotics.

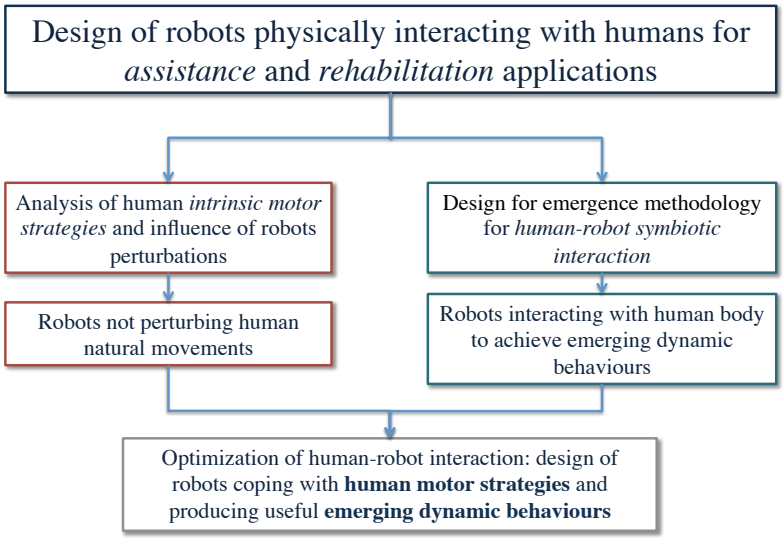

Figure 1.1: Complementary design aspects for the optimization of pHRI in assistive and rehabilitation robots: minimization of robots perturbation to human intrinsic neuromotor strategies and exploitation of structural embodied intelligence to elicit emerging dynamic behaviors.

Analysis of human intrinsic motor strategies and influence of robots perturbations. Recent research on human limbs movements showed that besides 'hard', *biomechanical constraints*, the design of robots physically interacting with humans should also consider 'soft', *neural constraints*, which are adopted by the brain to solve redundancy in motor tasks and to achieve motor efficiency [1, 2, 3]. Neural control underlying complex motor tasks is sometimes not completely understood, even though it may represent a crucial parameter to be taken into account in the design of systems that intimately interact with human agents. In this sense,

the analysis of human intrinsic motor control strategies (e.g. while handling kinematic redundancy) and of possible robots perturbations are fundamental to define guidelines for the design of systems minimally hindering users' natural motion.

Design for emergence methodology for robots with embodied intelligence. Works in the field of walking bipedal robots demonstrated the possibility of greatly simplifying the achievement of desired gait behaviors when mechanical structure is endowed with proper intrinsic dynamics (passive and pseudo-passive walkers) [4]. With the same approach, a novel design method for rehabilitation and assistive machines is based on the idea of exploiting *structural embodied intelligence* [5], i.e. of embedding some opportune mechanical properties so that the intrinsic human-robot coupling can elicit a target physiological movement as an *emerging dynamic behavior*. This design process is expected to lead to novel concepts of robots allowing *i)* high level of adaptability to the action of different users due to the flexibility of simple control schemes, *ii)* natural and smooth (even *symbiotic*) interaction with humans due to the exploitation of structural embodied intelligence, *iii)* energetic efficiency due to the optimal allocation of passive dynamics and possibly to human-robot energy bouncing, and *iv)* improved ergonomics due to the advantages of possible non-anthropomorphic solutions in terms of kinematic compatibility (minimization of macro/micro misalignments between robot and human joints).

As it can be noticed, one approach proposes the minimization of interference to human neuromotor strategies as the deepest and most effective form of adaptation, while the other one deliberately tries to introduce a *constructive perturbation* to human body dynamics with the aim of improving the properties of the compound human-robot dynamical system. From a proper combination of these two apparently conflicting aspects, an optimal pHRI is expected to be attained, giving rise to a new generation of machines in the next future.

A common trait that can be found in robots coping with human motor strategies and producing useful emerging dynamic behavior is represented by control schemes which are not based on rigid position regulations (as for traditional high bandwidth and high precision industrial robots), but rather on interaction force modulation.

The most conventional approaches used to directly or indirectly achieve force control are: *i) explicit* (or *direct*) *force control* [6], that generates a force servo: the controller input is directly the error between the desired force and the actual measured one and typically without any positional feedback; *ii) stiffness control* [7] and *damping control* [7], that create a virtual spring or damper around an equilibrium position. Both techniques measure positions and velocities in order to generate a desired force output related to the virtual spring or damper; *iii) impedance control* [8], generalizes the ideas of stiffness and damping controls. The position and velocity of the robot are commanded to follow some trajectory and the control system modulates robot behavior as a visco-elastic or as a second-order system (if also virtual inertial contribution is added). Control gains which set the virtual stiffness, damping (and inertia) of the robot correlate directly with stability and bandwidth limitations; *iv) hybrid position/force control* [9], that combines conventional position control with force control: the environment dictates natural constraints (e.g. contact with an obstacle) where only force control is used, while position control is employed in non-constrained directions, where the robot can move freely. More sophisticated control algorithms can basically be seen as an evolution of these basic schemes.

Beside active control approaches where rigid actuator are commanded to directly or indirectly regulate interaction forces, current research is moving towards the introduction of intrinsic compliant elements in robotic systems. The presence of elastic components allows simple adaptation to external agents and, with proper design, energy storage and stabilization capabilities. The trend of *soft robotics*, i.e. of human-friendly systems which intrinsically behaves compliantly, is undergoing a rapid diffusion and a number of actuators and/or passive joints for different applications are being developed. These systems provide the possibility of implementing direct/indirect force control schemes when fixed compliance is used (which lower actuator impedance and allows estimating interaction forces measuring passive deflection of soft elements), or the possibility of physically regulating the joints properties when variable impedance actuators are employed. The use of physical springs and dampers can be particularly useful in the design of actuators and joints of robots with embodied intelligence, since energy bouncing between the human body, the

robot and the external environment can be exploited.

1.1 Objectives and main contributions

The goal of this thesis is to contribute to the improvement of pHRI in the design of assistive and rehabilitation robots, with respect to the aforementioned research areas.

The topic of human intrinsic motor strategies and influence of robots perturbations will be addressed presenting a work on human wrist movements during kinematically redundant pointing tasks in free motion and during interaction with a state-of-the-art rehabilitation robot. Main contributions regarding this study are:

- Estimation of dynamical properties of the InMotion^3 wrist rehabilitation robot to compensate for friction, inertial and gravitational effects;

- Calculation of kinematic operators fro the InMotion^3 system for joints space control (Jacobian matrix, adjoint transformation, etc.);

- Implementation and validation of a direct force control scheme on the InMotion^3 robot to improve transparency during assessment mode;

- Analysis of wrist kinematics and human motor strategies during pointing tasks in three operative conditions: *i)* free motion, using magneto-inertial sensors; *ii)* interaction with the robot controlled through its native impedance controller; *ii)* interaction with force-controlled robot.

This work demonstrates the possibility of using a simple control approach to cope with neural strategies in performing motor tasks, which are not properly taken into account in current design of rehabilitation robots.

The topic of robots leveraging potentialities of structural embodied intelligence will be addressed presenting the design and characterization of compliant components (actuators and passive joints) suitable to be used in lower limbs wearable robots. Main contributions regarding these studies are:

- Analysis, classification and critical comparison of state-of-the-art compliant actuator based on double actuation architectures;
- Model and control of Variable Impedance Differential Actuator (VIDA) suitable to independently regulate position and impedance;
- Design, control and experimental characterization of a rotary Series Elastic Actuator (SEA);
- Design and experimental characterization of a passive ViscoElastic Joint (pVEJ).

In these works guidelines on variable impedance actuators properties are introduced, based on their classification and comparative analysis, and new compact compliant active and passive joints have been developed and tested to be used in wearable robotics applications.

The following section is meant to be an outline of this dissertation and of the aforementioned aspects, which will be examined in detail in the next chapters.

1.2 Thesis overview

This thesis is divided in two parts. Part I (*pHRI during wrist pointing tasks: effects on human intrinsic motor strategies*), includes:

Chapter 2 – Impedance reduction of a robot for wrist rehabilitation This chapter deals with the analysis of human wrist kinematics during pointing tasks. Starting from the demonstration that human motor strategies are perturbed during the interaction with a highly back-drivable state-of-the-art rehabilitation robot in assessment mode, the effects of mechanical impedance reduction for the pronation/supination joint are analyzed. To this end a basic force control scheme is deployed, in order to minimize human-robot interaction force and to make the robot transparently follow user motion. To assess the effects on human motor strategies, pointing tasks are performed by three subjects with a lightweight handheld device, interacting with the robot using its native controller (setting desired impedance to zero) and with the force-controlled robot. Human motion features are quantified

using two-dimensional surfaces in the three-dimensional configuration space of rotations. Results reveal that the subject-specific characteristic strategies can reappear after the reduction of robot impedance.

Part II (*Compliant actuators and joints for pHRI: analysis and new designs*), includes:

Chapter 3 – Double actuation architectures This chapter analyzes different application fields where compliant actuation is employed and it examines architectures involving two active elements and passive elastic components for separate position and impedance regulations of one actuated degree of freedom. Based on state-of-the-art solutions, the chapter evaluates the possible configurations of rotary double actuation systems classifying them in three main categories. A critical and comparative analysis of the their most relevant features is carried out, also describing representative prototypes. Recently proposed methodologies and evaluation criteria for design optimization are illustrated and perspectives on potential applications of double actuation architectures are presented. On this basis a new actuation system is proposed, Variable Impedance Differential Actuator (VIDA) which is intended for wearable robotics applications. It separately controls output position and mechanical impedance and includes an impedance-controlled rotary Series Elastic Actuator and a simple brushless DC motor connected through a Harmonic Drive in a differential configuration. An electromechanical model of the system is developed and two control schemes for separate position and impedance regulations are implemented on the two active input shafts. Performances of the actuator are evaluated in simulations.

Chapter 4 – Design, control and characterization of a rotary Series Elastic Actuator This chapter presents a compact rotary Series Elastic Actuator (SEA). The system includes a flat brushless DC motor, a Harmonic Drive gear and a custom-made compact torsion spring designed and optimized by means of an iterative FEM simulations-based process. A velocity-sourced type torque control scheme is implemented on the actuator and a cascaded impedance controller is employed on top of that. Characterization of torque-angle characteristic of the elastic element is per-

formed to achieve an accurate estimation of the torque delivered by the actuator and a high fidelity torque control. Performances of the prototype in terms of the torque control bandwidth and of impedance regulation are experimentally verified using a custom dynamometric test-bed and system identification techniques. System performance limitations can be overcome with a new design under development which is briefly presented at the end of the chapter together with some experimental tests on its elastic components.

Chapter 5 – Design and characterization of a passive Visco Elastic Joint
This chapter presents a purely mechanical rotary passive ViscoElastic Joint (pVEJ), including two functionally distinct sub-modules: a torsion spring and a torsion damper connected in parallel. The torsion stiffness module is implemented using linear compression springs connected between the joint shaft and rollers sliding on cam profiles. The modularity of the system allows to have constant, linear and quadratic stiffness-angle characteristics by using different cams. The damping module is implemented connecting the joint shaft to a roller compressing a tube filled with a viscous fluid. The rotation of the shaft produces the motion of the fluid in the tube. A localized pressure drop, obtained by partially closing a valve, causes viscous forces which result in a torque proportional to the angular velocity on the joint shaft. Characterization of the developed prototype using a custom dynamometric test-bed is reported.

Nevio Luigi Tagliamonte

Part I

pHRI during wrist pointing tasks: effects on human intrinsic motor strategies

Chapter 2

Impedance reduction of a robot for wrist rehabilitation

During traditional neurorehabilitation sessions the role of the patient is quite passive and the participation of the high-level structures of his nervous system are limited. On the other hand, robotic therapy allows subjects to perform active movements, thus promoting *neurogenesis* and *neuroplasticity*, and optimizing the functional recovery after neurological injuries [10, 11]. For this reason rehabilitation robotics has become an emerging field in recent years and the potentialities of robot-mediated motor therapy is being widely investigated [12, 13, 14, 15].

During therapy rehabilitation robots are meant to: *i)* provide assistance as needed, not to perturb voluntary movements, and to help completing tasks that patients are not able to perform autonomously; *ii)* apply, if required, resistive force fields to improve the efficacy of the treatment. During assessment robots have to be as transparent as possible in order to minimally interfere with human natural motor strategies. In this sense a high back-drivability, i.e. a low perceived mechanical impedance during user-driven motion, is of crucial importance. Therapy and assessment sessions can be interlaced, and assessment sessions may determine the amount of future treatment to be imparted thus they may also have an indirect impact on therapy. The technological choices regarding the design of mechanical structure and control strategies for this kind of robots have to face several issues, such as safety,

dynamical adaptability and biomechanical compatibility [16]. Nevertheless, besides biomechanical constraints, also the understanding of neural strategies behind human motor control (especially in presence of dynamic interactions) should be considered to define some indications for robots design.

In this regard, it has been shown that rehabilitation machines have to comply not only with 'hard' (*biomechanical*) constraints but also with 'soft' (*neural*) constraints [17], which are adopted by the brain to solve kinematic redundancy and to implement strategies for motor efficiency.

Studies on human motor control have demonstrated the existence of simplifying strategies adopted by the brain when dealing with kinematically redundant problems. Such strategies are often referred to as *Donders' law* or *Listing's law* for historical reasons, in relation to the early Donders' and Listing's studies on the eye movements. In a good approximation, the eye can be considered as a center-fixed sphere rotated by the action of 6 (i.e. 3 agonist/antagonist couples) Extra Ocular Muscles (EOMs). EOMs provide 3 DOFs kinematics allowing full mobility in the space of rigid body rotations with the only limitations given in terms of range of motion. When looking at some point in space, the gaze direction is fully determined but not the amount of ocular torsion about the line of sight. In other words, for a given line of sight, uncountably many eye configurations (torsions) exist which correspond to the same gaze direction.

In 1847, Donders experimentally found that for a given *steady* gaze direction there is only one eye configuration (*Donders' Law*) [1], i.e. physiological eye configurations are described by a 2-dimensional surface embedded into the 3-dimensional space of eye configurations: a solution to redundancy. Two decades later, Listing and Helmholtz determined that such a 2-dimensional surface is actually a plane: the eye assumes only those positions that can be reached from primary position by a single rotation about an axis in the *Listing's plane*, which lies orthogonal to the gaze direction in primary position (*Listing's Law*) [1]. Listing's law is therefore a particular form of a more general Donders' law: the former prescribes a plane whereas the latter prescribes a generic surface[1].

[1]Hereafter the term *Donders' law* will be generally used.

It had been debated for quite some time whether Donders' law was due to a biomechanical or a neural mechanism. It is now known that such a law holds during fixation, saccades, smooth pursuit, and vergence, but not during sleep and vestibulo-ocular reflex, suggesting that it is actively implemented by a neural mechanism [18]. Moreover, in the last two decades, Donders' law has been found to well apply to the head as well as to limb movements [2, 19].

Recent studies demonstrated that Donders' law applies also to wrist movements during pointing tasks (in which the three DOFs of the wrist are redundant) [3]. This study was conducted measuring wrist orientations during pointing movements using a lightweight *handheld* device, which introduces a negligible perturbation to the physiological movements. The three dimensional rotations vectors resulted well fitted by quadratic (Donders') surfaces, whose curvature expresses inter-subjects differences in motor strategies, thus denoting a personal 'style' in solving redundancy [3].

The same analysis was conducted in [17] with subjects performing similar pointing tasks while interacting with the InMotion^3 system (Interactive Motion Technologies Inc.), a the state-of-the-art robot for wrist neurorehabilitation. This system is specifically designed to comply with the biomechanical constraints providing a high level of back-drivability [20] and it is being successfully employed in post-stroke therapy.

In this case no statistically significant difference was found between subjects, suggesting that the robot, in assessment mode, flattens out any personal motor strategy; in particular, it was hypothesized that the impedance of the most proximal joint of the robot, responsible for Pronation/Supination (PS) movements, was not low enough to comply with the neural constraints. In other terms the robot perturbs voluntary movements of the subjects, despite its high level of transparency which copes with humans biomechanical features.

This result is in line with studies on motor control and robot-assisted neurorehabilitation, in which the influence of robots dynamics on human psychophysics was experienced. This can be basically imputed to the high sensitivity of the human motor control to external perturbations, which is due to sophisticated active and passive learning and adaptation mechanisms [21, 22, 23]. In this sense, it is impor-

tant to consider potential artifacts in measuring human natural motion when robotic platforms are employed. Indeed, as stated before, one of the most important design challenges relies in the simultaneous matching of both requirements on assistance and assessment (high deliverable forces and low perceived impedance).

In studies with the planar shoulder/elbow MIT-Manus system (InMotion^2, Interactive Motion Technologies Inc., [12]), for example, reliability issue is accurately taken into account and some opportune experimental expedients are typically adopted to avoid possible measurements artifacts due to the presence of the robotic structure.

The objective of this thesis is to analyze the effect of a reduced perceived impedance of the InMotion^3 system on human motor strategies during pointing tasks.

To this aim the handle of the robot was provided with a load cell and a basic force control scheme (with a null reference) was implemented to minimize the interaction force exerted by the user. This kind of approach has also been preliminary validated in [24] on the MIT-Manus system, in both simulation and experimental tests. In [24] a reduction of (mean and maximum) forces exerted by a subject during planar pointing tasks was verified in different operative conditions, demonstrating the effectiveness of the selected force control scheme in improving the system transparency.

In this thesis, friction and gravity effects have been estimated for the PS joint of the InMotion^3 system to be actively compensated for. The performance of the robot have been analyzed with and without the force control to verify the reduction of its mechanical impedance. Moreover, the reduction of forces/torques required to three healthy subjects to perform two different kinds of tasks (involving respectively 1 or 3 DOFs movements) has also been measured.

The effect of the reduced impedance of the robot on human motor strategies during 3-DOFs pointing tasks has been analyzed, by assessing wrist rotations of three healthy subjects in three different testing conditions: movements with *i)* the handheld device, *ii)* the robot with its standard PD control with gains set to zero and *iii)* the force-controlled robot; for each experiment Donders' surfaces were calculated as performance index.

Nevio Luigi Tagliamonte

2.1 InMotion^3 wrist robot

The InMotion^3 system [20] has three active DOFs: Pronation/Supination (PS), Abduction/Adduction (AA) and Flexion/Extension (FE). A differential mechanism is used to achieve AA and FE movements; PS rotations entail the sliding along a curve guide of the housing comprising the differential gearing and the AA and FE actuators (Fig. 2.1). In [20] a quantification of the three axis inertia, friction and gravity terms is provided showing that PS values are one order of magnitude higher with respect to the two other DOFs.

The robot is actuated by three DC motors which are equipped with rotary encoders; angle resolution measurement is 0.017 deg for the PS DOF and 0.026 deg for FE and AA DOFs.

At the basis of the handle two passive DOFs, a linear slider and a revolute joint, are used to comply with the anatomic characteristics of different subjects and also for a further adaptation of the robot to the axes of rotation of the human wrist (Fig. 2.1).

The robot is provided by the manufacturer with a PD plus gravity compensation control scheme (which, for simplicity, will be referred as *PD control*) so to generate programmable viscoelastic torque fields to deliver forces or impart movements during therapy. In particular, it can be programmed to provide different levels of mechanical impedance by properly setting the control stiffness and damping parameters (details on the standard control of the InMotion^3 system can be found in [20]). The minimum impedance, with this control scheme, can be achieved when these parameters are both set to zero; in this case the only role of the motors is to compensate the gravity effects.

In this work we sensorized the robot handle, in order to implement a direct force control for a further reduction of the impedance of the robot PS joint. To this aim we decided to remove the linear slider and the passive revolute joint, whose movements could not be measured, and to mount a load cell at the basis of the end effector (Fig. 2.2).

A 6 axes JR3 torque/force sensor (20E12A4-I25-EF 100N5, JR3 Inc. - maximum force: 100 N; maximum torque: 5 N·m) with external electronics was used. The six

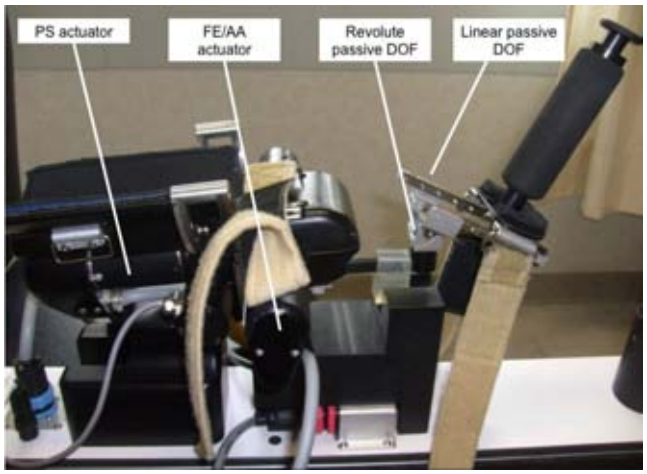

Figure 2.1: InMotion^3 wrist robot [20].

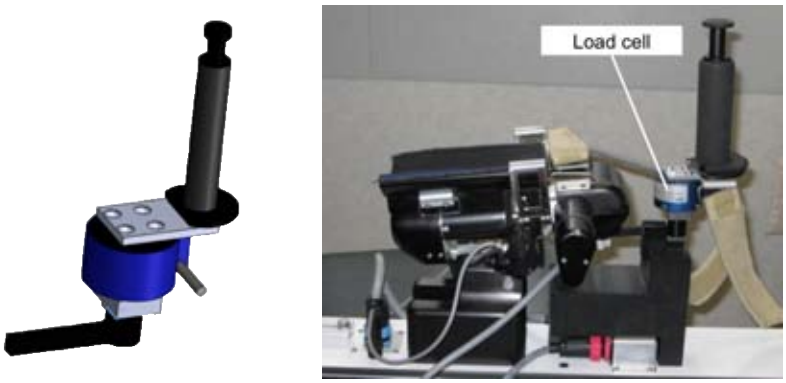

Figure 2.2: Integration of the force/torque sensor in the InMotion^3 system.

analog outputs of the sensor were directly connected to an acquisition board already present on the robot, which automatically synchronizes external signals with the 200 Hz control software. The sampled signals have been multiplied by a calibration and decoupling matrix, provided by the manufacturer of the sensor.

2.2 Force control implementation

The control algorithm used in this work is adapted from [25, 26]. It compensates robot dynamics (gravity, inertia and friction) and minimizes the end-point interaction force since a zero reference is imposed.

The equation of robot dynamics[2] can be expressed as:

$$\boldsymbol{B}(\boldsymbol{q})\ddot{\boldsymbol{q}} + \boldsymbol{b}\dot{\boldsymbol{q}} + \boldsymbol{g}(\boldsymbol{q}) = \boldsymbol{\tau} - \boldsymbol{J}^T(\boldsymbol{q})\boldsymbol{F}_{int} \tag{2.1}$$

where $\boldsymbol{F}_{int}$ represents the 6×1 vector of the generalized forces exerted by the user (with respect to the base frame), $\boldsymbol{b}$ is a 3×3 diagonal matrix of constant friction coefficients, $\boldsymbol{B}(\boldsymbol{q})$ is the 3×3 inertia matrix, $\boldsymbol{J}^T(\boldsymbol{q})$ is the 3×6 transpose Jacobian matrix, $\boldsymbol{g}(\boldsymbol{q})$ is the 3×1 gravity term and $\boldsymbol{\tau}$ is the 3×1 vector of control torques. Relation (2.1) is composed by three scalar equations, which refer to PS, AA and FE joints respectively; thus the vector of joint coordinates is $\boldsymbol{q} = [q_{PS}\ q_{AA}\ q_{FE}]^T$.

The implemented control law is:

$$\boldsymbol{\tau} = \hat{\boldsymbol{b}}\dot{\boldsymbol{q}} + \hat{\boldsymbol{g}}(\boldsymbol{q}) + \boldsymbol{J}^T(\boldsymbol{q})\boldsymbol{F}_{int} + \hat{\boldsymbol{B}}(\boldsymbol{q})\boldsymbol{K}_P\boldsymbol{J}^T(\boldsymbol{q})(\boldsymbol{F}_d - \boldsymbol{F}_{int}) \tag{2.2}$$

where the symbol ˆ indicates an estimation of the corresponding vector or matrix, $\boldsymbol{F}_{int}$ indicates the 6×1 vector of generalized forces measured by the load cell and $\boldsymbol{K_P}$ is a 3×3 positive-definite diagonal gain matrix.

A block scheme of control law in (2.2) is presented in Fig. 2.3.

Force error can be indicated as $\boldsymbol{e}_f = \boldsymbol{J}^T(\boldsymbol{q})(\boldsymbol{F}_d - \boldsymbol{F}_{int})$, where $\boldsymbol{F}_d$ is the desired interaction force. By substituting (2.2) in (2.1), and assuming that robot dynamics are perfectly estimated, the force error dynamics becomes:

$$\boldsymbol{e}_f = \boldsymbol{K}_P^{-1}\ddot{\boldsymbol{q}} \tag{2.3}$$

Considering $\boldsymbol{M} = \boldsymbol{K}_P^{-1}$, equation (2.17) can be expressed as:

$$\boldsymbol{e}_f = \boldsymbol{M}\ddot{\boldsymbol{q}} \tag{2.4}$$

[2]Coriolis and centrifugal effects have been neglected because of the low values of velocity involved in the wrist pointing tasks.

Nevio Luigi Tagliamonte

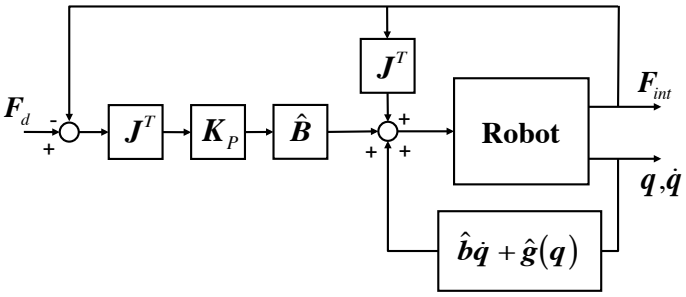

Figure 2.3: Block diagram of force control in (2.2); the 'Robot' block represents the first term of equation (2.1).

If $\boldsymbol{F}_d$ is set to zero, equation (2.4) indicates that the system behaves like a free body with mass $\boldsymbol{M}$, so that increasing proportional gain, within stability margins, will reduce the perceived inertia.

Force control in (2.2) has been implemented only for the PS joint since the AA and FE joints are already highly back-drivable (their mechanical impedance is one order of magnitude smaller than the one of PS DOF [20]); therefore, the control torques for the three DOFs can be written as follows:

$$\begin{cases} \tau_{PS} = \boldsymbol{\tau}[1\ 0\ 0]^T \\ \tau_{AA} = 0 \\ \tau_{FE} = 0 \end{cases} \tag{2.5}$$

with

$$\tau_{PS} = b_{PS}\dot{q}_{PS} + \tau^g_{PS} + [\boldsymbol{J}^T(\boldsymbol{q})\boldsymbol{F}_{int} + \hat{\boldsymbol{B}}(\boldsymbol{q})\boldsymbol{K}_P\boldsymbol{J}^T(\boldsymbol{q})(\boldsymbol{F}_d - \boldsymbol{F}_{int})][1\ 0\ 0]^T \tag{2.6}$$

where $\tau^g_{PS} = g_{PS}\sin(q_{PS})$ and b_{PS} are the gravity term and the viscous friction coefficient of the PS DOF, respectively.

Indicating for simplicity:

$$\tau^{int}_{PS} = [\boldsymbol{J}^T(\boldsymbol{q})\boldsymbol{F}_{int}][1\ 0\ 0]^T \tag{2.7}$$

and

Nevio Luigi Tagliamonte

$$\tau_{PS}^{fb} = \hat{\boldsymbol{B}}(\boldsymbol{q})\boldsymbol{K}_P\boldsymbol{J}^T(\boldsymbol{q})(\boldsymbol{F}_d - \boldsymbol{F}_{int})][1\ 0\ 0]^T \tag{2.8}$$

the final control torque for the PS DOF becomes:

$$\tau_{PS} = b_{PS}\dot{q}_{PS} + \tau_{PS}^{g} + \tau_{PS}^{int} + \tau_{PS}^{fb} \tag{2.9}$$

The implementation of the control scheme in (2.9) required the calculation of the robot kinematic operators and the estimation of its dynamical properties.

2.2.1 Robot kinematics

Since the robot native control is implemented only in the joint space, the calculation of the Jacobian matrix $\boldsymbol{J}(\boldsymbol{q})$, and of its transpose $\boldsymbol{J}^T(\boldsymbol{q})$, was necessary to map the torques/forces measured in the operative space in the corresponding actions on the joints. A schematic representation of the robot kinematics is provided in Fig. 2.4. In the figure and in this section a new notation is used for robot joint angles: $\boldsymbol{q} = [q_{PS}\ q_{AA}\ q_{FE}]^T \equiv [\mathrm{t}_1\ \mathrm{t}_2\ \mathrm{t}_3]^T$. Denavit-Hartenberg convention was used to select the frames of reference (the parameters are reported in Table 2.1) and to calculate the direct kinematics.

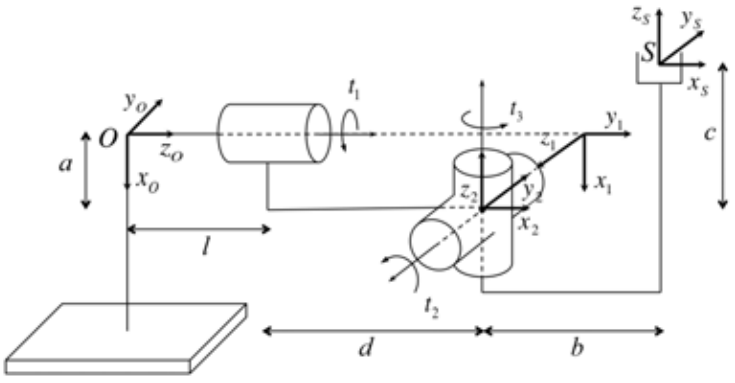

Figure 2.4: Schematic representation of the robot kinematics; frames of reference are selected using the Denavit-Hartenberg convention. The following quantities were measured: $a = 0.062$ m, $b = 0.158$ m, $c = 0.022$ m, $d = 0.120$ m, $l = 0.100$ m.

Nevio Luigi Tagliamonte

Table 2.1: Denavit-Hartenberg parameters for the kinematics of the InMotion^3 system.

Joint	a_i	d_i	α_i	θ_i
1	a	d	$-\pi/2$	t_1
2	0	0	$\pi/2$	t_2
3	b	c	0	t_3

The adjoint transformation [27] was used to map the vector of generalized forces from the the sensor coordinate frame (indicated with S in Fig. 2.4) to the global reference system (indicated with O in Fig. 2.4).
Let $\boldsymbol{p}_{os}$ be the 3×1 position vector of the origin of frame S from the origin of frame O and $\boldsymbol{R}_{os}$ the 3×3 rotation matrix describing the orientation of frame S with respect to frame O. This matrix is calculated as

$$\boldsymbol{R}_{os} = \boldsymbol{R}_{o1}(\mathrm{t}_1)\boldsymbol{R}_{12}(\mathrm{t}_2)\boldsymbol{R}_{2s}(\mathrm{t}_3) \tag{2.10}$$

being the $\boldsymbol{R}_{(\boldsymbol{i-1})\,\boldsymbol{i}}(\mathrm{t}_i)$ matrix associated with the i-th rotation of the i-th frame with respect to the $(i-1)$-th one. Rotation matrices $\boldsymbol{R}_{o1}(\mathrm{t}_1)$ and $\boldsymbol{R}_{2s}(\mathrm{t}_3)$ indicate the orientation of frame 1 with respect to frame O and of frame S with respect to frame 2 respectively.

Details about kinematics calculations are provided in appendix A.
Indicating with g_{os} the pair $(\boldsymbol{p}_{os}, \boldsymbol{R}_{os})$ the matrix

$$\boldsymbol{Ad}_{g_{os}} = \begin{bmatrix} \boldsymbol{R}_{os} & \boldsymbol{p}_{os} \wedge \boldsymbol{R}_{os} \\ \boldsymbol{0} & \boldsymbol{R}_{os} \end{bmatrix} \tag{2.11}$$

associated with g_{os} is the adjoint matrix; its transpose transforms force vectors from the frame S the frame O as follows:

$$\boldsymbol{F}_{int} = \boldsymbol{Ad}^T_{g_{os}} \boldsymbol{F}^S_{int} \tag{2.12}$$

It has been assumed that the vector without superscripts is referred to the base frame.

Nevio Luigi Tagliamonte

2.2.2 Robot dynamics

2.2.2.1 Gravity term estimation

To estimate the gravity term for the PS joint, a correlation between different static configurations and the torques required to hold the robot in those positions was performed.

It is important to note that tests were carried out with AA and FE joints locked, being the actuators commanded to maintain their 0 reference position through high gains PD position control (in these conditions we verified a deviation from the rest position of FE and AA of less than of 3 deg which does not sensibly affect the estimation). The choice of neglecting the contribution of changes in AA and FE configurations on the PS the gravity term is also adopted in [20] since the load produced by the handle on the PS joint is reasonably independent of the AA and FE orientations of the robot in the range of operation.

The robot was commanded to reach 10 positions (from -0.6 rad to $+0.6$ rad with respect to its rest position); PS actuator torques exerted to maintain these rotations in static conditions were evaluated. Fig. 2.5 shows an example of the PS torque and angle patterns during one estimation test of gravity term.

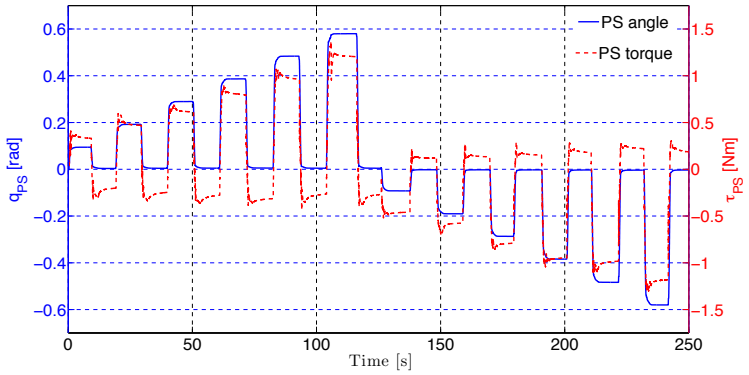

Figure 2.5: PS torque and angle patterns during one representative test for the gravity term estimation. Commanded angles varied from -0.6 rad to $+0.6$ rad with respect to the robot rest configuration.

As in [20] the gravity term has been assumed sinusoidally varying with PS angle. Therefore, a linear regression between PS torque and the sin of the PS rotation was

Nevio Luigi Tagliamonte

calculated for 5 trials. In Fig. 2.6 the collected data (static PS angles and torques for the 5 trials) are shown together with the best fitting curve.

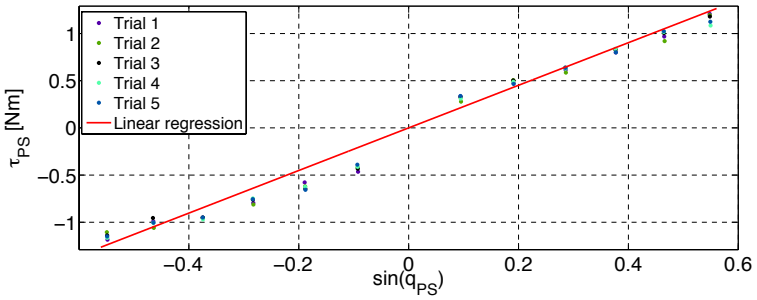

Figure 2.6: Linear regression between τ_{PS} and $\sin(q_{PS})$ static values for the estimation of the PS gravity term. The fitting curve slope is mediated on 5 trials. The resultant gravitational term is $\tau^g_{PS} = g_{PS}\sin(q_{PS}) = 2.254\sin(q_{PS})$.

The slope of the linear curve in Fig. 2.6, averaged on the 5 trials, was found to be $g_{PS} = 2.254 \pm 0.009$ N·m, with a mean R^2 of 0.980.

2.2.2.2 Inertia and friction estimation

To estimate inertia and friction terms the robot was manually back-driven performing few rapid oscillating movements. The PS motor compensated the gravity effect (on the basis of the estimation reported in section 2.2.2.1) and the AA and FE actuators were commanded to maintain their rest positions through high gains PD position control; in these conditions a deviation of less than 3 deg for FE and AA was found. Force/torques exerted on the handle were recorded and their effect on the PS joint was calculated as follows:

$$\tau^{PS}_{sens} = [\boldsymbol{J}(\boldsymbol{q})^T \boldsymbol{Ad}^T_{g_{os}} \boldsymbol{F}^S_{int}][1\ 0\ 0]^T \tag{2.13}$$

In Fig. 2.7 velocity and acceleration profiles for one representative trial are shown.

We estimated the inertia and friction terms for the PS joint by regressing the τ^{PS}_{sens} reported in (2.13) with angular velocities and accelerations of the PS DOF, as reported in the following equation:

$$\tau^{PS}_{sens} = \tau^{PS}_0 + b_{PS}\dot{q}_{PS} + B_{PS}\ddot{q}_{PS} \tag{2.14}$$

Nevio Luigi Tagliamonte

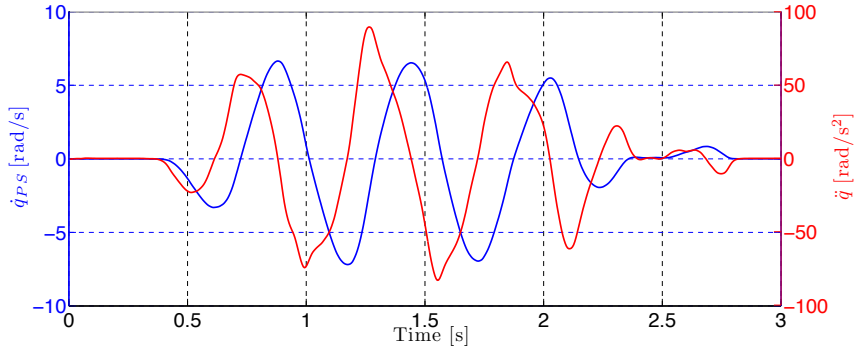

Figure 2.7: Velocity and acceleration profiles for one representative trial of the inertia and friction identification procedure. These values are obtained by manually back-driving the handle of the robot while locking AA and FE DOFs and compensating the gravity effect for the PS DOF.

The multivariable linear regression reported in (2.14) was calculated on 5 trials; the best fitting plane is shown in Fig. 2.8. We found $\tau_0^{PS} = 0.219 \pm 0.049$ N·m, $b_{PS} = 0.055 \pm 0.005$ Nm·s/rad and $B_{PS} = 0.012 \pm 0.001$ kg·m^2 with a mean R^2 of 0.942.

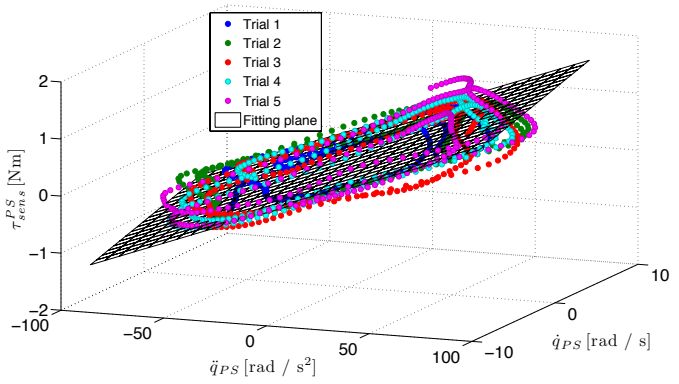

Figure 2.8: Multivariable linear regression for PS inertia and friction estimation as reported in (2.14). Considering the values averaged on 5 trials, we found $\tau_0^{PS} = 0.219 \pm 0.049$ N·m, the viscous friction $b_{PS} = 0.055 \pm 0.005$ N·m·s/rad and the inertia $B_{PS} = 0.012 \pm 0.001$ kg·m^2, with a mean R^2 of 0.942.

Nevio Luigi Tagliamonte

2.3 Effects of force control on robot transparency

In this section the effectiveness of the force control in (2.9) in improving the transparency of the robot is tested. First, the reduction of the robot mechanical impedance in the PS joint, due to the action of the force control has been estimated; then the reduction of forces/torques exerted by three subjects while performing two kinds of pointing tasks were analyzed, comparing the cases of *unpowered robot*, robot with *zero gains PD control*, and *force-controlled robot*.

2.3.1 Reduction of PS joint impedance

To evaluate the perceived robot mechanical impedance with the action of the force control, the same procedure described in section 2.2.2.2 was followed. In particular, the proportional gain of the force control was set to 250 $\mathrm{kg}^{-1}\cdot\mathrm{m}^{-2}$. The resultant perceived inertia should correspond to the inverse of this proportional gain (as explained in section 2.2) so we expect a value of 0.004 $\mathrm{kg}\cdot\mathrm{m}^2$.

In Fig. 2.9 velocity and acceleration profiles for one representative trial are shown.

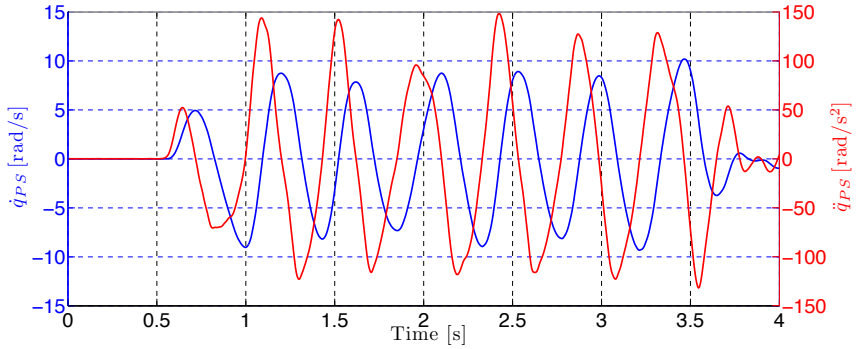

Figure 2.9: Velocity and acceleration profiles for one representative trial of the mechanical impedance evaluation test with force control active on the PS DOF. These values are obtained by manually back-driving the handle of the robot while locking AA and FE DOFs.

The multivariable linear regression reported in (2.14) was calculated on 5 trials; the best fitting plane is shown in Fig. 2.10. We found $\tau_0^{PS} = -0.059 \pm 0.043$ N·m, $b_{PS} = -0.002 \pm 0.002$ N·m·s/rad and $B_{PS} = 0.0037 \pm 0.0001$ $\mathrm{kg}\cdot\mathrm{m}^2$ with a mean R^2

Nevio Luigi Tagliamonte

of 0.980.

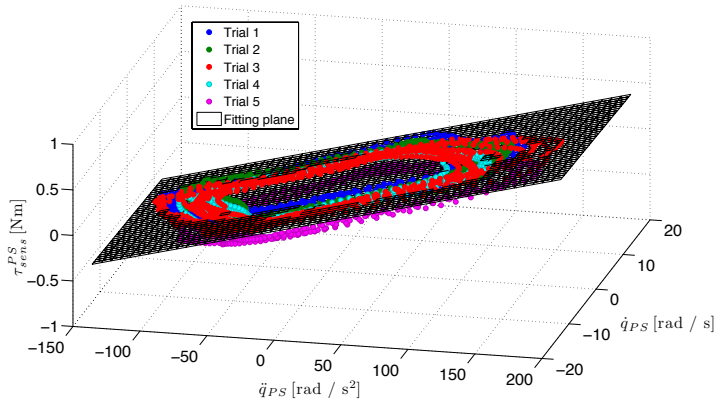

Figure 2.10: Multivariable linear regression for PS joint mechanical impedance estimation with force-controlled robot. Considering the values averaged on 5 trials, we found $\tau_0^{PS} = -0.059 \pm 0.043$ N·m, the viscous friction $b_{PS} = -0.002 \pm 0.002$ N·m·s/rad and the inertia $B_{PS} = 0.0037 \pm 0.0001$ kg·m^2, with a mean R^2 of 0.980. A reduction of about 70% of perceived inertia was obtained.

The negative value of friction suggests that an overestimation of this parameter was made. Anyway, this value can be considered negligible since it was found to be not statistically different from 0.

Of note, the implemented force control scheme in these conditions causes a reduction of the inertia of about 70% with respect to the case of PD control with gains set to zero (simple gravity compensation, as described in section 2.1). In particular, the estimated inertia $B_{PS} = 0.0037$ kg·m^2 is consistent with the expected value of 0.004 kg·m^2 demonstrating the effectiveness of the force control action.

2.3.2 Reduction of interaction forces/torques

In this section PS torques (τ^{PS}_{sens}, as in (2.13)) exerted by three healthy subjects (Sub1-3) to perform a 1-DOF (Pronation/Supination) task and a 3-DOFs task are reported for three different conditions: Unpowered Robot (UR), Zero gains PD control (ZPD) and Force-Controlled robot (FC).

2.3.2.1 Pronation/Supination (PS) task

During this 1-DOF task, three healthy subjects were asked to alternately reach two points displayed on a monitor on the left and right sides of a starting central point, only using the PS DOF (AA and FE DOFs were constrained in their rest positions through PD position control).

Fig. 2.11 shows the PS torque (2.13) exerted by one representative subject in the different testing conditions. The only gravity compensation (PD control with gains set to zero, ZPD) reduces the torques required to perform the task with respect to the case motors are turned off; a further decrease of the torque in the case of the force-controlled robot can be noticed. Fig. 2.12 reports the peak and mean values of the PS torque for the 1-DOF trials on the three subjects.

It can be seen that these values slightly decrease increasing the gain K_P although no major changes occur. In case of $K_P = 300$ kg^{-1}·m^{-2} the peak torque decreases of the 90% while the mean torque of the 81% with respect to the unpowered robot case. PD control only causes a reduction of the 54% and 46% of the peak and mean torques respectively. Of note, the force control ($K_P = 300$ kg^{-1}·m^{-2}) reduces the peak and mean torques of 77% and 65% respectively, with respect to the PD control condition.

2.3.2.2 3-DOFs task

During this 3-DOFs task, three healthy subjects were asked to perform pointing movements with the wrist from the center of the workspace to eight peripheral points arranged in a circle displayed on the monitor; this is also a typical 'video game' rehabilitation exercise (often referred as *clock* game), which has been used in [17, 3] to test the effect of the robot on human motor strategies.

Fig. 2.13 shows the PS torque (2.13) exerted by one representative subject in the different testing conditions. Also in this case gravity compensation PD control with gains set to zero lowers the PS torques with respect to the case of unpowered robot and force control improves this effect.

Fig. 2.14 reports the peak and mean values of the PS torque for the trials on the three subjects. No major changes occur with the gain increasing. In case of

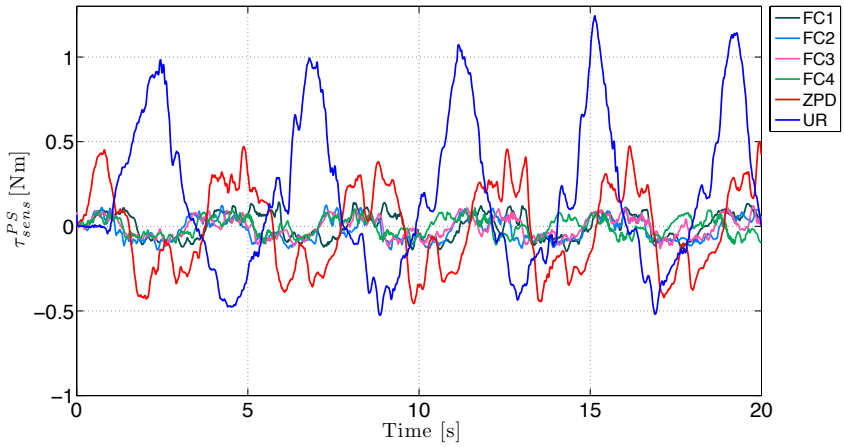

Figure 2.11: τ_{sens}^{PS} pattern for 1-DOF PS tasks, performed by one representative subject, in five different conditions: Unpowered Robot (UR); Zero gains PD control (ZPD); Force-Controlled robot $K_P = 150$ kg^{-1}·m^{-2} (FC1); Force Control $K_P = 200$ kg^{-1}·m^{-2} (FC2); Force Control $K_P = 250$ kg^{-1}·m^{-2} (FC3); Force Control $K_P = 300$ kg^{-1}·m^{-2} (FC4).

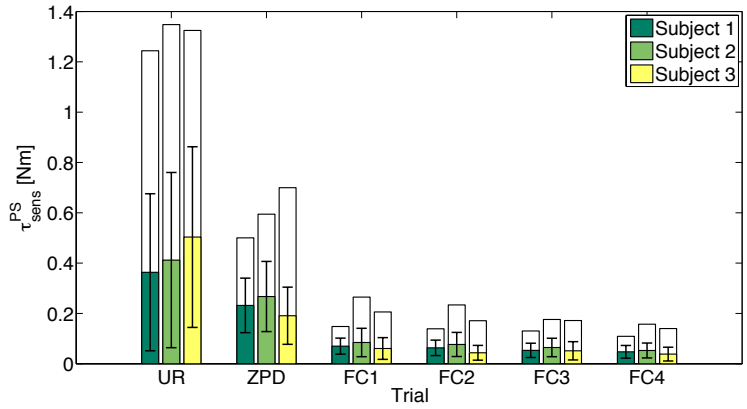

Figure 2.12: τ_{sens}^{PS} mean (colored) and peak (blank) values for 1-DOF PS tasks on three subjects; error bars represent the standard deviation. Five conditions are reported: Unpowered Robot (UR); Zero gains PD control (ZPD); Force-Controlled robot $K_P = 150$ kg^{-1}·m^{-2} (FC1); Force Control $K_P = 200$ kg^{-1}·m^{-2} (FC2); Force Control $K_P = 250$ kg^{-1}·m^{-2} (FC3); Force Control $K_P = 300$ kg^{-1}·m^{-2} (FC4).

Nevio Luigi Tagliamonte

$K_P = 300$ kg^{-1}·m^{-2} the peak torque decreases of the 80% and the mean torque decreases of the 78% with respect to the unpowered robot case. PD control only decreases of the 5.6% and 5.4% the peak and mean torques respectively; thus the force control ($K_P = 300$ kg^{-1}·m^{-2}) reduces the peak and mean torques of 79% and 77% respectively, with respect to the PD control condition.

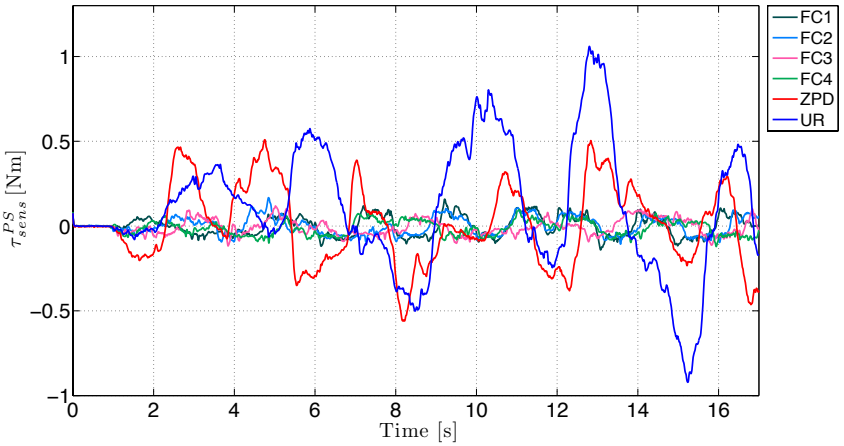

Figure 2.13: τ_{sens}^{PS} pattern for 3-DOFs tasks, performed by one representative subject, in five different conditions: Unpowered Robot (UR); Zero gains PD control (ZPD); Force-Controlled robot $K_P = 150$ kg^{-1}·m^{-2} (FC1); Force Control $K_P = 200$ kg^{-1}·m^{-2} (FC2); Force Control $K_P = 250$ kg^{-1}·m^{-2} (FC3); Force Control $K_P = 300$ kg^{-1}·m^{-2} (FC4).

An overall view of the results obtained on three subjects is presented in Table 2.2.

Table 2.2: τ_{sens}^{PS} peak and mean values for PS and 3-DOFs tasks.

	Peak torque [N·m]		*Mean torque* [N·m]	
	PS	3-DOFs	PS	3-DOFs
UR	1.306 ± 0.055	0.553 ± 0.441	0.427 ± 0.071	0.167 ± 0.131
ZPD	0.598 ± 0.099	0.522 ± 0.198	0.230 ± 0.038	0.158 ± 0.062
FC1	0.206 ± 0.059	0.155 ± 0.009	0.072 ± 0.012	0.056 ± 0.004
FC2	0.181 ± 0.048	0.151 ± 0.185	0.061 ± 0.017	0.049 ± 0.004
FC3	0.162 ± 0.028	0.139 ± 0.021	0.057 ± 0.007	0.043 ± 0.004
FC4	0.135 ± 0.024	0.108 ± 0.014	0.081 ± 0.066	0.037 ± 0.002

To verify that the decreasing of the interaction torques was really due to a re-

Nevio Luigi Tagliamonte

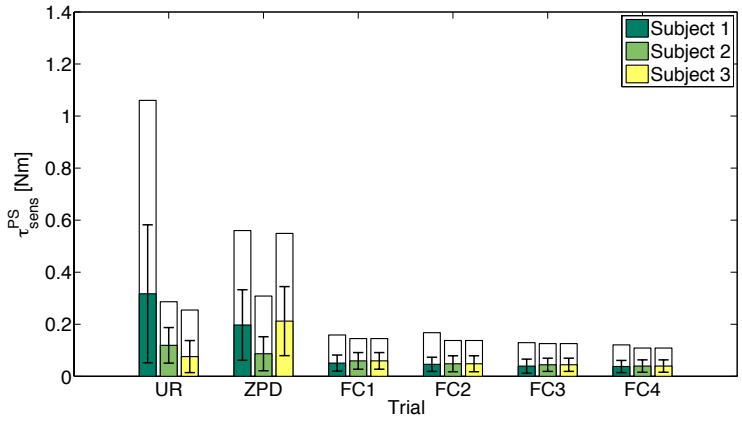

Figure 2.14: τ^{PS}_{sens} mean (colored) and peak (blank) values for 3-DOFs PS tasks on three subjects; error bars represent the standard deviation. Five conditions are reported: Unpowered Robot (UR); Zero gains PD control (ZPD); Force-Controlled robot $K_P = 150$ kg^{-1}·m^{-2} (FC1); Force Control $K_P = 200\cdot$ kg^{-1}m^{-2} (FC2); Force Control $K_P = 250$ kg^{-1}·m^{-2} (FC3); Force Control $K_P = 300$ kg^{-1}·m^{-2} (FC4).

duction of the robot impedance and not to possible differences in the execution of the tasks during the five testing conditions, the RMS values of the velocity for the three subjects were analyzed. Results reported in Tables 2.3–2.5 show that the tasks executed by each subjects in different conditions are comparable and that the ones executed with lower velocities are actually those where the robot is in UR or ZPD conditions. These observations confirm that the reduction of the interaction torques in FC condition were due to a real reduction of robot impedance.

Table 2.3: RMS values of the velocity patterns during PS and 3-DOFs tasks [rad/s] for subject 1.

	PS	3-DOFs		
	$\dot{q}_{PS,rms}$	$\dot{q}_{FE,rms}$	$\dot{q}_{AA,rms}$	$\dot{q}_{PS,rms}$
UR	0.7062	0.3731	0.2052	0.3879
ZPD	0.8031	0.3573	0.2014	0.4664
FC1	0.7946	0.4255	0.2063	0.3356
FC2	0.7987	0.4181	0.2064	0.3085
FC3	0.8235	0.4243	0.2155	0.3761
FC4	0.8645	0.4002	0.2100	0.3455

Table 2.4: RMS values of the velocity patterns during PS and 3-DOFs tasks [rad/s] for subject 2.

	PS	3-DOFs		
	$\dot{q}_{PS,rms}$	$\dot{q}_{FE,rms}$	$\dot{q}_{AA,rms}$	$\dot{q}_{PS,rms}$
UR	0.7497	0.3677	0.2225	0.0431
ZPD	0.8212	0.4370	0.2545	0.0613
FC1	1.0125	0.5225	0.2790	0.1673
FC2	0.9155	0.5912	0.2870	0.3176
FC3	0.8797	0.5830	0.2938	0.2281
FC4	0.8587	0.5701	0.3055	0.3008

Table 2.5: RMS values of the velocity patterns during PS and 3-DOFs tasks [rad/s] for subject 3.

	PS	3-DOFs task		
	$\dot{q}_{PS,rms}$	$\dot{q}_{FE,rms}$	$\dot{q}_{AA,rms}$	$\dot{q}_{PS,rms}$
UR	0.9616	0.5360	0.3263	0.0287
ZPD	0.9485	0.1258	0.0572	0.8529
FC1	1.0902	0.5225	0.2790	0.1673
FC2	0.9389	0.5912	0.2870	0.3176
FC3	0.9429	0.5830	0.2938	0.2281
FC4	1.0217	0.5701	0.3055	0.3008

2.3.3 Considerations on force control performances

The performance of the adopted force control scheme in general depends on the dynamic characteristics of the robot and of the interacting system and some unstable behaviors may occur when control gains are high. This is particularly true in the case of industrial robots, where the intrinsic mechanical impedance is extremely high. Well known studies on direct force control of manipulators explored sources and solutions to instability caused by interactions with the environment (*coupled instability*) associated with force feedback [28, 29, 30]. In [29] it was demonstrated that the major source of instability is the *non-colocation* of sensors and actuators. In [28] it was shown that a robot which is stable when no interaction occurs (*isolated*

stability) can exhibit unstable behaviors when external forces from the environment are applied. Necessary and sufficient conditions for coupled stability were derived, showing limitations of direct proportional force control. In particular, a simplified analysis on linear, time-invariant systems showed that a feedback controlled plant is stable during interaction if it has the interaction port behavior of a *passive system*: the transfer function of the system impedance at the interaction port, defined as the ratio between output force and input velocity, must be a positive real function. This mathematical condition basically quantifies the notion that the system can not, for any time period, deliver more energy at its interaction port than has in total been introduced into the same port. This condition is valid for interactions with arbitrary stable, passive environments (linear or not). A corollary of this criterion is that coupled stability is guaranteed if stability is demonstrated for interactions with *all* linear masses and *all* linear springs (pure springs and pure masses are commonly termed *worst environments*).

Here we briefly summarize some results reported in [28] underlying theoretical limitations of the adopted force control and showing that practical implementation and specific interaction conditions can exhibit different behaviors, as already shown in [29]. To this aim a basic 1-DOF translational version of the control law (2.2) will be reported considering, for simplicity sake, a perfect compensation of viscous friction and of gravitational effects. In Fig. 2.15 a simple robot model with a single structural resonant mode is presented which captures the essential features of robot dynamics with non-colocated actuation and sensing elements.

k and c generally represent structural dynamics or other effects such as actuator or transmission dynamics. The overall mass of the system B is distributed in two equal halves, one is driven by the actuator force F and the other one is subject to the interaction force with the environment F_{int}. Adapting equation (2.2) to this case and considering a desired interaction force $F_d = 0$ leads to a command force

$$F = F_{int} - \hat{B} K_p F_{int} \tag{2.15}$$

where $\hat{B}$ is the estimated mass and K_P is the control gain. Assuming the constant quantity $(\hat{B}K_p - 1) = K_f$, equation (2.16) can be rewritten as:

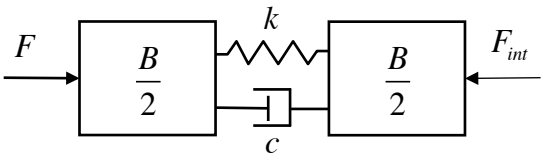

Figure 2.15: 1-DOF robot model with non-colocated actuation and sensing, adapted from [28]. k and c generally represent single-resonance robot dynamics. The overall mass of the system B is distributed in two equal halves, one driven by the actuator force F and the other one subject to the interaction force F_{int}. Friction and gravitational effects are considered to be perfectly compensated.

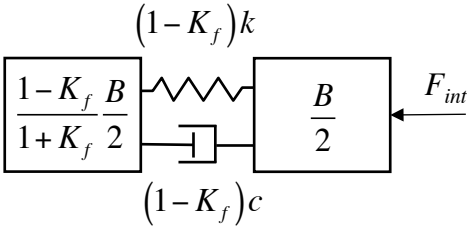

Figure 2.16: Passive physical equivalent representation of the single-resonance robot of Fig. 2.15 under proportional force feedback control with gain K_f, adapted from [28].

$$F = -K_f F_{int} \tag{2.16}$$

Given this feedback term, a *passive physical equivalent* representation for the system of Fig. 2.15 can be derived according to [28] as reported in Fig. 2.16.

The force feedback gain K_f is restricted to be between -1 and 1 for this to be a passive realization. For $K_f > 1$ spring, mass and damper would assume negative values and the system would become non-passive, thus violating coupled stability criterion. It is worth noticing that these negative values do not affect isolated stability: force feedback is not a state feedback, hence the poles of the closed loop system are equal to the ones of the open loop system which is intrinsically stable. From (2.16) it can be seen that actuator force is null if no interaction force is measured. Moreover, since K_f limit is independent of the values of the structural stiffness and damping, any system under proportional force feedback becomes non-passive for a

gain greater than unity and it is vulnerable to coupled instability.

If $K_f = 1$ robot internal dynamics are masked and the minimum impedance is achieved. Anyhow, an amount of inertia equal to $B/2$ cannot be compensated thus demonstrating that the this simple controller is not able to reduce the apparent inertia to less than 50% of its physical value if passivity has to be guaranteed.

Anyhow, in our case no critical stability problems occurred when force control was implemented and tested on the InMotion^3 system, even though we used a gain $K_P = 300$ kg^{-1}·m^{-2}, corresponding to a 70% reduction of the perceived inertia (about 0.003 kg·m^2) and to $K_f = 2.6$ which should theoretically give rise to coupled instability.

The explanation of this apparent discrepancy with theoretical prediction has to be found in the fact that the traditionally used passivity criterion ensures stability only with passive environments, and provide no information if the interacting system is non-passive. Remarkably, even though the human neuro-motor system employes sensory feedback loops including time delays, which make it basically non-passive, the successful interaction with passive robots is due to limited energy production and frequency range of active human motion [31].

Passive environments and, in particular, the worst environments presented above (e.g. high pure stiffness), include systems with dynamics that can be very different from human limbs, which have finite mass and limited stiffness. Hence, since the magnitude of human limbs impedance is bounded significantly, the use of passivity as stability measure may be exceedingly conservative for human-interactive robots, and performance may be uselessly sacrificed in achieving this objective.

In summary, destabilizing systems for a particular robot and controller can be limited to dynamics far apart from robot practical interaction conditions, and even though the controller makes the robot non-passive, coupled stability is still possible. Passive control independence from the environment is a great advantage but also a limitation: this approach can be insufficiently conservative if the interacting system is non-passive, or excessively conservative if it has limited dynamical properties [32]. An alternative analysis of coupled stability can consider interaction only with particular systems, i.e. the machines are said to be *complementary* to the specific sets

of systems with which they are designed to interact[3] [32]. This choice consider even limited knowledge of the environment to design controllers thus taking advantage of the properties of both interacting systems, rather than just one.

Nevertheless, force feedback is used in many robots in real applications, where passivity is seldom achieved: control gains are sometimes tuned manually to an appropriate stability margin, based on testing and the result is not necessarily passive. Empirical demonstration that relaxing passivity can allow improved performance still in stable conditions can be found, for example, in [32]. In this work, whose results are in line with achievements of this thesis, force feedback controller was implemented on a screw-driven vertical robot module to reduce its perceived impedance. Extensive testing with human arms, and also clinical trials [33], revealed the coupled system to be stable, even for gain $K_f = 5$. The controller successfully reduced apparent Coulomb friction and inertia by a factor of six even though the closed loop plant was non-passive. This system exploits a characteristic of the environment (in this case, its limited stiffness) to expand the space of stable interaction controllers. As in many literature example, the most problematic environments are simply avoided, and coupled stability is determined empirically allowing a more 'aggressive' force feedback.

During the tests with the InMotion[3] we did not experienced any unstable behaviors, not even when the handle was manually excited to oscillate with a peak velocity of the order of 10 rad/s and a peak acceleration of the order of 150 rad/s^2, values which are grater than the ones normally measured during pointing tasks. Nonetheless, trials for the evaluation of human motor strategies (which will be described in the next section) were performed using a gain value lower than the maximum tested one. In both 1-DOF and 3-DOFs tasks, we found a net decrease of torques exerted by the subjects in case of force-controlled robot with respect to the PD control condition while no significant differences occurred when different gain values were used for force control. Since improving the gain values, with a fixed friction compensation, corresponds to reduce only the perceived inertia (0.007 kg·m^2 and 0.003 kg·m^2 for $K_P = 150$ kg^{-1}·m^{-2} and $K_P = 300$ kg^{-1}·m^{-2} respectively) it could be concluded

[3] A passive robot is complementary to the set of passive environments.

that the major contribution in the achievement of robot transparency is given by the friction reduction, which is of course due to the direct friction compensation but also to the force feedback.

Moreover, considering a perfect estimation of gravity and friction terms, from (2.1) and (2.2) it can be seen that the force error dynamics becomes:

$$\boldsymbol{e}_f = \frac{\boldsymbol{B}}{\hat{\boldsymbol{B}}\boldsymbol{K_P}}\ddot{\boldsymbol{q}} \tag{2.17}$$

Equation (2.17) shows that an error in the inertia estimation is compensated by the $\boldsymbol{K_P}$ gain. If inertia is overestimated the force control gain has to be reduced of the same amount to preserve the stability margin, while if inertia is underestimated the gain can be incremented. From a different perspective we can say that the responsible of the stability is the product $\hat{\boldsymbol{B}}\boldsymbol{K_P}$ (see also equation (2.16)) so that a variation of the gain make the control law basically insensible to inertia estimation.

2.4 Human motor strategies during pointing tasks

In this section we analyze pointing tasks of three subjects in three different operative conditions. Firstly wrist rotations were recorded using a handheld device that introduced a negligible loading effect (in this condition subjects movements were basically free); these results were compared with the ones obtained during the interaction with the robot when the gains of its standard PD control scheme were set to zero and when the proposed force control was active. Since the zero gains PD control actually corresponds to only gravity compensation, the comparison with the force-controlled robot allows to evaluate the effect of inertia and friction compensation and of force feedback.

For each condition the experimental protocol included five learning trials, that were used to make the subjects acquainted with the experimental setup, and five trials to be used for data analysis.

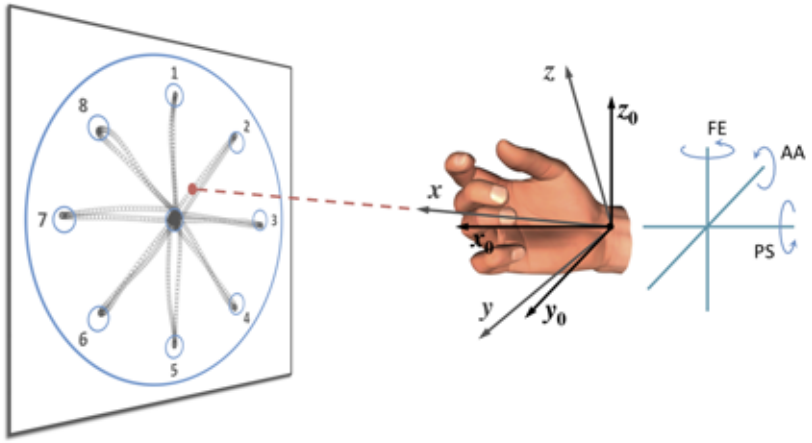

Figure 2.17: Typical 'video game' used to guide subject to perform pointing tasks and representation of the three wrist DOFs with the reference frames.

2.4.1 Analysis of wrist movements during pointing tasks

2.4.1.1 Handheld device

To assess natural motor strategies during pointing task with the wrist, we used a 'video game' showing to subjects some visual targets to be reached (from/to a central target to/from peripheral ones) (Fig. 2.17); this protocol has been already used in the 3-DOFs experiments presented in the previous sections and in [3] to assess the existence of Donders' law for the wrist during pointing tasks.

The subject under test was seated on a chair and rested his arm on a support purposively created to bind arm and forearm (Fig. 2.18). In this way she/he could execute pointing tasks moving only the wrist.

Each trial started after defining a *primary position* (see [3] for details); the subject was then instructed to move the round cursor on the screen towards the peripheral positions randomly chosen by the software among 1, 2, . . . , 8 (Fig. 2.17) and then back to the central position. To register the wrist movements we instrumented an hollow cylindrical handle (height: 150 mm; outer diameter: 50 mm; inner diameter: 35 mm; mass: 120 g) with an inertial magnetic unit (IMU, MTx-28A53G25 device from XSens Inc. - angular resolution: 0.05 deg; static orientation accuracy: < 1 deg; dynamic accuracy: 2 deg RMS; bandwidth: 40 Hz); this setup is indicated

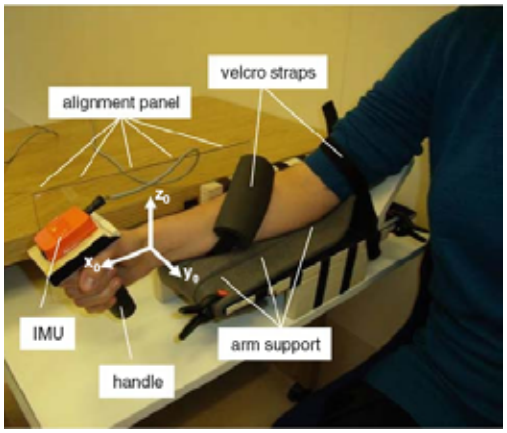

Figure 2.18: Experimental apparatus for trials with handheld device.

as *handheld device* (Fig. 2.18).

With the wrist in its primary position, a fixed reference frame $\{x_0, y_0, z_0\}$ was defined (see Fig. 2.18): z_0-axis is along the vertical direction (upwards), x_0-axis is horizontal and aligned with the forearm (forward) and y_0-axis is horizontal and perpendicular to the forearm (leftward). A second (moving) reference frame $\{x, y, z\}$ attached to the wrist (see also Fig. 2.17) was defined to coincide with the fixed reference frame when the wrist is in the primary position.

The IMU, connected to a PC, was configured to continuously acquire a rotation matrix $\boldsymbol{R}$ (at a rate of 100 samples/s) which expresses the orientation of the wrist moving frame with respect to the fixed frame.

We calculated the rotation vector as:

$$\boldsymbol{r} = \frac{\theta}{2\sin(\theta)} \begin{bmatrix} R_{3,2} - R_{2,3} \\ R_{1,3} - R_{3,1} \\ R_{2,1} - R_{1,2} \end{bmatrix} \tag{2.18}$$

where $R_{j,k}$ indicates the (j,k) element of the matrix $\boldsymbol{R}$ and $\theta = \arccos[(\mathrm{trace}(\boldsymbol{R}) - 1)/2]$, being $\mathrm{trace}(\boldsymbol{R}) = R_{1,1} + R_{2,2} + R_{3,3}$ and $|\theta| < \pi$. The vector $\boldsymbol{r}$ defines the axis (parallel to $\boldsymbol{r}$ itself) and the amount of rotation ($\|\boldsymbol{r}\| = \theta$).

Since the primary position was selected as the 'home' position for the IMU the coordinates of the x, y, and z axes with respect to the fixed frame could be deter-

mined, respectively, as the first, the second, and the third columns of the matrix $\boldsymbol{R}$. For this reason the pointing vector $\boldsymbol{n}$ (which represents the pointing direction during the tasks) was always parallel to the moving x-axis after the reset procedure and it could be determined as follows:

$$\boldsymbol{n} = \boldsymbol{R}\ [1\ 0\ 0]^T \tag{2.19}$$

Considering the subscript i to represent the i-th acquisition sample, the temporal sequence of acquired rotation matrices and of the derived rotation and pointing vectors can be indicated as $\boldsymbol{R}_i$, $\boldsymbol{r}_i$ and $\boldsymbol{n}_i$ respectively.

Numerically, the sequence $\boldsymbol{r}_i = [r_{xi}\ r_{yi}\ r_{zi}]^T$ was fitted to $\boldsymbol{r}_i^* = [r_{xi}^*\ r_{yi}\ r_{zi}]^T$ where r_{xi}^* is defined by a generic quadratic surface:

$$r_{xi}^* = C_1 + C_2 r_{yi} + C_3 r_{zi} + C_4 r_{yi}^2 + 2C_5 r_{yi} r_{zi} + C_6 r_{zi}^2 \tag{2.20}$$

where the coefficients $C_1, \ldots, C_6$ were determined via least-squares fitting methods. The first three coefficients (C_1, C_2 and C_3) define a plane, while the last three coefficients (C_4, C_5 and C_6) are related to the curvature of the fitted surface. In particular, the coefficient C_5 denotes the amount of twisting of a quadratic surface.

Fig. 2.19 reports an example for the graphical representation of the temporal sequences of rotation and pointing vectors ($\boldsymbol{r}_i$ and $\boldsymbol{n}_i$). While the wrist pointing directions necessarily lie in a 2-dimensional space, the three components r_{xi}, r_{yi} and r_{zi} of a rotation vector $\boldsymbol{r}_i$, in general, define points of a 3-dimensional space. Remarkably, it can be observed that the rotation vectors tend to lie on a 2-dimensional (Donders') surface, represented by equation (2.20), which can also be well approximated by a plane near the primary position.

As in previous studies [17, 3], the thickness of a Donders' surface is defined as the standard deviation of the fitting error between the sequence $\boldsymbol{r}_i$ and the best fitting surface. For a given set of fitting coefficients ($C_1, \ldots, C_6$), the fitting error is defined as $r_{xi} - r_{xi}^*$.

Obviously, thickness values quantify the goodness of fitting and indicate how much the rotation vectors tend to lie on the best fitting surface (Donders' surface);

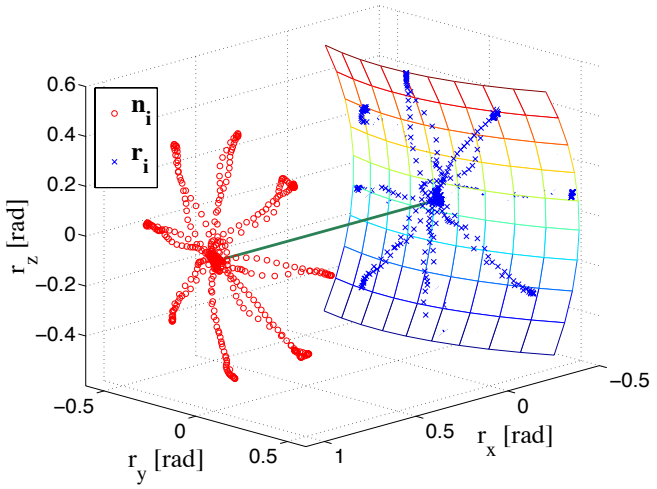

Figure 2.19: Rotation vectors (crosses) represented in the 3-dimensional space of the motor task together with the pointing vectors (circles). A 2-dimensional quadratic surface fits the rotation vectors. The green straight line represents the pointing direction when the wrist is in the primary position.

low values of thickness indicate that a soft constraint (such as Donders' law) apply to wrist kinematics during pointing tasks.

2.4.2 Wrist robot

Subjects were strapped to a chair with their right arm fasten to the InMotion[3] arm-support by appropriate belts to minimize torso, shoulder and elbow movements; in this configuration only wrist rotations were left unconstrained while the subject grasps the handle of the robot (Fig. 2.20). The more distal strap only constraints the flexion of the elbow while allowing a free pronation/supination movement. In this way the PS joint is moved by the user only exerting forces on the handle and not via the strap.

For the experiments described in this section, two different conditions were tested: in the first one, the motors of the robot were commanded so that they only compensate gravity, with the stiffness and damping parameters of the native impedance controller set to zero; in the second one, subjects performed the same task with the robot controlled using the force control law in (2.2). In what follows we refer to these two operative conditions as *zero gains PD control* and *force-controlled robot*

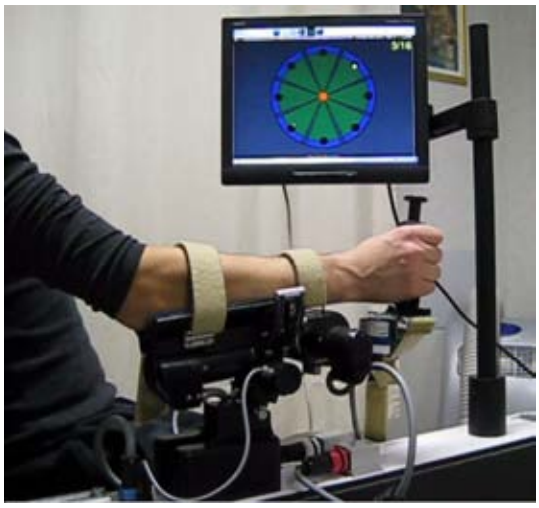

Figure 2.20: Experimental setup for trials with InMotion^3 system.

respectively.

The starting position for the wrist was set as to coincide with the mechanical zero position of the robot, defined in [20]. Knowledge of the sequence, from proximal to distal, of the mechanical joints allows to determine the wrist orientation $\boldsymbol{R}_w$ from the angles as sensed by the encoders of the system:

$$\boldsymbol{R}_w = \boldsymbol{R}_x(\theta_{PS})\,\boldsymbol{R}_y(\theta_{AA})\,\boldsymbol{R}_z(\theta_{FE}) \tag{2.21}$$

where x, y and z coincide with the axes of the fixed reference frame. i.e. the primary or 'zero' position for the wrist. For a given wrist orientation $\boldsymbol{R}_w$, the wrist pointing direction $\boldsymbol{n}_i$ is given as in (2.19). During the execution of each task, data were acquired at a rate of 200 Samples/sec, in particular the three sequences of sampled angles, and (where i refers to i-th sample at time t_i). Using equation (2.21), the sequence of wrist orientation $\boldsymbol{R}_{wi}$ at time t_i was derived. The sequence of wrist pointing directions $\boldsymbol{n}_i$ was evaluated via (2.19) and finally the sequence of rotation vectors $\boldsymbol{r}_i$ was obtained via (2.18). The sequence $\boldsymbol{r}_i = [r_{xi}\ r_{yi}\ r_{zi}]^T$ was numerically fitted to a generic quadratic surface with coefficients $C_1, \ldots, C_6$ as in (2.20).

Nevio Luigi Tagliamonte

2.4.3 Free movements and human-robot interaction: a comparison

Donders' surfaces are typically subject-dependent and reveal personal motor strategies, as demonstrated in previous studies [3]. The effect of a purely mechanical (holonomic) constraint on a 3-DOFs wrist mechanism, e.g. a locked joint, is to constrain the system configuration exactly to a 2-dimensional surface. Noisy measurements and mechanism non-idealities (e.g. backlash) would reveal such a surface with a certain resolution, for the robotic systems under consideration this is (often much) less than 0.1 deg. Observing a mechanically unconstrained 3-DOFs system evolving on a subspace (2-dimensional surface) of its configuration space (3-dimensional) is indicative of active control. This has been attributed to a form of neural control in studies relative to the oculomotor system [1] and to the upper limbs [2, 19, 3]. Unlike physical constraints, neural control is characterized by much larger variability (or *biological noise* [1]) leading to thicknesses in the order of 1–3 deg [1, 2].

In this section we reported the results obtained in the three different experimental conditions, namely experiments with the handheld device, with the robot in zero gains PD control mode and with the force-controlled robot. In Figures 2.21–2.22 the Donders' surfaces and the histograms of the mean values of $C_1, \ldots, C_6$ coefficients are reported.

In the experiments when the handheld device was used, neural kinematic constraints arose as 2-dimensional surfaces embedded in the 3-dimensional space of wrist configurations. The lightness of the handheld device allows the subjects' own motor style to emerge: different trials show similar curvature for the same subject, while they differ among subjects, as already proved in [17, 3]. During the interaction of subjects with the robot in zero gains PD control mode the high goodness-of-fit in terms of thickness (1-2 order of magnitude smaller than in the experiments with the handheld device) revealed the strong influence of robot in masking the human motor strategies. In this case 2-dimensional surfaces are similar for all subjects highlighting the absence of any biological noise (Fig. 2.21). It has to be noticed that, since the robot constraining behavior has also been verified in [17] (where experiments were conducted without any modification to the mechanical structure of the system), the perturbation to the human natural motor strategies cannot be due to the removal

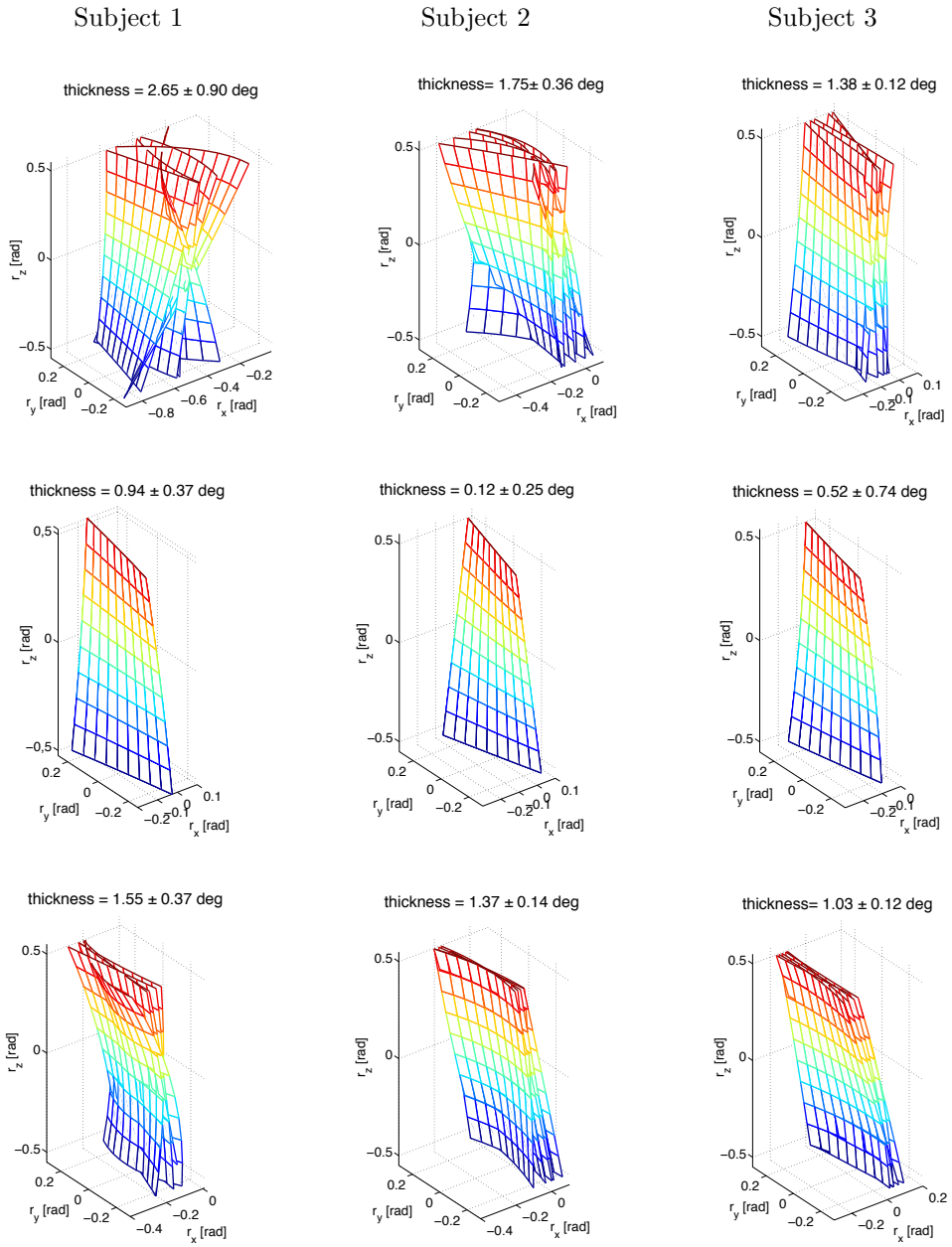

Figure 2.21: Donders' surfaces fitting the rotation vectors (in radians) relative to three different subjects who perform the same pointing task, each one composed of 5 trials, in three different operative way: with handheld device (top), with robot in zero gains PD control mode (middle), with force-controlled robot (bottom).

Nevio Luigi Tagliamonte

of the passive revolute joint and of the linear slider.

In the case of force-controlled robot, 2-dimensional surfaces were different among tested subjects; moreover, each subject' surfaces were similar to those coming from the experiment with the handheld device, with thickness values got back into the physiological range (1–3 deg). From the analysis of the coefficients C_4, C_5 and C_6, which are related to Donders' surfaces curvature, no discrepancy between the values measured with the handheld device and with the force controlled robot emerges. This confirms the analogies between the two performances.

The constraining action of the robot, when controlled through the PD control (with gains set to zero) is particularly evident in the Helmholtz-like behavior of the surfaces: the sign of the C_5 coefficient is inter-subjectively invariant and positive. It is worth recalling that the Helmholtz gimbal is a 2-dimensional mechanism and its rotation vectors necessarily lie on a 2-dimensional surface; in the case the surface is expressed through the (2.20) this implies $C_5 = 1/2$ and all the other coefficients to be zero. The explanation to this result is that subjects natural movements are affected by an excessive mechanical impedance on the PS joint of the robot; this is confirmed by the restoration of a natural behavior during the execution of the tasks with a more transparent robot (from Table 2.6 it can be seen that thickness values became physiological) and by an evident activation of PS DOF.

It is worth highlighting that, due to stability limitations presented above, we could easily achieve an acceptable transparent behavior to make re-emerge human natural motor features because the InMotion^3 system already presented a good level of back-drivability. Hence, the same approach would not have given successful results if the mechanical properties of the robot had been far apart from the desired one.

2.5 Conclusions

The presented work addresses not only the traditional issues of pHRI in terms of safety and biomechanical compatibility but also the problem of coping with human motor strategies and neural mechanisms adopted to solve redundancy during motor tasks which are not appropriately considered in the design of current robotic systems.

The analysis of neural constraints for the human wrist during kinematically re-

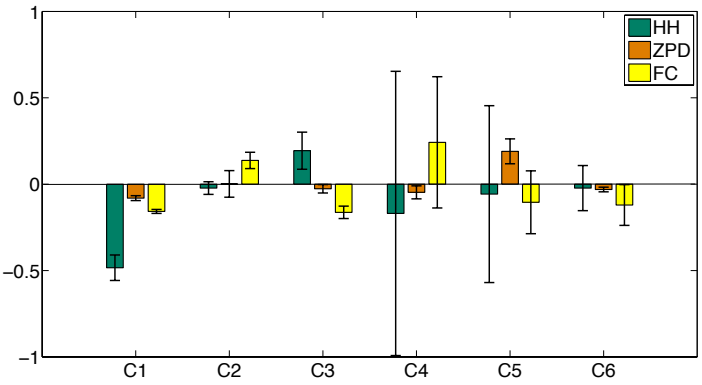

(a)

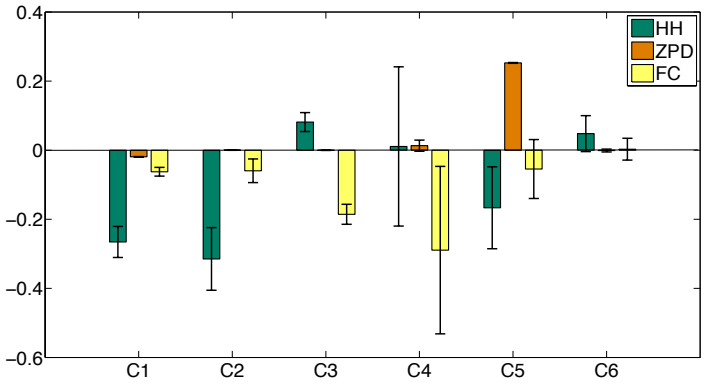

(b)

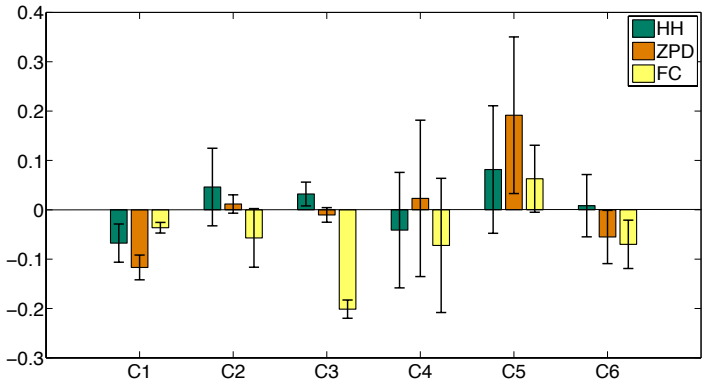

(c)

Figure 2.22: Histograms of the C_1, ..., C_6 coefficients (averaged on 5 trials, the vertical bars represent the 95% confidence interval) each of one relative to a single subject in 3 different operative conditions; (a) Subject 1, (b) Subject 2, (c) Subject 3. (HH: HandHeld device; ZPD: robot in Zero gains PD control mode; FC: Force-Controlled robot). C_1 is in rad, C_2–C_3 are dimensionless, C_4–C_6 are in rad^{-1}.

Nevio Luigi Tagliamonte

Table 2.6: Thickness values for Donders' surfaces [rad]. ZPD: robot in Zero gains PD control mode; FC: Force-Controlled robot).

Subject	HH	ZPD	FC
1	0.031 ± 0.006	0.016 ± 0.007	0.024 ± 0.002
2	0.046 ± 0.016	0.002 ± 0.004	0.027 ± 0.006
3	0.024 ± 0.002	0.009 ± 0.013	0.018 ± 0.002
overall	0.034 ± 0.008	0.009 ± 0.008	0.023 ± 0.003

dundant tasks showed that motor strategies can be perturbed when subjects interact with a state-of-the-art wrist robot, despite its high level of back-drivability [17, 3]. This is due to excessive mechanical impedance associated with the PS joint.

This confirms results found in studies on human motor control and robot-aided neurorehabilitation which assessed the influence of robot dynamics on subjects psychophysic performances.

In this work a basic control scheme, specifically for the PS axis, was implemented to reduce human-robot interaction forces and to study the effects of a lower perceived impedance on such neural constraints. From the analysis of Donders' surfaces associated to the execution of pointing tasks it was found that, when interacting with the force-controlled robot, subjects regained natural motor behaviors as during free motion (measured with a lightweight handheld device).

The work emphasizes the possibility of minimizing the perturbation to human natural motion even through simple solutions like a well known direct force control approach. Nevertheless, it was possible to successfully exploit this solution since intrinsic mechanical properties of the robot were already close to the acceptable ones. Conversely, the employed direct force control scheme would have been capable of reducing impedance only to a certain extent, with performances bounded by coupled stability requirements.

Since transparency can be primarily guaranteed only by the *hardware design* more than by the control design (as also suggested in pioneer studies on force control, [28]), it is crucial to examine the effects of different levels of back-drivability on human natural movements and to point out which is the range of impedance values that can

avoid the occurrence of constraining behaviors thus providing guidelines for future designs. For this reason, this work is the starting point for analyses able to suggest new approaches in the design of rehabilitation robots which, at the state of art, do not consider neural constraints but only biomechanical ones.

Part II

Compliant actuators and joints for pHRI: analysis and new designs

Chapter 3

Double actuation architectures

As pointed out in chapter 1, in recent years robotic systems have been more and more conceived for a number of applications where a high level of adaptability is required, in order to interact with the environment and to stably comply with actions exerted by external agents. New design paradigms and actuation solutions have grown, so to opportunely fulfill the requirements of these scenarios [34] and traditional *stiff robots* [35], with rigid, high-precision behavior, have given way to *soft robots* [36, 37] which operate compliantly.

In *rehabilitation and assistive robotics*, the pHRI is a normal operative condition since users are continuously connected to a machine which guides or assists their movements. In this case a high level of biomechanical compatibility and dynamical adaptability is desirable. These machines have to be as transparent as possible to the active motion of the users and to provide assistance as needed in conditions where they are not able to complete a prescribed motor task [38].

Robotic prostheses are required to restore human functionalities lost due to amputation in a large variety of dynamical conditions. In the case of human locomotion, for example, collision with terrain is managed cyclically and exploited to store energy in elastic tissues, which can be released to reduce the active work produced by the muscles [39]. For this reason, in active prostheses, the necessity of having mechanical properties dynamically varying as a function of gait phase or speed and adapting to terrain shape is crucial to mimic the humans' physiological features [40].

Reproducing passive elastic properties of human and animal joints can also enormously improve the energetic efficiency of *legged robots*, especially in the case of running and hopping machines, as demonstrated in pioneer works in the early 1980s both in simulation and in prototypal implementations [41]. The on-line modification of dynamical properties is also pivotal in bipedal robots using the principles of pseudo-passive locomotion [4] in which a stable limit cycle of the system has to be achieved and possibly modified.

In *neuroscience*, the theories on human sensory-motor control and on learning strategies can be experimentally validated through dedicated robotic platforms [42, 43]. These systems have to reproduce the kinematic, dynamic and functional features of human limbs also with an high level of flexibility to test different kind of control schemes. One of the main attributes to be replicated is the muscular agonistic/antagonistic actuation arrangement to have the capability of separately regulate joints position and stiffness. In this way it is possible, for example, to investigate the debated Equilibrium Point (EP) control hypothesis [44].

In *industrial robotics* it is crucial to limit the energy exchange with external agents during unwanted collisions and to modulate the level of intervention during human-robot cooperative tasks [34, 45, 46]. Using compliant transmissions as a countermeasure can be inefficient in transferring actuators power to the links for fast motion in free space, unless joints stiffness is made variable during the execution of the task [36, 45]. In this regards, the Safe Brachistochrone problem aims at finding the minimum time required to move between two fixed configurations such that an unexpected impact would guarantee a defined safety level at any instant. The solution to this optimal control problem suggests the need of low stiffness-high speed and high stiffness-low speed movements [34, 45].

For a rotational mechanical system the output mechanical impedance can be defined as the torque τ produced in response to an imposed motion θ. In the Laplace domain the mechanical impedance can be written as the transfer function

$$Z(s) = \frac{\mathrm{T}(s)}{\Theta(s)} \tag{3.1}$$

in which $T(s)$ and $\Theta(s)$ are the Laplace transforms of τ and θ, respectively.

The simplest solution to reduce mechanical impedance with respect to traditional stiff robots consists in adopting control schemes to render desired dynamical properties in the interaction with the environment, e.g. mimicking desired visco-elastic characteristics and possibly using force feedback.

This active control approach provides a limited level of safety due to possible sensors failure, to bandwidth limitations or to stability issues. On the other hand, the introduction of passive mechanical components gives the great advantage of reducing the impedance of robotic systems intrinsically, i.e. across the whole frequency spectrum. In chapter 2 an example of force control limitation was presented based on [28] showing stability issues in coupling robots and interacting systems[1]. Using a similar method, in [32, 47] it was demonstrated that adding series dynamics can improve interaction both by altering the actuator structure to make it more closely resemble a target system, and by allowing more 'aggressive' force feedback.

The interposition of a compliant element between an actuator and its load was originally presented in [48, 49] in studies on legged locomotion. The proposed prototype, indicated as Series Elastic Actuator (SEA), was a linear actuator but a number of rotary systems have been developed in recent years [50, 51, 52, 53, 54, 55, 56, 57, 58, 59] (more details will be provided in chapter 4).

This approach provides several advantages:

- intrinsic compliance allows shock tolerance and safety during impacts;
- simple and high fidelity force control can be implemented using as feedback signal the measurement of the elastic element deflection;
- the effects of stiction, friction, backlash and other nonlinearities are reduced;
- work and power output of the actuator can be increased if an appropriate series elasticity is selected according to a specific task;
- in cyclical and/or explosive tasks efficient energy storage/release can be achieved.

In Fig. 3.1 a schematic representation of a general SEA torque control approach is reported.

[1]Stability problems typically arise when a robot contact stiff environments [28].

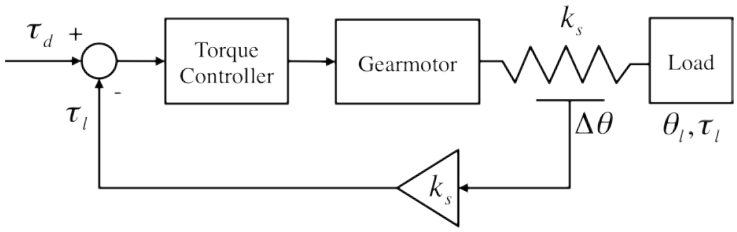

Figure 3.1: General torque control approach for rotary SEAs, adapted from [47]. τ_d is the desired torque, τ_l is the actual torque, θ_l is the output rotation, k_s is the spring stiffness and $\Delta\theta$ represents its deflection. The controller acts on the torque error considering as feedback signal the delivered torque estimated from the measurement of the spring deflection.

Nevertheless, series elasticity causes a degradation of performances in terms of control bandwidth with respect to traditional rigid actuation systems [47]. This limitation can be overcome using elastic elements whose properties can be varied during operation. The aim of independently regulating motion and impedance field to improve performances as well as to stably controlling robots interaction forces with external agents paved the way to the development of *Variable Stiffness/Impedance Actuators* (*VSA/VIA*), which are achieved by means of redundant actuation solutions, i.e. including a number of active elements higher than the number of actively controlled DOF.

The aforementioned application fields can benefit from a simultaneous and decoupled control of both motion and impedance of robotics joints, thus possibly requiring redundant actuation solutions.

In this chapter a classification and a comparison of rotary double actuation units is presented, analyzing pros and cons of different architectures and describing some representative state-of-the-art prototypes. This kind of analysis can serve as a reference criterion for new designs of actuators according to the requirements of different application fields.

It is worth noticing that the presented analysis will involve also several preliminary works presented in recent international conferences. This choice is motivated by the necessity of reporting also about latest activities in the rapidly growing research

field of variable impedance actuation.

3.1 Classification of double actuation units

Reducing the problem to its lowest terms, there are two ways to connect two actuators to a load: in serial or in parallel configurations (Fig. 3.2). According to the most commonly accepted definition of series and parallel in mechanical systems [60], a configuration is of serial type if the generalized displacement of the output link is obtainable by algebraic sum of the generalized displacements of the two actuators. On the contrary, a configuration is parallel if the torque applied to the output link is obtainable by algebraic sum of the torques applied by the two actuators. These basic possibilities can be varied to achieve a number of profoundly different configurations, by employing different kind of transmissions or introducing compliant elements.

Despite the incredibly high number of configurations that can be theoretically devised by arranging two motors and some elastic components [61], the focus of this work will be only on state-of-the-art systems, which have been proved to be effective and relevant.

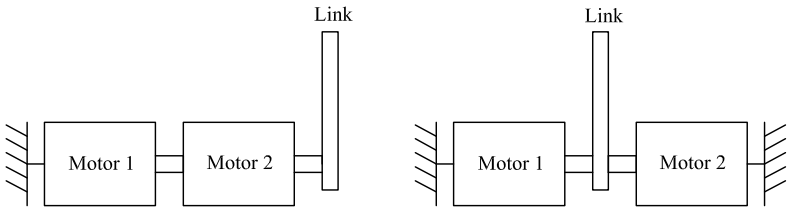

Figure 3.2: Serial (a) and parallel (b) arrangements of two actuators.

Two types of serial connections can be achieved: *purely serial* (Fig. 3.3a-d) and *quasi antagonistic* [36] (Fig. 3.3e-f). In the first case the output of one motor is the input for the other one, whose output is connected to the load. Both of them can be *ordinary* (Fig. 3.3a, c, e), for a direct connection, and *differential* (Fig. 3.3b, d, f), if the same connectivity between the elements is achieved through a differential transmission. Parallel connections can be classified in: *purely parallel*

(Fig. 3.4a-d) and *agonistic/antagonistic* (Fig. 3.4e-g). In the first case an *colocated* configuration implies a direct connection of both motors to the load (Fig. 3.4a, c), while in a *distributed* one the outputs of the motors are coupled and only one of them is directly connected to the load (3.4b, d). Agonistic/antagonistic architectures can be further distinguished in *simple*, *cross coupled* and *bidirectional* [37] (Fig. 3.4e, f, g respectively).

Therefore, purely serial and purely parallel solutions can be *elastic* or *rigid* if respectively they use or not compliant components.

While in agonistic/antagonistic architectures the two motors (and their series elasticity) are antagonistically coupled, in quasi-antagonistic configuration only the springs are antagonist while the motors are serially coupled. In particular, the simple agonistic/antagonistic arrangement (Fig. 3.4e) represent the parallel connection of two SEAs.

This classification is schematically resumed in Fig. 3.5.

SERIAL ARCHITECTURES

Purely serial configuration

	Ordinary	Differential
Rigid	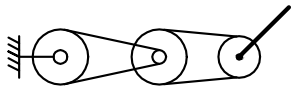 (a)	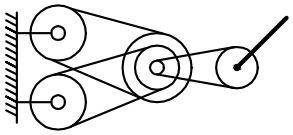 (b)
Elastic	 (c)	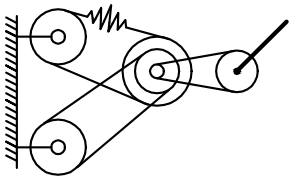 (d)

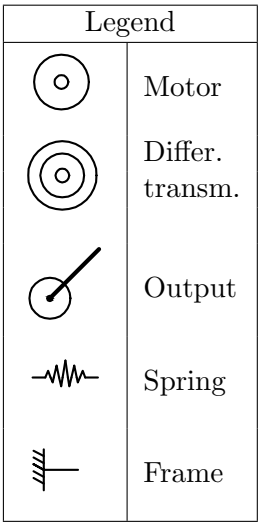

Quasi antagonistic configuration

	Ordinary	Differential
	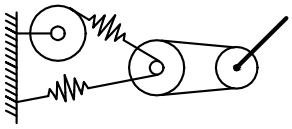 (e)	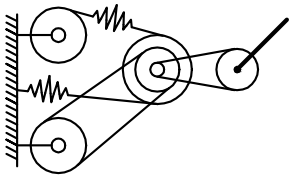 (f)

Figure 3.3: Serial architectures. In the differential transmission symbol the smallest circle is the output while the outer circles are the two inputs. The represented springs are in general nonlinear.

Nevio Luigi Tagliamonte

PARALLEL ARCHITECTURES

Purely parallel configuration

	Colocated	Distributed
Rigid	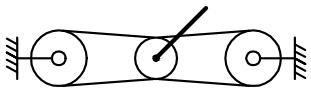 (a)	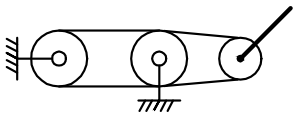 (b)
Elastic	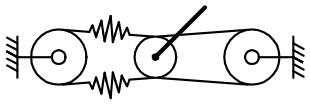 (c)	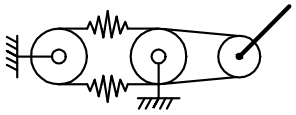 (d)

Agonistic/antagonistic configuration

Simple	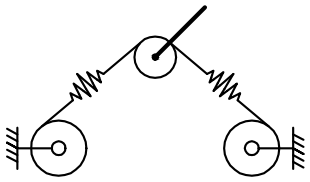 (e)
Cross coupled	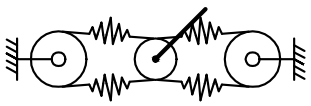 (f)
BIdirectional	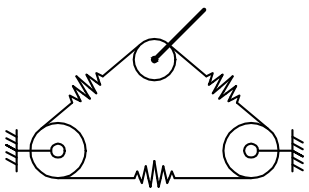 (g)

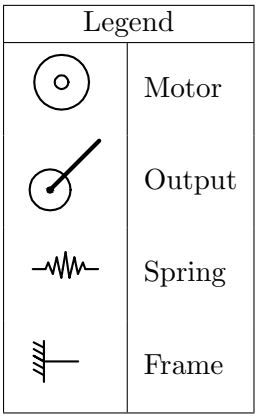

Figure 3.4: Parallel architectures. The represented springs are in general nonlinear.

The following sections will be focused on analyzing the different arrangements cited above, and on describing representative prototypes implementing the presented architectures.

Moreover, a third category can be identified, which cannot be properly classified as serial or parallel configurations: *Physically controllable impedance* actuators consists of all systems in which one of the two motors is employed to modify the mechanical properties of a passive elastic element. Possible solutions are exhaustively classified and described in [62] (where a further distinction is made between structure controlled and mechanically controlled impedance) but some examples will be also reported here. Also variable damping actuators will be touched on.

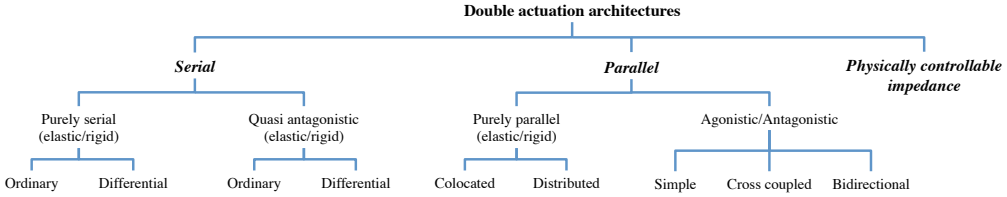

Figure 3.5: Classification of double actuation architectures.

3.1.1 Serial configuration

In the serial configuration two motors can be used to control the position and the impedance simultaneously and independently [63]. The drawback of this configuration is that the maximum torque is limited by the smallest motor. As previously remarked, a particular implementation of the serial configuration consists in using a differential mechanism. This principle is also reported in [64] where a rotary SEA is implemented through a Harmonic Drive gear in differential mode (Differential Elastic Actuator, DEA).

In the serial connection of two motors, one can be used to provide a variable series elasticity. This can be regarded as a direct extension of the SEA concept, which allows to overcome some of the limitations due to a fixed compliance. However, if no physical compliant elements are introduced in the actuation system, most of SEAs advantages cannot be exploited (see section 3). In the following sections purely serial

and quasi antagonistic configurations (both of them in an ordinary and differential implementation) will be described through some examples.

3.1.1.1 Purely serial - ordinary

The Double Actuator Joint (DAJ, [43]) consists of two motors connected in series: one of them commands the equilibrium point of the joint which is connected to (positioning motor) and the other one modulates the joint stiffness (stiffness control motor). The DAJ represents a *rigid* implementation of the ordinary purely serial configuration.

With this system an EP control scheme is implemented to obtain a human arm-like behavior. Therefore, the contact force with an external object can be controlled either by regulating the distance between the equilibrium point and the contacting surface or by modulating the compliance through the stiffness control motor.

In Fig. 3.6b it is reported a 2-DOFs master-slave manipulator with the DAJ mechanism [43]. The DAJ mechanism is implemented on the slave arm, while single actuators are placed on each joint of the master arm.

At each joint axis, there is a stack of three layers (base, positioning, and compliant layers); positioning motor connects base and positioning layers while stiffness control motor connects positioning and compliant layers. If the second and third layers are locked the robot arm works in a conventional position control mode.

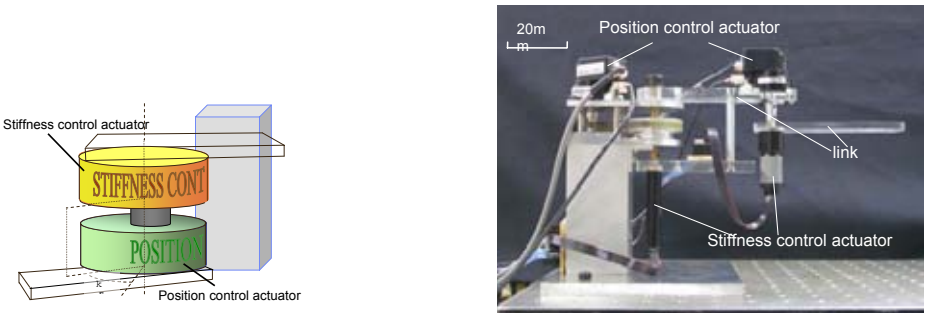

(a) (b)

Figure 3.6: Serial connection of the positioning motor and stiffness control motor for the DAJ (a) and components of the two-linked robot arm with the DAJ (b) [43].

The Floating Spring Joint (FSJ, [65]) is an *elastic* version of the ordinary purely serial architecture. In Fig. 3.7a a conceptual diagram is reported.

The Joint Motor (for position regulation) uses a Harmonic Drive (HD) as reduction gear; its output is serially connected to a Variable Stiffness Mechanism (VSM), which is composed by two cam disks separated by cam rollers and connected by a pre-compressed linear spring. The relative rotation of these two disks causes an elastic torque when the joint is passively deflected; the stiffness preset is regulated by a Stiffness Motor by modifying the initial relative rotation of the disks.

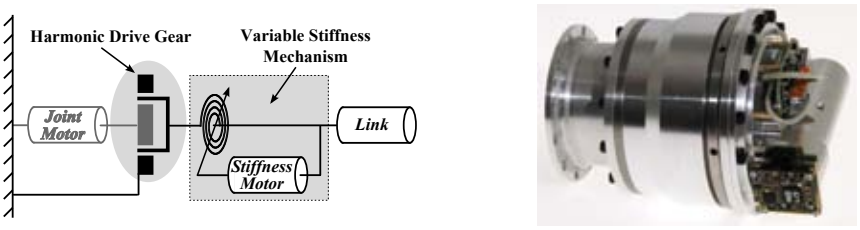

(a) (b)

Figure 3.7: Conceptual diagram (a) and prototype (b) of the FSJ [65].

3.1.1.2 Purely serial - differential

The SDAU (Serial-type Dual Actuator Unit, [63]) is a rigid implementation of the purely serial differential configuration, where two motors are connected in series via a four-stage planetary gear train. One high-torque low-speed motor (Position Actuator, PA) controls the position and the other low-torque high-speed motor (Stiffness Modulator, SM) regulates the stiffness.

Because of the serial connection, the angular displacement of the SDAU, θ_{DAU}, can be expressed as $\theta_{DAU} = \theta_{PA} + \theta_{SM}$, being θ_{PA} and θ_{SM} the rotations of the PA and of the SM respectively. The joint stiffness, k_{DAU}, is:

$$k_{DAU} = \frac{(1/r_{PA})^2(1/r_{SM})^2 k'_{PA} k'_{SM}}{(1/r_{PA})^2 k'_{PA} + (1/r_{SM})^2 k'_{SM}} \approx \left(\frac{1}{r_{SM}}\right)^2 k'_{SM} \tag{3.2}$$

being r the reduction ratio of the considered gearmotor and k' its stiffness before reduction. The approximation in (3.2) is due to the condition that $r_{PA} \gg r_{SM}$.

Nevio Luigi Tagliamonte

This implies that the output stiffness can be modulated by varying only the stiffness of the SM, and does not depend on the stiffness of the PA, thus decoupling the control problem.

In Fig. 3.8 the prototype of SDAU is shown.

Figure 3.8: Prototype of the SDAU (a) and internal view of the planetary gear train (b) [63].

An external force exerted on the link attached to the SDAU shaft causes the SM to rotate. The joint torque can be estimated as $\tau_{DAU} = \tau_{SM} = k_{SM}\theta_{SM}$ since the joint stiffness k_{SM} is set by the user and the angular displacement can be measured using an encoder.

Moreover, the SDAU architecture allows to switch among three operation modes [63]: dual actuation (PS controls the position and SM adjusts the stiffness), high torque (a clutch mechanism locks SM and only PA is activated) and high velocity (both motors play the role of position controller and their velocity can be summed if a small external load is applied).

The features of a differential Harmonic Drive (HD)[2] are exploited in the VS-Joint (Variable Stiffness Joint) presented in [66] to regulate position and physical stiffness preset separately. In Fig. 3.9 a conceptual diagram and a picture of the prototype are reported. In the VS-Joint a high power Joint Motor is connected to the WG for position regulation, a VSM is connected to the CS and the output link is connected to the FS. The VSM is composed of four compression springs whose linear deflection is transformed by a cam-based system in a centering torque against the compliant joint deflection. A small Stiffness Motor regulates the springs preload to change the

[2]More details on the use of Harmonic Drive in Differential mode will be provided in the sections 3.4.2.1 and 3.4.3.1.

resultant joint stiffness.

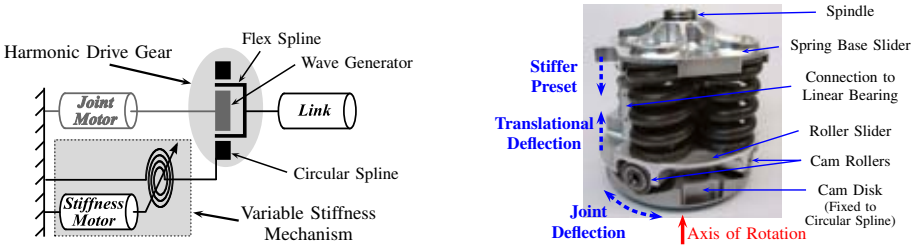

(a) (b)

Figure 3.9: Conceptual diagram (a) and prototype (b) of the VS-Joint [66].

In case of a passive deflection of the joint the positioning motor does not move and the output impedance is only determined by the VSM. On the other hand, the torque of an active joint movement is transferred to the link directly from the positioning motor to the output without additional friction and inertia of the VSM. Different shapes of the the cam disk profile can be used to provide different stiffness characteristics of the VSM.

3.1.1.3 Quasi antagonistic - ordinary

The AMASC (Actuator with Mechanically Adjustable Series Compliance) is presented in [67]. A prototype is depicted in Fig. 3.10(a). In this actuator two motors are coupled in a quasi-antagonistic configuration, using pulleys and cables. The AMASC system has been specifically designed to adjust the dynamical properties of legged robots. In Fig. 3.10(b) a schematic overview of the AMASC is given. The springs F_Y are linked to floating pulleys to create a nonlinear spring function ($G(z)$ is the pulley transmission function between the extension of the cable z and the spring deformation y). The link to be actuated (leg) is placed on pulley J_2. One motor controls the rotation θ_1 of pulley J_1 (which corresponds to set the equilibrium position of the system with a costant stiffness) and a second motor controls the displacement x_3 resulting in a deformation of the springs and in the regulation of the output stiffness.

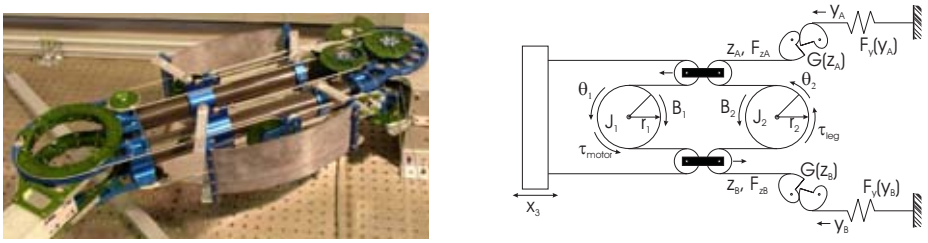

(a) (b)

Figure 3.10: Prototype (a) and schematic diagram (b) of the AMASC [67].

3.1.1.4 Quasi-antagonistic - differential

The Quasi Antagonistic Joint (QA-Joint, [68]) is similar to the VS-Joint since it employs a HD in differential mode with a VSM connected to the CS. From a comparison between Fig. 3.11a and Fig. 3.9a it can be noticed that the VSM of the QA-Joint is composed of two antagonistic nonlinear spring elements, while the one of the VS-Joint has not this antagonistic arrangement.

The compliant system consists of two progressive elastic elements opposing each other with a variable offset. A cam bar is connected to the CS of the HD; two pairs of rocker arms with cam rollers, each pair linked by a linear spring, act on different faces of this cam bar. A pair of rocker arms is fixed to the housing while the other pair is connected to a stiffness motor, which can modify springs pretension. A scheme of the elastic mechanism is reported in Fig. 3.11b. The use of the cam-roller mechanism allows to achieve different torque/displacement characteristics modifying the shape of the cam profile.

Due to the above-mentioned characteristics of the HD gear, output link position can be changed without implying any motion of the elastic mechanism, thus reducing the moving parts of the joint. It is noticeable that this advantage, already seen for the VS-Joint, is not present in the FSJ where the HD is not used in differential configuration.

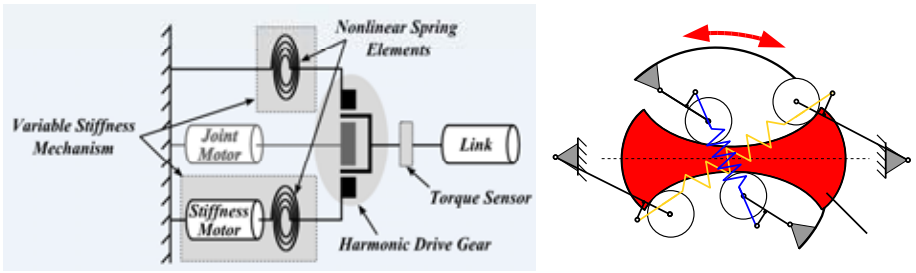

(a) (b)

Figure 3.11: Conceptual diagram of the QA-Joint (a) and working principle of its Variable Stiffness Mechanism (b) [68].

3.1.2 Parallel configuration

Two motors connected in parallel imply that the output torque equals to the algebraic sum of the torque applied by each of the two motors. This can be achieved through two main configurations. The *purely parallel* one is basically used to meet safety and performance demands (as described in the following section) while the *agonistic/antagonistic* one allows a simultaneous regulation of position and stiffness taking inspiration from the working principle of the musculoskeletal system in vertebrates.

Dynamic control of joints stiffness is crucial for animals to produce a wide range of stable movements in accordance to tasks they have to perform, especially in environments where external disturbances are present. Independent stiffness and position regulation are enabled by the antagonistic arrangement of the musculoskeletal system: agonist and antagonist muscles drive one articulation and common-mode actuation, i.e. the co-contraction of both muscles, increases joint stiffness while differential-mode actuation allows position control.

Many robotic actuation solutions have been inspired by biological agonistic/ antagonistic setup. This actuation architecture implies two significant drawbacks: the necessity of using complex control algorithms to achieve the desired behaviors and a reduced energetic efficiency. Different configurations have been proposed: *simple*, *cross coupled* and *bidirectional*. Some examples are presented in the following section; more details, also regarding energetic considerations, can be found in [37], where this

classification was introduced.

3.1.2.1 Purely parallel - colocated and distributed

In the purely parallel colocated configuration two motors are directly connected to the load. The *colocated* architecture (see Fig. 3.4a) does not offer advantages if transmissions are rigid since the same effect can be achieved through a single motor with a double torque, which would result in a more compact and lightweight design solution.

In [69] a *distributed* approach (see Fig. 3.4b) was proposed to assure desired interaction forces during constrained motion in robotic manipulators. In particular, a *rigid* macro/micro manipulation system was developed to verify the possibility of reducing impedance and of providing inherently stable behaviors in high bandwidth force control.

The Distributed Elastically Coupled Macro-Mini Parallel Actuator (DECMMA [70], previously called Distributed Macro-Mini, DM^2, architecture) adds series elasticity to the one presented in [69] (see Fig. 3.4d). This architecture (Fig. 3.12) was designed to overcome both the safety limitations of torque control [71] and the performance limitations of SEAs [48]. The implementation of joint torque control provides near-zero impedance only within the control bandwidth, thus high-frequency impacts cannot be attenuated. The SEA provides low output impedance across the whole frequency spectrum but with bandwidth limitations that strongly reduce performances with respect to traditional stiff actuators. The DECMMA approach overcomes these limitations using a high torque-low frequency SEA and a low torque-high frequency motor connected in parallel. In this way the torque generation is partitioned into low- and high- frequency contributions with low impedance at all frequencies. The two motors are located in different districts where they are most effective (distributed architecture): the heavy and high torque SEA (the major source of actuation effort) is placed remotely from the manipulator joint so to reduce its reflected weight and inertia while the small low torque motor can be directly connected to the joint through a stiff, low friction transmission to locally improve performance with a reduced amount of additional weight.

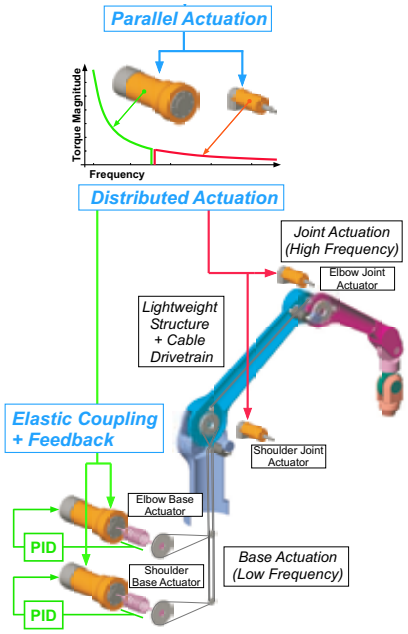

Figure 3.12: Representation of the DECMMA approach [70].

The PaCMMA (Parallel-Coupled Micro-Macro Actuator, [72]) is a compact implementation of the DECMMA approach (see Fig. 3.13).

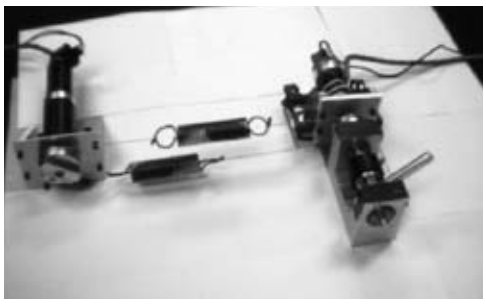

Figure 3.13: Prototype of the PaCMMA [72].

3.1.2.2 Agonistic/antagonistic - simple

The simple agonistic/antagonistic arrangement actually consists of two SEAs connected in parallel to an output shaft (see Fig. 3.4e). It has to be noticed that, in order to have adaptable stiffness, the two series elastic elements have to be nonlinear

[62, 73]. Quadratic springs in an antagonistic configuration, for example, provide a linear relationship between actuator co-contraction and joint stiffness [74]. Due to this nonlinearity a joint displacement under the equilibrium state of low stretching requires small torques while the equilibrium state under high stretching requires large torques to provide the same angular displacement.

If the torques generated by the two motors have different signs and the same magnitude they compensate for each other and no net output torque is generated; however, these opposing torques allow controlling the stiffness of the joint (*pretensioning of the joint* [75]). Therefore, if torques of different magnitude are applied, their difference generates a torque on the load.

Several prototypes have been designed which implement the simple agonistic/antagonistic architecture. Four representative examples are reported in Fig. 3.14 [76, 77, 78, 79, 80]. These prototypes constitute the elementary implementation of the simple agonistic/antagonistic arrangement; a more complex solution is represented by the Variable Stiffness Joint (VSJ) proposed in [81].

In this system two actuators are connected in parallel and a compliant linkage provides the possibility to vary the output stiffness. The linkage consists of four leaf springs connected to a central axis and four pivots that slide along each spring thanks to rolling elements (Fig. 3.15). Four 4-bar linkage systems transmit the rotation of two motors to the pivots (Fig. 3.15); they rotate together with the motors when they move in the same direction and with the same speed. In this case the distance to the axis from the pivots does not change and the stiffness is kept constant. The effective length of the springs changes when the motors rotate in opposite directions, thus varying the joint torsional stiffness.

This symmetric architecture allows to share between both motors the power to move the load or to change the stiffness. Even though the working principle is based on the physical modification of elastic components, the system is classified as agonistic/antagonistic since the net action on the output axis results from the differential contribution of the two parallel motors.

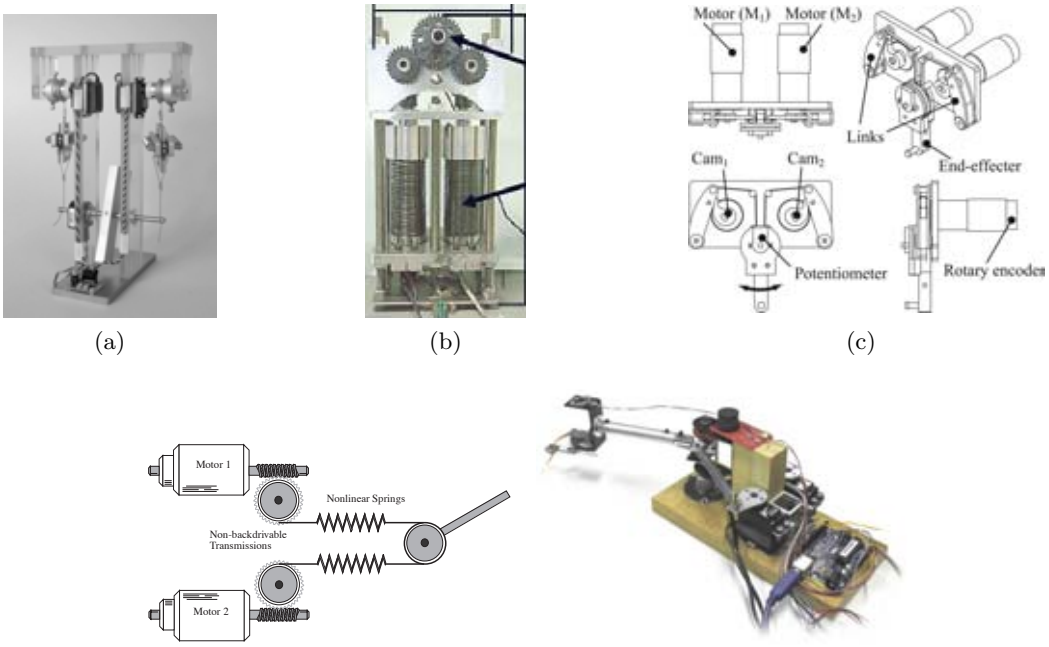

(a) (b) (c) (d) (e)

Figure 3.14: Representative examples of simple agonistic/antagonistic actuation. Prototype of Migliore et al. [76] (a); prototype of the ANLES (Actuator with Non-Linear Elastic System) [77] (b); drawing of the system using KTM (Kinematic Transmission Mechanism) presented in [78] (c); schematic drawing of the system proposed in [79] (d); prototype describe in [80] (e).

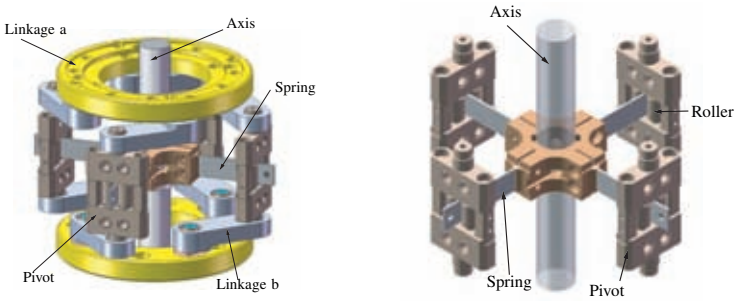

Figure 3.15: VSJ compliant mechanism [81]. Four leaf springs are attached to a central axis; four pivots sliding along the springs cause a change in stiffness. Four 4-bar linkage systems transmit the motors rotation to the pivots.

Nevio Luigi Tagliamonte

3.1.2.3 Agonistic/antagonistic - cross coupled

Simple agonistic/antagonistic configuration emulates muscles architecture (see Fig. 3.4e). Since only pull modality is allowed, the maximum output torque cannot be higher than that of one motor; moreover, no net output torque is available if the maximum stiffness is set ([37, 75]). The elastic couplings existing between different human joints suggest a solution to this limitation: the introduction of a third elastic element (see Fig. 3.4f) to cross couple the two motors enables setting preload forces and using a fraction of each motor torque in both directions [82].

The VSA (Variable Stiffness Actuator) presented in [83] is an example of the *cross coupled* agonistic/antagonistic configuration. In Fig. 3.16a a schematic view of the system is reported. The pulleys 2, 3, and 4 are connected by the belt 1. Pulleys 2 and 3 are controlled by two motors, while pulley 4 is connected to the joint shaft. The belt is tensioned by the elastic mechanisms 5, 6, and 7. The linear elastic elements 5 and 6 have a resultant nonlinear characteristic because of the geometric properties of the transmission mechanism. The system 6 keeps the belt in contact with the other two pulleys. When the two motors rotate in opposite directions the stiffness is varied. Starting from the red configuration in Fig. 3.16b, a clockwise rotation of pulley 3 and a counterclockwise rotation of pulley 2 cause the compression of spring 6 and the elongation of springs 5 and 7, resulting in a more compliant configuration (green in Fig. 3.16b). When the two motors rotate in the same direction the length of the springs does not change so that only the equilibrium position is varied.

(a) (b)

Figure 3.16: Drawing of the VSA (a) (the motors are connected to pulleys 2 and 3) and detail of the transmission belt and pulleys (b) [83].

3.1.2.4 Agonistic/antagonistic - bidirectional

Another solution to overcome the energetic limitations of simple agonistic/ antagonistic architecture consists in using the push-pull configuration, i.e. a *bidirectional* connection of the motors to the joint [82] (see Fig. 3.4g). It has to be noticed that, in order to guarantee that motor continuously apply bidirectional torques to the output joint, the springs have to be constantly pretensioned.

This arrangement, besides allowing the simple antagonism operating mode (as previously described and also indicated as *normal mode*), also enables the motors to support each other increasing torque capability of the system (*helping mode*) [75].

The normal mode assures a broad stiffness adjustment range for low external torques; the helping mode allows the generation of an output torque up to twice the maximum torque of a single motor (in case no pretensioning internal torque is generated), still maintaining stiffness variation capability. Anyhow, the helping mode does not activate if no external torque is applied.

An external load can be shared by the two motors in different ways: output stiffness can be varied by regulating the ratio of the torques applied by the two motors. Therefore, the limitations to the range of allowable stiffness are provided by the following situations: *i)* maximum stiffness is achieved when only one motor completely compensates for the external load, generating its highest allowable torque; *ii)* minimum stiffness is achieved when the load is equally shared between the motors.

The properties of the bidirectional agonistic/antagonistic, with particular regard to the helping mode, are analyzed in detail in [75], where also a method to synthesize stiffness curve to ensure stiffness variation capability in bidirectional mode is presented. The proposed approach is also evaluated on a bidirectional antagonistic testbed, which is reported in Fig. 3.17.

The second version of the Variable Stiffness Actuator (VSA-II, [82]) is an example of *bidirectional* antagonistic arrangement. A picture of the prototype is reported in Fig. 3.18a. The system is made of two equal halves, each containing a pair of 4-bar elastic mechanisms (each pair is actuated by one motor). The schematic representation of a 4-bar mechanism is depicted in Fig. 3.18b; the motor is connected in O and its rotation is indicated with θ. A linear torsion spring k is connected in C

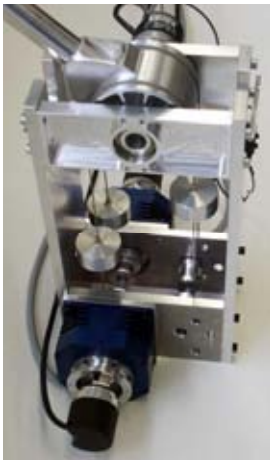

Figure 3.17: Bidirectional antagonistc joint testbed presented in [75].

and β is the transmission angle in A. Because of the nonlinear kinematic constraint between angles θ and β the torsion stiffness opposed to the rotation of axis O is also nonlinear.

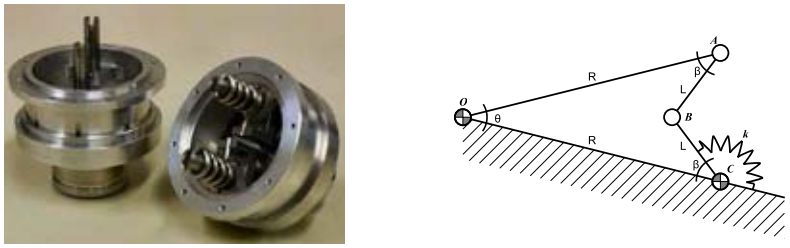

(a) (b)

Figure 3.18: Open VSA-II prototype (a) and schematic representation of a 4-bar elastic mechanism (b) [82].

In Fig. 3.19 the assembled prototype is shown; the two motors are connected to the upper and lower halves of the transmission system. Two motors, each connected to a pair of 4-bar mechanisms (i.e. a pair of nonlinear torsion springs), implement the bidirectional antagonistic architecture.

The motor torques is distributed in stiffness regulation and net output torque; this distribution is different for the VSA and VSA-II, albeit for both architectures the external load decrease the stiffness range [82]. In the first system a differential

torque is required to achieve the minimum stiffness thus reducing the torque available for the motion generation. In the second system the minimum stiffness can be set without generating any differential torque. Moreover, an external torque increases the maximum stiffness in the case of VSA while it decreases the stiffness in the case of VSA-II [82].

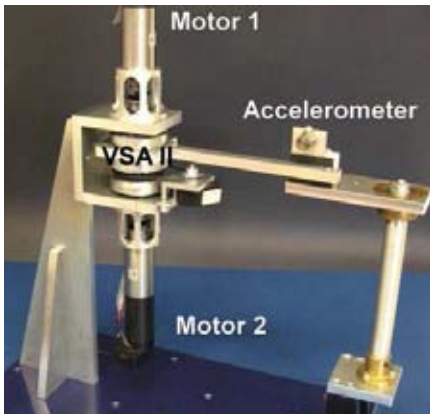

Figure 3.19: VSA-II prototype and experimental set-up [82].

3.1.3 Physically controllable impedance actuators

Solutions which cannot be just considered as serial nor parallel arrangements are described in this section. In *physically controllable impedance* systems one of the two motors is employed to directly modify the properties of a passive elastic element while the other one is in charge of regulating position. A detailed classification and description of these kind of solutions is reported in [62].

In actuators with *structure controlled stiffness* [62] the physical structure of a spring is modified, for example, varying the length of an elastic beam as for the Mechanical Impedance Adjuster (MIA, [84]) or varying the number of active coils in a helical spring as in [85] or in the Linear Adjustable Stiffness Artificial Tendon (LASAT, [86]); in actuators with *mechanically controlled stiffness* [62] the effective physical stiffness of the system is also changed, but the full length of the spring is always used.

In the Mechanically Adjustable Compliance and Controllable Equilibrium Position Actuator (MACCEPA, [87]) the stiffness variation is achieved by changing the pretension of a spring. The MACCEPA 2.0 [88]) is an improvement version of this prototype.

A profile disk is placed on the joint and it is directly connected to a linear spring through a wire. A motor rotates the profile disk and the wire is guided over the profile causing the extension of the spring and the generation of an elastic torque (Fig. 3.20). A desired (even direction-dependent) torque-angle curve can be achieved opportunely shaping the disk profile. With reference to Fig. 3.20b, the extension of the spring is due to the variation of α (the angle between the profile disk and the output link), and the setting of the pretension P. By changing the pretension, different stiffnesses can be set; moreover, the stiffness increases with increasing angle α, i.e. when the joint is moved out of its equilibrium position (*stiffening spring*). A desired torque-angle curve can be achieved opportunely shaping the disk profile, also with the possibility of a direction-dependent stiffness (asymmetric disk profile). A third version of this system (Wheeled MACCEPA), which enlarges the stiffness range, is presented in [89].

Figure 3.20: Working principle of the MACCEPA 2.0 [88].

The HDAU (Hybrid-type Dual Actuation Unit, [63]) is based on an adjustable lever arm mechanism. A modified planetary gear train (hybrid control module) is employed, where the sun gear is replaced with rack gears. The differential action of two motors connected to the inputs of the modified planetary gear train causes the

rotation of the joint (position control) and the translation, through rack gears, of linear springs blocks, thus enabling stiffness control by regulating springs engagement point.

The hybrid control module consists of two spring blocks, each composed of a linear compression spring, a linear motion block, and a roller follower (Fig. 3.21a). A modified planetary gear train with a rack-pinion mechanism is adopted as adjustable moment arm system; in particular, by replacing the sun gear with dual rack gears, the dual rack-pinion mechanism and the planetary gear train are combined into a single structure. Two 'internal ring gears' (Fig. 3.21b) are connected to the ring gear and the carrier, respectively; two motors (included in the drive module) are connected to internal ring gears 1 and 2, and their torques are transmitted to the ring gear and the carrier through transmission paths 1 and 2, respectively, as shown in Fig. 3.21b.

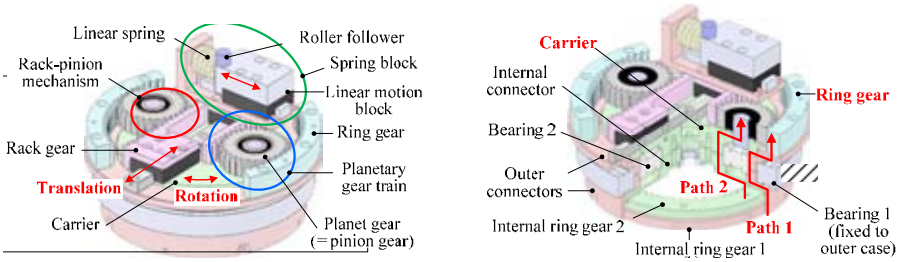

Figure 3.21: Hybrid control module of the HDAU (only one spring block is reported) [90].

A variable spring lever arm system is also used in the AwAS (Actuator with Adjustable Stiffness, [91]) where a linear drive tunes joint stiffness controlling the fixation points of two opposing elastic elements. The working principle is also similar to the one presented in [92] (Adjustable Compliant Series Elastic Actuator, ACSEA).

As reported in Fig. 3.22 motor M1 controls the position of the joint and it is rigidly connected to an intermediate link; between this intermediate link and the output link two springs are placed. The distance between the center of rotation of the joint and the attachment point of the springs (lever arm) is modified by the motor M2 through a ball screw mechanism (Fig. 3.22b).

Nevio Luigi Tagliamonte

In this system a small amount of energy is needed to change the stiffness: when the output link is in its equilibrium position the force generated by the springs is perpendicular to the direction in which the linear drive acts to modify the lever arm and only friction causes energy dissipation; when the joint is not in the equilibrium position, only a small component of the spring force is parallel to the linear drive motion.

While in the AwAS the lever arm is modified by moving the location of the springs with respect to a fixed pivot, in the AwAS-II, presented in [93], the location of the pivot is changed while the springs are fixed. With this arrangement a wider range of stiffness and a lower regulation time are achieved.

When the output link is in its equilibrium position the force generated by the springs is perpendicular to the direction in which the linear drive acts to modify the springs lever arm. In this case very low energy is needed to change the stiffness (only friction causes energy dissipation). Moreover, if the joint is not in the equilibrium position, only a small component of the spring force is parallel to the linear drive motion, hence only a small amount of energy is needed to change the stiffness.

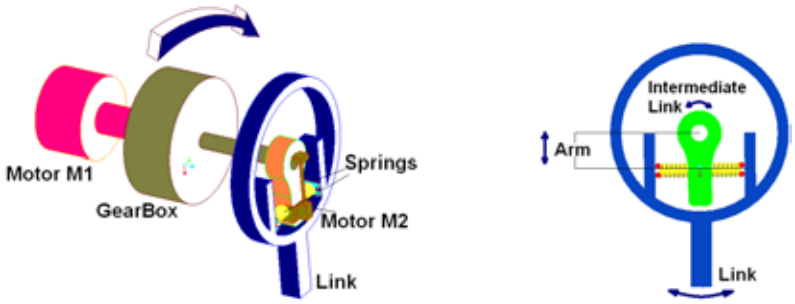

(a) (b)

Figure 3.22: Conceptual design (a) and working principle (b) of the AwAS [91].

The MESTRAN (MEchanism for varying Stiffness via changing TRasmission ANgle, [94]) is reported in Fig. 3.23. Link 1 is fixed while Link 2 rotates around O by means of a positioning motor connected to Gear 2. The rotation of Link 2 is converted in a linear motion by a Cam/Follower system. The action of the follower on the Slope-gear causes the Slope-carrier to translate and to compress a linear

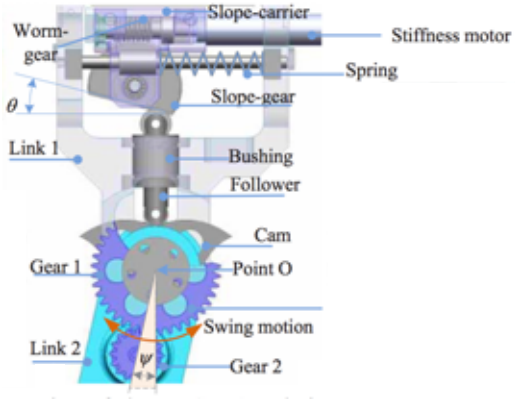

Figure 3.23: Drawing of the MESTRAN [94].

spring; this results in a perceived elastic torque around the joint O. The stiffness motor modifies through a Worm-gear the angle θ of the Slope-gear thus varying the resultant torsional stiffness of the joint.

3.1.3.1 Physically controllable dampers

Despite being classified as actuators with physically controllable impedance, the systems described in the previous sections are only employed to regulate stiffness.

Dampers are generally used to attenuate the oscillations induced in robotic systems in which compliance is introduced, especially in the case of interactions with humans [95]. Systems with fixed damping (*passive dampers*) can not adapt their dynamical actions to variations of kinematic configuration or loading conditions. Moreover, impedance control (*active dampers*) is not able to compensate oscillations at frequencies above the closed loop bandwidth. For these reasons *semi-active dampers*, i.e. systems capable of modifying their physical properties with a low amount of power, are being investigated.

Semi-active dampers based on ElectroRheological (ER) fluids or on MagnetoRheological (MR) fluids are presented in [96, 97] and [98, 99, 100] respectively. In these systems, the fluid rheological properties, and the resultant damping capability, are controlled through an applied electric or magnetic field. These solutions have typically drawbacks in terms of bulk, weight and mechanical complexity, which hinder

the integration in compact robotic joints. An alternative is constituted by friction dampers, in which the contact between moving components produces frictional forces. Damping can be modulated, for example, modifying the contact of two surfaces through piezoelectric actuators as proposed in the VPDA (Variable Physical Damping Actuator, [95]) or compressing a stack of discs as for the WDB (Wafer Disc Brake, [101]) and for the SCA (Series Clutch Actuator, [102]). These systems are clean, lightweight and they can be more easily embedded in compliant joints but they vary their mechanical properties in time due to the wear of the contacting surfaces. The damper proposed in [95] has been integrated in parallel to the compliant element of the rotary SEA presented in [51] in order to regulate oscillations when required. The resultant system (CompAct) has been described in [103].

One actuator in which position, stiffness and damping are separately regulated is the RD-Joint (Redundant Drive Joint, [104]). It consists of a serial connection (achieved through a differential mechanism based on pulleys and wires) of two subsystems: *i)* a motor with a HD gear, which sets the position of the joint; *ii)* an Adjustable Stiffness and Damping Mechanism (ASD-Mechanism), which physically regulates the impedance (both stiffness and damping) of the joint. In the ASD-Mechanism leaf springs and linear air dampers (pistons which forces air through orifices at a controlled rate) are used to provide fixed stiffness and damping; each of them is made variable by controlling the transmission ratio of its connection with the output shaft. This is achieved using two motors which modify the interconnections of linkage mechanisms. The prototype of the RD-Joint is reported in Fig. 3.24.

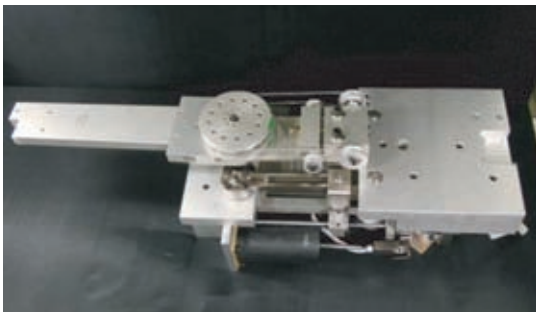

Figure 3.24: Prototype of the RD-Joint [104].

3.2 Novel approaches to dual actuation units design

An important contribution on the systematic enumeration of possible solutions to use two motors to implement variable stiffness actuators and on the analysis of the expected performances is reported in [61]. This work enumerates all possible arrangements resulting from the combination of two motors, two HD gears, one output shaft and a number of rigid or elastic elements as interconnections between these elements.

Some hypotheses have been assumed in order to reduce the magnitude of the search space and to consider only actuators ensuring the stiffness controllability. *i)* the two motors and the two HDs have the same performances in terms of torque and reduction ratio; *ii)* the motors output are connected to the WGs; *iii)* the elastic elements are nonlinear to enable a stiffness variation and they are bidirectional; *iv)* no limitation on link motion is considered; *v)* no connection can be done between the components of a single HD.

A matrix representation is used to express all the possible configurations and an automated algorithm filters out the solutions not responding to the required functional properties. A further filtering process, grouping functionally equivalent systems, highlights 22 resultant architecture, which include many of the actuators already developed and presented in the previous sections.

To verify the mechanical complexity of the layouts selected through the presented enumeration, the Modular Variable Stiffness (MVS) prototype has been fabricated (Fig. 3.25a) [61].

MVS is composed of two motors, two HDs, and a modular connection system, which allows to replicate all the connections hypothesized for the enumeration process (rigid beams and linear traction springs with lever arms are employed). Because of its mechanical simplicity, one of the possible 22 layouts has been selected and fabricated as a stand-alone system; the resultant prototype, the VSA-HD, is reported in Fig. 3.25b. In this system (VSA-HD, [61]) one of the two HDs has its FS connected to the mechanical frame through a nonlinear elastic element (as for the CS of the second HD), while its CS is connected to the output shaft through a rigid element. Moreover, the two FSs are rigidly coupled.

(a) (b)

Figure 3.25: Prototype of the VSM (a) and of the VSA-HD (b) [61].

In [105] a port-based mathematical framework for analyzing and modeling energy efficient variable stiffness actuators is presented. Based on the conditions set by the mathematical framework, the conceptual design of a novel actuator is presented, demonstrating that, in theory, the output stiffness can be varied by only modulating the transmission ratio of an ideal transmission without using any energy.

Considering a non ideal transmission an external power through an 'input port' can either be used to change the transmission ratio or to do work at the 'output port'. Some hypotheses are considered: *i)* the actuator has some internal DOFs, indicated with variables q; *ii)* the apparent output stiffness is related to the configuration of the internal DOFs; *iii)* friction is neglected; *iv)* there is no coupling between the output force and the velocities of the internal DOFs; *v)* energy can be added to or removed from the system via the input or output ports.

The design of the internal configuration should include a number of internal DOFs such that it is possible to change the apparent output stiffness while the amount of energy stored in the system does not change due to power supplied through the input port. This corresponds to decoupling position and stiffness control on a mechanical level.

Following this guideline, an actuator, whose functional concept is reported in Fig. 3.26a, was designed. The working principle is based on a linear spring connected to a lever arm of variable effective length which determines how the stiffness of the spring is felt at the output. The difference with respect to the AwAS, AwAS-II and HDAU is that, in this case, the locations of the spring and of the pivot are fixed

while the point where the end-effector acts is variable [93].

The DOF q_1 controls the transmission ratio from the spring to the end effector while the DOF q_2 directly control the end effector (which has position x). It has been demonstrated that if $\dot{q}_1$ is such that the stiffness varies as desired, and if $\dot{q}_2 = -\sin(\phi)\dot{q}_1$, the stiffness modification does not require energy. A prototype matching the conceptual system of Fig. 3.26a is reported in Fig. 3.26b.

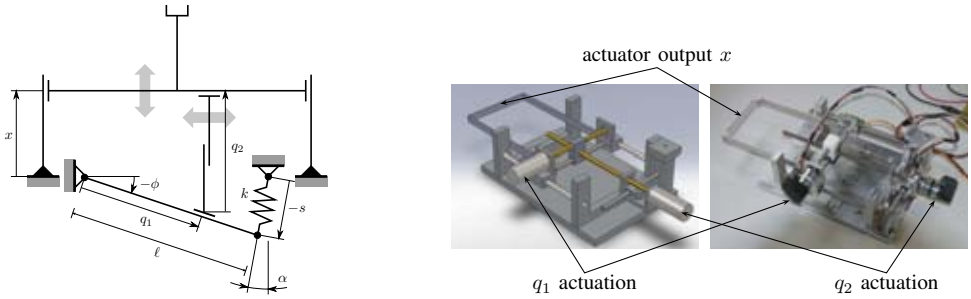

(a) (b)

Figure 3.26: Conceptual design (a) and prototype (b) of the energetic efficient variable stiffness actuator presented in [105].

3.3 Discussion and comparison

New actuation solutions have been developed in recent years to establish a safe and effective human-robot interaction in rehabilitation and assistive robotics, to increase energy efficiency in legged robots, to study human motor control in neuro-robotics, and to prevent damages to operators in industrial environments shared with robots. To this aim architectures involving more than one active element and elastic components are increasingly being investigated. The advantages of separately controlling position and impedance, according to the different application fields, can be basically resumed as the improvement of systems dynamical performances while preserving safety (e.g. Safe Brachistochrone problem [45]) or as the optimization of energetic exchanges with humans and/or external environment.

A classification of rotary double actuation systems has been introduced in this thesis, including three main categories: *serial*, *parallel* and *physically controllable*

impedance. A critical analysis of the most relevant features of each presented architecture has been carried out (see also Table 3.1). A straightforward comparison among all the presented prototypes is not easy since not all of them are optimized for the same target application, nevertheless some common traits have been identified for the introduced categories. The overview and classification of these systems can represent a general guideline for future designs of actuators in different application fields.

A critical analysis of different reported architectures highlighted that serial configurations allow the decoupling of position and stiffness controls; as a drawback, the maximum deliverable torque is limited by the smaller of the two motors.

Moreover, purely parallel configurations allow the partitioning of the generated torque in high- and low-frequency contributions; in this case the use of a SEA for low-frequency/high-torque generation guarantees low intrinsic impedance across the whole frequency spectrum. In the agonistic/antagonistic actuation architectures, complex control laws are required because the motors contemporarily contribute to control position and stiffness. Moreover, the mechanical structure is elaborate and energetic efficiency is often reduced. Nevertheless, since they reproduce the features of the muscoloskeletal system in vertebrates, they are particularly suitable for neuroinspired robotics and for neuroscientific studies on motor control.

While the above-mentioned architectures provide the possibility of regulating stiffness via software or by pre-compressing elastic elements, in actuators with physically controllable impedance the properties of a mechanical component or the way it is connected to the load can be changed. This kind of solution generally implies a complex mechanical structure but it offers the advantage of providing physical mechanical impedance adaptable to different operative conditions and suitable to improve energetic efficiency. The addition of variable dampers (e.g. ER, MR or friction systems) in actuators with variable stiffness can be useful to improve dynamical performances but it increases the complexity of the mechanical design, as for the system presented in [104] where three motors are used for position, stiffness and damping regulation. For this reason variable dampers are usually employed for joints with a fixed compliance (e.g. in [99, 103]), in traditional robots where flexible

components can cause vibrations (e.g. in [96, 97]) or in rehabilitation devices where resistive torques are needed [106, 107, 108].

Factors limiting the use of double actuation systems are inherent to the complexity of the mechanical structure and of the required control algorithms. Moreover, a considerable on-going research effort is currently being devoted to improve power-to -mass and -volume ratios and energetic efficiency, by exploiting both theoretical design tools and novel technological solutions.

In [105] a mathematical framework has been presented to assess energetic efficiency of variable impedance actuators, also demonstrating that a particular class of solutions allows to physically modulate impedance in an energetically conservative way.

Technical choices to improve the overall power-to-mass ratio can include the use of high-performance frameless electromagnetic motors (as in [50, 51, 56, 64]) or the design of custom compliant components to optimize weight and volume (as proposed in [56, 109]). An alternative to electromagnetic motors is constituted by pneumatic artificial muscles (e.g. McKibben muscles [110] or PPAMs (Pleated Pneumatic Artificial Muscles) [111]). These systems provide intrinsic compliance due to gas compressibility and to the flexibility of gas chambers but a considerable drawback is the need of external compressors. As a promising solution, research on novel energy transduction methods is leading to propellant-based chemical actuators able to directly convert chemical energy into mechanical energy [112, 113].

In wearable *assistive/rehabilitative robots*, the requirements on mass/volume are particularly strict. This is the reason why minimal actuation architectures are normally employed, possibly including passive element with fixed compliance [52, 114]. Nevertheless, biomechanical studies clearly demonstrate that the human musculoskeletal system deeply exploits the independent regulation of both position and stiffness in several tasks, including locomotion and manipulation [115, 116, 117]. Ideal actuation solutions for wearable robots should be able to replicate (in the case of *robotic prostheses*) or to harmonically co-exist with (in the case of *active orthoses*) such biomechanical systems. It is expected that in the coming years improvements on key enabling technologies for actuators will allow a widespread diffusion of double

actuation architectures in these fields.

In *legged robots* double actuation solutions are currently considered for a decoupled regulation of position and impedance inspired by animals' locomotion and for improving energetic efficiency. In this regards, the adjustment of mechanical properties of the legs can help switching among walking, running and hopping. For pseudo-passive walkers, the modification of the robot natural frequency is even more crucial to elicit stable limit cycles. The use of these actuation systems is expected not to be hindered by requirements on bulk and weight.

In *neuroscience* the use of double actuation solutions, as the agonistic/antagonistic architecture, cannot be avoided if the human/animal muscular systems have to be reproduced for motor control investigations. Restrictions on mass and dimensions are not excessively strict for the design of bio-inspired platforms validating neuroscientific hypotheses. Rather, technological solutions are becoming more and more sophisticated to reproduce the cellular array structure of muscles (for example using Shape Memory Alloys (SMAs) elements [118]) or to fabricate bio-micro-actuation units using human tissues ([119, 120]). In this sense, a thigh collaboration is expected to be established between neuro-robotics and (bio)material engineering.

In *industrial robotics*, the need of minimizing risks arising from unpredictable collisions and from the interaction during physically shared tasks is primary and cannot completely rely on control software. In this context the widespread adoption of compliant actuation, with adjustable properties for low stiffness-high speed and high stiffness-low speed motion, is likely to happen in the close future.

In general, the current research trend is moving towards the design of actuators with physically controllable impedance, i.e. highly efficient systems physically adaptable to a wide range of dynamic operative conditions. To this aim the most recent works presented in section 3.2 are devoted to the identification of novel design methodologies where mathematical tools are employed to optimize actuators performances, varying impedance in an energetically efficient way. Despite of that, translating these concepts into practical design is still an open point for future research.

Actuation architecture			General characteristics	Pros	Cons
Serial	Purely serial	Ordinary	The generalized displacement of the output is obtainable by algebraic sum of the generalized displacements of the two motors.	Decoupling of position and impedance/stiffness controls.	Maximum torque limited by the smallest motor.
		Differential			Complex mechanical structure.
	Quasi-antagonistic	Ordinary			
		Differential			
Parallel	Purely parallel	Colocated	The torque applied to the output is obtainable by algebraic sum of the torques applied by the two motors.	Torque generation can be partitioned into low- and high- frequency contributions to meet safety and performance demands.	Need of a powerful motor for high-torque/ low-frequency torque contribution.
		Distributed			
	Agonistic/ antagonistic	Simple		Simultaneous control of position and stiffness inspired by the musculoskeletal system.	Complex mechanical structure and control laws. Reduced energetic efficiency.
		Cross coupled			
		Bidirectional			
Physically controllable impedance			One motor is employed to directly modify the properties of a passive elastic element while the other one is in charge of regulating position.	Physical regulation of the impedance. Low power motor for impedance regulation. High energetic efficiency. Decoupling of position and stiffness controls.	Complex mechanical structure.

Table 3.1: Characteristics of double actuation architectures.

Nevio Luigi Tagliamonte

3.4 Design of a Variable Impedance Differential Actuator

Based on the previous analysis an actuator based on a purely serial differential architecture is presented in this section. The Variable Impedance Differential Actuator (VIDA) combines advantages of the SDAU system (see section 3.1.1.2) for separate position and impedance regulations with the ones of SEAs because of the presence of an elastic component. Virtual impedance is chosen to be rendered via an active software control instead of using physical variable impedance or stiffness presets to have a simpler and more lightweight design and to also include damping regulation. In the following sections a preliminary design is presented and a model of the system is developed to evaluate performances of the system in simulation.

3.4.1 Design requirements

The system is mainly intended for gait assistive wearable robots. Hence it is reasonable to require the actuator to have a weight lower than 2 kg and to be contained in a volume of 150×100×100 mm^3. A maximum instantaneous torque of 15 N·m (suitable to complement human joints torques in assistive conditions, e.g. 30% of lower limbs physiological torques during walking) has been selected as target. Since it is important to guarantee a high level of safety and coupled stability and to respond to high-frequency shocks deriving for example from the interaction with the ground, an intrinsically compliant element has to be included in the architecture. VIDA general design, including the overview of the architecture, a description of the control and expected performances, is presented in the following sections.

3.4.2 Design

The VIDA has a redundant actuation, with one motor (Position Regulator, PR) used to regulate the position and the second one (Impedance Regulator, IR) to modulate the mechanical impedance (stiffness and damping values can be varied). A Harmonic Drive (HD) in differential mode is used to achieve a serial connections similarly to what presented in [66]. A scheme of the VIDA architecture and

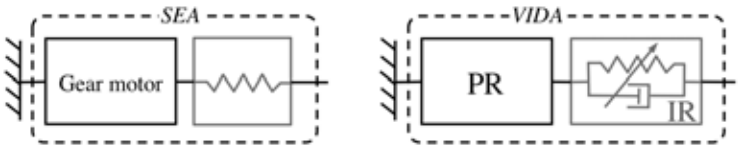

Figure 3.27: Architectures of SEA (left) and VIDA (right).

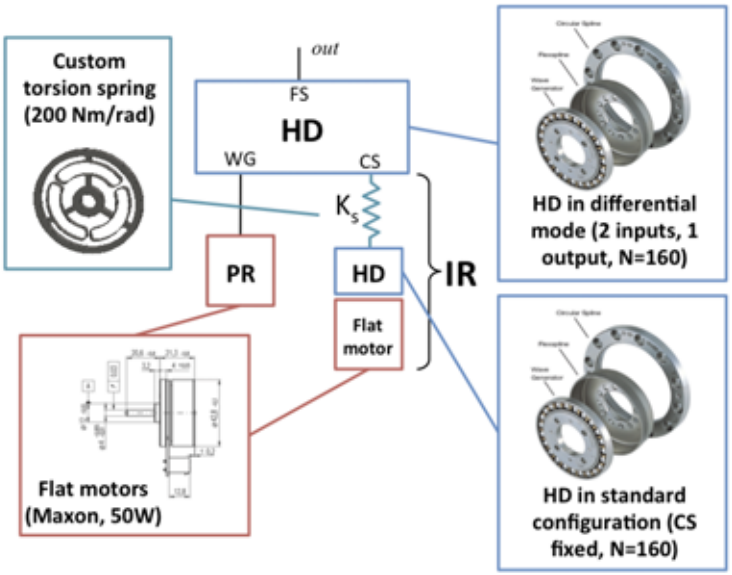

Figure 3.28: VIDA architecture and components.

a comparison with SEA architecture is reported in Fig. 3.27. In the VIDA system the series elastic element is substituted by a software-controlled variable impedance implemented through the IR.

In Fig. 3.28 the architecture and components of the VIDA are reported, whose description will be presented on the following sections.

3.4.2.1 Harmonic Drive gear - HD

In the proposed VIDA architecture the Harmonic Drive operates as a differential gear to allow a serial connection of the two motors; in particular, the Wave Generator (WG) and the Circular Spline (CS) are the inputs and the Flexible Spline (FS) is the output. The equivalent impedance seen from the output (FS) is:

$$Z_{out} = \frac{Z_{CS} Z_{WG} N^2}{(N+1)^2 Z_{WG} + Z_{CS}} \tag{3.3}$$

For high values of the transmission ratio N, $Z_{out} \approx Z_{CS}$. On the basis of this consideration, the IR is connected to the CS while the PR is connected to the WG (which has high transmission ratio with respect to the FS shaft) to get a rigid behavior. The selected gearing is the CSD-20-160-2A-GR, which has a transmission ratio $N = 160$, a weight of 130 g and a thickness of 14 mm.

3.4.2.2 Position Regulator - PR

Many manufacturers of electrical motors include flat DC motors in their catalogues, which show to be a good compromise between high torque/power and low volume/mass. A flat motor is used as Position Regulator (PR): Maxon EC45-flat, 50 W brushless DC motor with a maximum continuous torque of 84.3 mN·m, a stall torque of 822 mN·m and weight of 110 g. This motor is equipped with an incremental optical encoder Avago HEDL5540, which has a 500 counts per turn resolution (0.18 deg with quadrature readings).

3.4.2.3 Impedance Regulator - IR

The Impedance Regulator tunes the impedance field around the equilibrium position set by PR. Since a low level torque control is needed to implement an impedance control, a SEA can be used as IR, introducing advantages typical of intrinsic physical compliance presented above. For the IR the same motor and encoder as for the PR are used, with an additional reduction gear. To minimize the longitudinal encumbrance a (second) Harmonic Drive, equal to the one presented in section 3.4.2.1, has been chosen.

3.4.2.4 Passive elastic element

The selection of the spring stiffness emerges as a tradeoff between the large force bandwidth and a low intrinsic impedance: the definition of an operational bandwidth for which the actuator needs to display large forces places a lower bound, while the

upper bound is set by the need of minimizing the intrinsic impedance [47]. In our case a stiffness of 200 N·m/rad has been selected.

In order to have a lightweight and thin torsion spring a steel disc can be opportunely shaped using a FEM-based design process. Details on possible designs will be presented in chapter 4.

3.4.2.5 Torque measurement

The stiffness of the spring also influences the resolution of torque measurement. A 32768 cpt magnetic incremental encoder (sensor PMIS4 and magnetic wheel PMIR4, ASM) is placed on the FS of the differential HD so to measure the deflection of the torsion spring (by difference with the angular position of the IR motor). This choice permits to directly monitor the output shaft of the whole actuator and to estimate the torque applied by the IR with a resolution of 0.038 N·m.

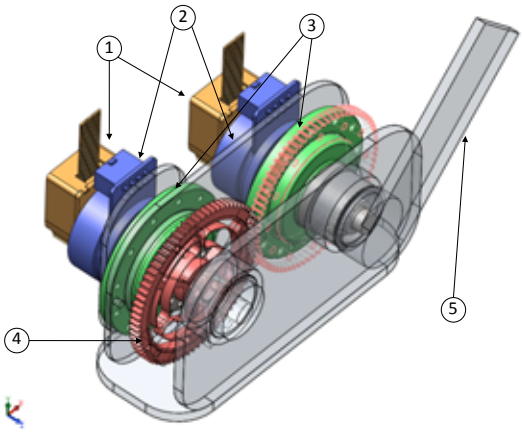

Figure 3.29: Preliminary 3D CAD drawing of the VIDA system. 1: encoders, 2: flat motors, 3: HD gears, 4: custom torsion spring, 5: output link. PR components are on the right side, IR components are on the left. Motion is transmitted through a 1:1 transmission ratio gear connecting the the series elastic element to the CS of the differential HD. The case is shown in transparency, with overall dimensions of 150×85×100 mm^3.

Nevio Luigi Tagliamonte

3.4.2.6 Overall mechanical structure

In Fig. 3.29 a preliminary 3D CAD drawing of the VIDA system is shown. The overall architecture includes two flat motors and relative encoders, two HD gears (one used in differential configuration and the other one used as a reduction gear), an encoder on the output shaft, the custom torsion spring, a 1:1 transmission ratio gear to transmit spring rotation to the CS of the differential HD.

3.4.3 Model and control

A block diagram of the whole system, comprising the HD, the IR and the PR, is reported in Fig. 3.30.

3.4.3.1 Harmonic Drive model

Modeling of Harmonic Drives in their most usual configurations has widely been investigated; the case of no fixed shaft (differential gearing configuration) has only been analyzed in [121]. The kinematic constraint on the components of the vector $\boldsymbol{\theta'} = (\theta_{WG}, \theta_{CS}, \theta_{FS})^T$ and the relation between the torques $\boldsymbol{\tau'} = (\tau_{WG}, \tau_{CS}, \tau_{FS})^T$ are:

$$\begin{cases} \theta_{WG} - (N+1)\theta_{CS} + N\theta_{FS} = 0 \\ \tau_{FS} = -N\tau_{WG} \\ \tau_{FS} = \frac{N}{N+1}\tau_{CS} \end{cases} \tag{3.4}$$

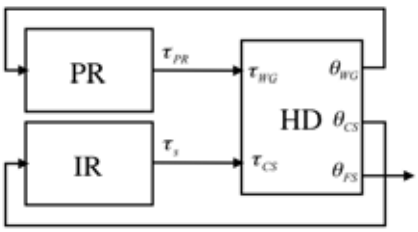

Figure 3.30: Block diagram of the VIDA. HD block implements equation (3.8). The IR block represents the model shown in Fig. 3.32. θ_{FS} represents the rotation of the load.

Nevio Luigi Tagliamonte

The dynamical model of the system is:

$$\boldsymbol{B'}\ddot{\boldsymbol{\theta}}' + \boldsymbol{C'}\dot{\boldsymbol{\theta}}' = \boldsymbol{\tau}', \tag{3.5}$$

where $\boldsymbol{\tau}'$ is the vector of the torques acting on the shafts and

$$\boldsymbol{B'} = \begin{bmatrix} J_{WG} & 0 & 0 \\ 0 & J_{CS} & 0 \\ 0 & 0 & J_{FS} \end{bmatrix} \boldsymbol{C'} = \begin{bmatrix} c_{WG} & 0 & 0 \\ 0 & c_{CS} & 0 \\ 0 & 0 & c_{FS} \end{bmatrix} \tag{3.6}$$

are the matrices of inertia and viscous damping respectively. The terms J and c indicate the inertia and damping of each shaft. Considering the kinematic constraint in the first equation of (3.4), the configuration of the system can be expressed in terms of two variables (θ_{WG} and θ_{CS}). As reported in [121], by introducing the matrix

$$\boldsymbol{R} = \begin{bmatrix} 1 & 0 \\ 0 & 1 \\ -\frac{1}{N} & \frac{N+1}{N} \end{bmatrix} \tag{3.7}$$

equation (3.5) becomes:

$$\boldsymbol{B}\ddot{\boldsymbol{\theta}} + \boldsymbol{C}\dot{\boldsymbol{\theta}} = \boldsymbol{\tau} \tag{3.8}$$

In (3.8) $\boldsymbol{\theta} = (\theta_{WG}, \theta_{CS})^T = \boldsymbol{R}^T\boldsymbol{\theta}'$ and $\boldsymbol{\tau} = (\tau_{WG}, \tau_{CS})^T = \boldsymbol{R}^T\boldsymbol{\tau}'$ are the vectors of the two independent angular and torque variables respectively; $\boldsymbol{B} = \boldsymbol{R}^T\boldsymbol{B'}\boldsymbol{R}$ and $\boldsymbol{C} = \boldsymbol{R}^T\boldsymbol{C'}\boldsymbol{R}$ are the inertia and viscous damping matrices in the independent coordinates. Considering a load connected to the FS, its moment of inertia J_L can be added to that of the FS in the matrix $\boldsymbol{B}$.

3.4.3.2 PR and IR models

Both the PR and the IR are modeled in their mechanical and electrical part, considering the moment of inertia of the rotor J, the viscous damping b and the motor inductance and resistance L and R. In the case of the PR, which is directly connected to the WG of the Harmonic Drive, the moment of inertia J_{PR} and the

viscous damping b_{PR} can be directly added to those of the WG in the matrices $\boldsymbol{B}'$ and $\boldsymbol{C}'$ respectively. In the case of the IR, a typical SEA model (such as the one presented in [47]) is considered. In Fig. 3.31 a schematization of the model in the Laplace domain is reported; K_s is the spring stiffness, τ_{IR} is the torque applied to the rotor, ω_{IR} is the velocity of the motor, τ_s is the torque applied to the CS, θ_{CS} is the rotation of the CS, V_{IR} is the voltage command, k_t is the torque constant and k_e is the back-EMF constant.

3.4.3.3 VIDA control

The regulation of the equilibrium position of the output shaft is pursued through a standard high gain PID position control of the PR. Impedance regulation is achieved by controlling the output torque of the IR. The commanded torque input at the CS shaft is:

$$\begin{aligned} \tau_{CS} &= K_v(\theta_{FS} - \theta_{FS,d}) + c_v(\dot{\theta}_{FS} - \dot{\theta}_{FS,d}) = \\ &= \left(\frac{N+1}{N}\right)^2 \left[K_v(\theta_{CS} - \theta_{CS,d}) + c_v(\dot{\theta}_{CS} - \dot{\theta}_{CS,d})\right] \end{aligned} \tag{3.9}$$

By imposing $\theta_{CS,d} = 0$, $\dot{\theta}_{CS,d} = 0$ the visco-elastic behavior of the output shaft is pursued around the current position, which is set by the PR.

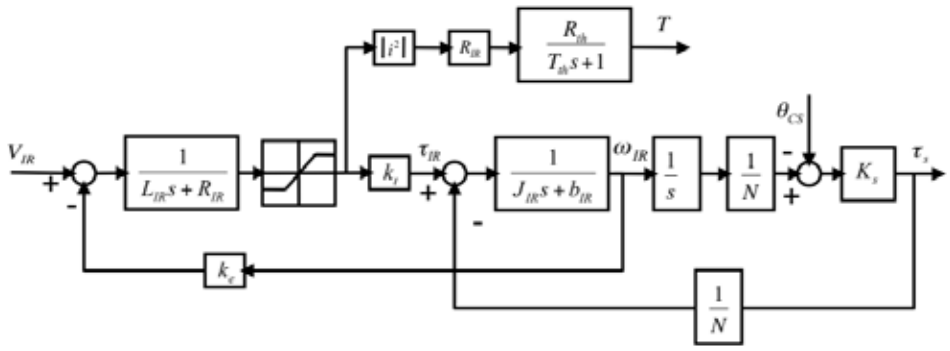

Figure 3.31: IR model in Laplace domain. The output torque is $\tau_s = K_s(\frac{\omega_{IR}}{s} - \theta_{CS}) = K_s(\theta_{IR} - \theta_{CS})$. The block with the thermal resistance (R_{th}) and the thermal time constant (T_{th}) allows to monitor motor winding temperature.

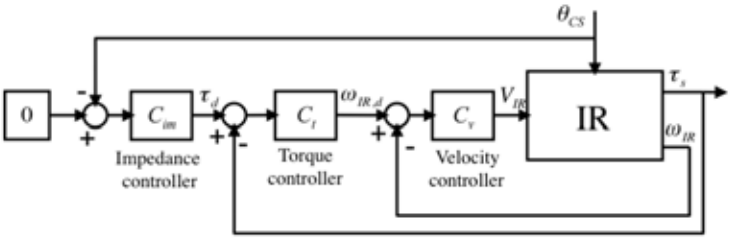

Figure 3.32: Block diagram of the IR control. IR block represents the model of Fig. 3.31. The three cascade controllers implement the transfer functions in (3.10). By imposing a 0 reference value for the impedance controller, the visco-elastic behavior of the output shaft is every-time pursued around the current output position.

The IR is controlled as proposed in [55, 122]: an inner PI velocity loop is implemented to use the actuator as a *velocity source* (*VS-SEA*) and an external loop is used to control the torque; this regulation is performed by measuring the deflection $\Delta\theta_s$ of the series elastic element (of stiffness K_s) and estimating the torque applied to the load τ_s, which is given by the relation $\tau_s = -K_s\Delta\theta_s = K_s(\theta_{IR} - \theta_{CS})$. An outer loop, closed on the load angle measurement, implements the impedance control in the form of (3.9) in order to render virtual stiffness K_v and damping c_v. The three cascade controllers are reported in (3.10); a block diagram of the control scheme is reported in Fig. 3.32.

$$\begin{aligned} C_v &= P_v + \tfrac{I_v}{s} \\ C_t &= K_t \tfrac{s^2+as+b}{s^2} \\ C_{im} &= K_v + sc_v \end{aligned} \tag{3.10}$$

3.4.4 Validation results

The model of the VIDA was implemented in Simulink/Matlab (The MathWorks Inc.). The values assigned to the parameters of the model are reported in Table 3.2.

Table 3.2: VIDA model parameters.

Parameter	Value	Units
J_{WG}	$65 \cdot 10^{-6}$	kg $\cdot$ m^2
J_{CS}	$32.9 \cdot 10^{-6}$	kg$\cdot$ m^2
J_{FS}	$3.8 \cdot 10^{-2}$	kg$\cdot$ m^2
J_l	5	kg$\cdot$ m^2
b_{WG}	$1 \cdot 10^{-4}$	N$\cdot$ m$\cdot$ s $\cdot$ rad^{-1}
b_{CS}	$8.03 \cdot 10^{-2}$	N$\cdot$ m$\cdot$ s $\cdot$ rad^{-1}
b_{FS}	$8.55 \cdot 10^{-2}$	N$\cdot$ m$\cdot$ s $\cdot$ rad^{-1}
N	160	
K_s	200	N$\cdot$ m$\cdot$ rad^{-1}
$J_{IR} = J_{PR}$	$1.35 \cdot 10^{-5}$	kg$\cdot$ m^2
$b_{IR} = b_{PR}$	$2.05 \cdot 10^{-2}$	N$\cdot$ m$\cdot$ s $\cdot$ rad^{-1}
$R_{IR} = R_{PR}$	0.978	Ω
$L_{IR} = L_{PR}$	0.573	mH
$k_t = k_e$	$33.5 \cdot 10^{-3}$	V$\cdot$ s $\cdot$ rad^{-1}
R_{th}	8.75	K$\cdot$W^{-1}
T_{th}	16.6	s

3.4.4.1 Torque control

The step response and the Bode diagram of torque control transfer function ($T_s(s)/T_d(s)$) are reported in Fig. 3.33. Even though very high bandwidth (in the order of 30 Hz for 3 dB attenuation) seems to be theoretically achievable with the selected control gains, it can be demonstrated that system saturation strongly limits deliverable torque with increasing frequency.

In particular, thermal limitations of the IR for three values of the stiffness of the elastic element are reported in Fig. 3.34. Windings temperature is calculated through a first order transfer function which takes into account the thermal resistance (R_{th}) and the thermal time constant (T_{th}) (see the block diagram of Fig. 3.31). Assuming a fixed load ($\theta_{CS} = 0$) the IR was commanded to track sinusoidal torques with frequencies (f_{tor}) from 0.1 Hz to 35 Hz; for each frequency the maximal torque amplitude (A_{tor}) before overheating (i.e. before motor winding temperature exceeds the maximum allowed temperature for standard thermal exchange conditions) was calculated. It can be seen that a higher stiffness allows to deliver higher torques (up to twice when moving from K_s=100 N·m/rad to K_s=200 N·m/rad) before the motor

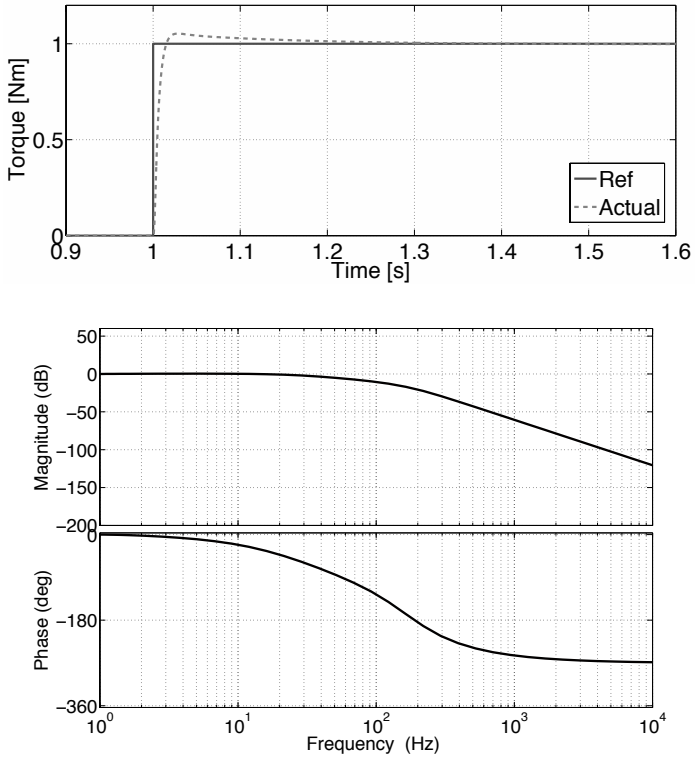

Figure 3.33: Step response and Bode diagram of the IR torque control.

overheats. The selected value of K_s=200 N·m/rad for the stiffness of the compliant element is demonstrated to guarantee a bandwidth of about 1 Hz for the desired peak torque (15 Nm), and of 3 Hz for a torque of 5 Nm which can are considered suitable for the selected application. Nevertheless, torques start becoming negligible at about 10 Hz, which can be considered the true theoretical limitation for the system (in reality other non-modeled friction, control delays and saturations contribute to a further lowering of performances).

3.4.4.2 Impedance regulation

As already highlighted mechanical output impedance is defined as the amount of torque delivered by an actuator for a given load motion. For the VIDA system the output impedance in the Laplace domain can be written as $Z_{out}(s) = T_s(s)/\Theta_{CS}(s)$. To test the capability of the VIDA (and in particular of the IR component) to

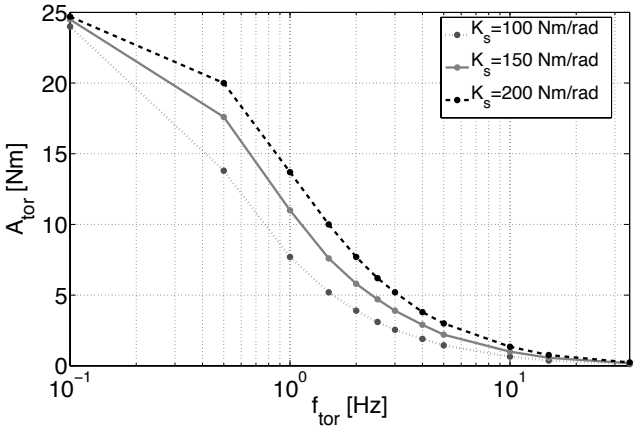

Figure 3.34: Thermal limitations of the IR for different series elastic elements (K_s =100, 150 and 200 N·m/rad). IR was commanded to track sinusoidal torque of amplitude A_{tor} and frequency f_{tor} with a fixed load ($\theta_{CS} = 0$).

render a virtual impedance, external position perturbations have been simulated. In particular, the output shaft was forced to move sinusoidally with an amplitude of 0.1 rad and a frequency of 1 Hz for different values of K_v and c_v set by the IR. In Fig. 3.35 the ideal torque (the one obtained multiplying the desired impedance and the imposed external rotation) and the actual torque (the one effectively delivered by the VIDA in response to the external position disturbance) are shown: graphs on the left represent a pure compliant behavior ($c_v = 0$ N·m·s/rad) while graphs on the right provide the response considering a non-null damping. The desired mechanical impedance can be correctly rendered except for the case of a low pure stiffness as already found in [53]. In Fig. 3.35 the case of $K_v = 10$ N·m/rad is reported; this value is more than one order of magnitude smaller than the stiffness of the physical series elastic element ($K_s = 200$ N·m/rad).

3.4.4.3 Positioning tasks

In this section the simulations of positioning tasks, for different rendered virtual impedances, are presented. In Fig. 3.36 the response of the VIDA to a step command of 20 deg is shown for $K_v = 100$ N·m/rad (top) and $c_v = 40$ N·m·s/rad (bottom). The same positioning task was simulated considering a torque disturbance; at $t = 4$

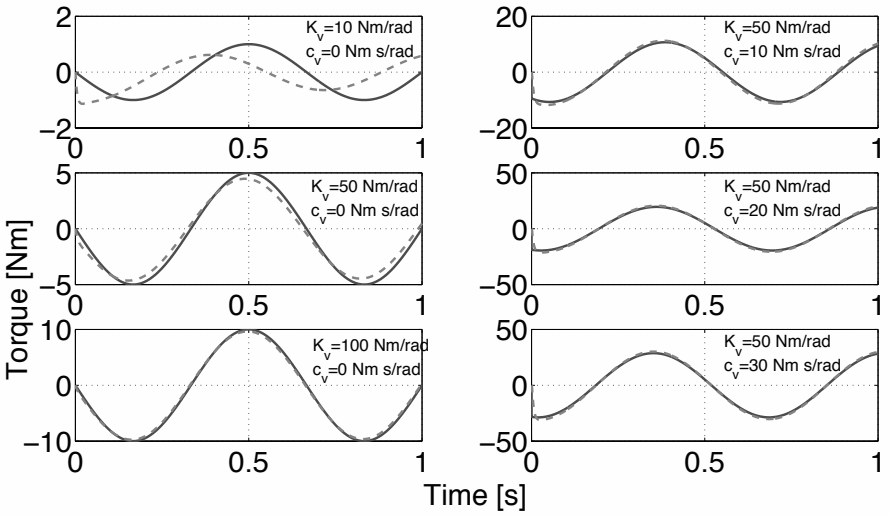

Figure 3.35: VIDA torque response to external position perturbations for different values of virtual impedance (ideal in solid blue, actual in dotted red). A sinusoidal rotation (amplitude 0.1 rad and frequency 1 Hz) was applied on the output.

s, a 5 N·m step torque, simulating the interaction with an external body, was applied on the output shaft. Results are reported in Fig. 3.37; virtual damping was c_v = 40 N·m·s/rad while virtual stiffness was 50 N·m/rad (top) and 20 N·m/rad (bottom).

3.4.5 Conclusions

The design of a Variable Impedance Differential Actuator has been presented: the model of the system is developed and the expected performances are evaluated through simulations in different conditions. It has been assessed that the VIDA is able to render the desired output impedance when the requested torque does not exceed the limits of the torque source (i.e. closed loop bandwidth and saturation). Impedance regulation degrades when a pure elastic behavior, with stiffness more than one order of magnitude smaller than the physical spring stiffness, is desired (Fig. 3.35). It has been verified that the desired impedance can be set while the output equilibrium position is being regulated by the PR (Fig. 3.36) also when an external torque disturbance is applied (Fig. 3.37). The presented actuation architecture allows to implement a control strategy where an equilibrium position

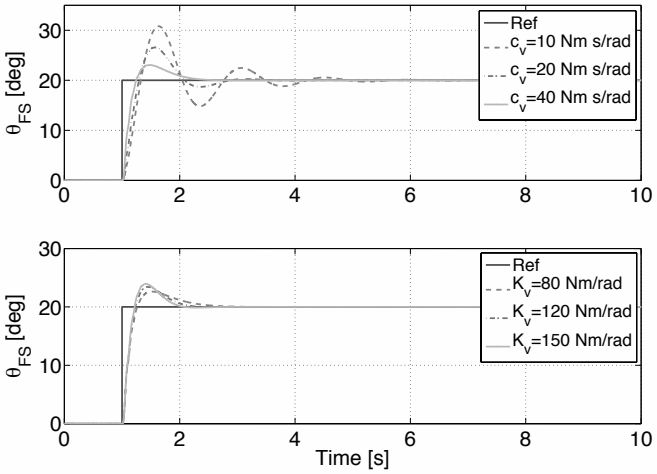

Figure 3.36: Response of the VIDA to a step reference position for different values of K_v and c_v. $K_v = 100$ N·m/rad (top) and $c_v = 40$ N·m·s/rad (bottom).

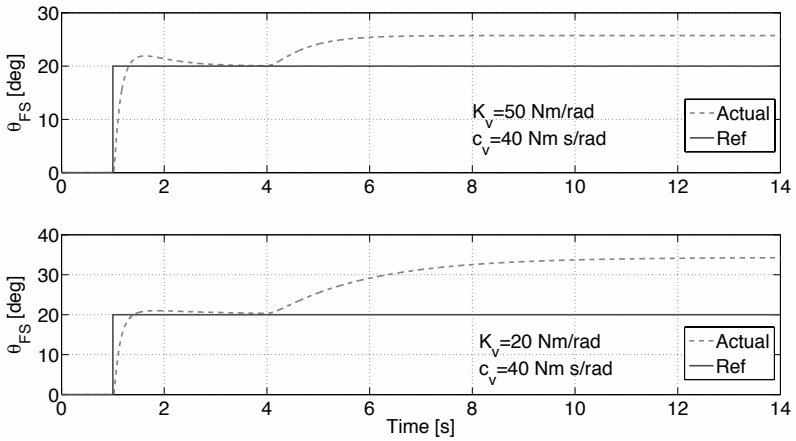

Figure 3.37: VIDA positioning task with torque disturbance; at $t = 4$ s, a 5 N·m step torque, simulating the interaction with an external body, is applied on the output shaft. Virtual damping is $c_v = 40$ N·m·s/rad; virtual stiffness is 50 N·m/rad (top) and 20 N·m/rad (bottom).

Nevio Luigi Tagliamonte

and impedance field are separately regulated. This is possible still adopting very simple control laws: two distinct Single-Input-Single-Output (SISO) controls for position and impedance regulation of the two input shafts.

Nevio Luigi Tagliamonte

Chapter 4

Design, control and characterization of a rotary Series Elastic Actuator

As pointed out in chapter 3 a number of advantages can derive from the serial connection of a compliant element to a gearmotor. Among the aforementioned ones, it worth recalling the possibility of operating in force (or torque) control mode in a way which is not so far from an ideal behavior (perfect force tracking and a null output impedance across the frequency spectrum). Indeed the use of series elasticity allows increasing the torque control loop gain (still maintaining desired stability margins) and to have a low output impedance, other than tolerance to shock loading, robustness to changing loads, reduction of internal stiction, friction and backlash [47]. Moreover, for external perturbations at frequencies above the actuator controllable bandwidth, the impedance of the system reduces to the stiffness of the spring thus avoiding unsafe behaviors due to possible sensors failure and/or control limitations.

The major drawback introduced by the series elastic element is the reduction of the actuator bandwidth with respect to a traditional stiff actuator. Improving the compliance of the actuator reduces the saturation frequency for a given torque, thus decreasing the overall performances of the system. In other terms, given some target torque control specifications, a SEA requires extra power source with respect

to a rigid motor. Therefore, when the system is stiffness-controlled, the maximum output stiffness that can be virtually rendered is limited by the elastic element, if conservative demands for passivity (as presented in chapter 2) are to be met [123].

Linear SEAs were originally employed in bipedal walking and running robots [124] where unavoidable high frequency disturbances due to impacts with the ground must be rejected. Despite of that, many rotary prototypes have been recently developed for several applications with very different performance requirements (see Figures 4.1-4.2). In [50] a compact SEA for a prosthetic elbow is presented (Fig. 4.1a) which is used to implement user-modulated impedance control. It is made of a customized frameless brushless motor and a HD gear; due to the hollow gearmotor the torsional spring is passed back through the center of the actuator (Fig. 4.2a). The prototype in [51] (Fig. 4.1b) is intended for a humanoid robot; it also uses a frameless brushless DC motor and a HD gear, but it employes a three spoke shaft with six linear springs (as reported in Fig. 4.2b) as compliant element. A similar architecture (frameless motor and HD) is also proposed in [56] (Fig. 4.1d) where a custom-made double spiral spring (Fig. 4.2b) is used, based on previous experience with hydraulic actuation [53]. This powerful SEA is intended to be used in a future version of the gait rehabilitation robot LOPES [52]. In the current SEA implementation of the LOPES platform, the actuation system of Fig. 4.1c is used: a brushless motor is located remotely with respect to the actuated joint and Bowden cables transmit the motion. Series elasticity is due to the agonistic/antagonistic arrangement of two linear compression springs (Fig. 4.2c) which are pre-tensioned with the maximally desired force to let cables always be under tension during operation. In [54] a SEA for an assistive active knee orthosis is designed (Fig. 4.1e). A very simple commercial torsion spring is inserted within the transmission mechanism (Fig. 4.2e). A worm gear is used to transmit the motion from one axis parallel to the longitudinal direction of the thigh to the knee joint axis; this solution allows distributing mechanical structure alongside the human segment for a compact design. The systems proposed in [55] (Fig. 4.1f), [57] (4.1g) and [58](Fig. 4.1h) use commercial DC motors. The first one includes a planetary gear and a compliant mechanism similar to the one of [51] with four linear springs (Fig. 4.2f); it was developed to validate velocity-sourced SEA control

approach (see sections 3.4.3.3 and 4.3). The second one, designed for a robotic manipulator, uses a planetary gear and a reduction capstan drive; compliance is introduced by means of a leaf spring mechanism (Fig. 4.2g) similar the one presented in section 3.1.2.2 for the VSJ system [81]. The third one is employed in an exoskeleton for the upper limbs; it comprises a simple commercial torsion spring (Fig. 4.2h). In [59] a nonlinear SEA is presented for running and jumping robots (Fig. 4.1i). The actuator uses a hypocycloid mechanism to stretch a linear spring in a nonlinear way (Fig. 4.2g) which can be adjusted offline through a pretensioning mechanism.

It is worth recalling a particular implementation of SEA which is named DEA used in a legged tracked wheeled robot [64]. In this system a HD in differential mode is used with a frameless motor connected to the WG and a commercial elastic joint connected to the CS. This arrangement allows a serial coupling of the elements attached to WG and CS shafts (as already mentioned in chapter 3).

In this chapter a compact SEA for assistive wearable robots id presented. The system has a modular design to easily change some components (i.e. motor, reduction gear and spring) for different possible configurations and/or performances. In particular, the presented implementation is compatible with requirements of a knee assistive robot for elderly subjects with an age-related decay of motor performances. Design will be described and torque/impedance control implementation together with experimental characterization will be extensively reported. At the end of the chapter a new design and some preliminary tests will be briefly introduced.

4.1 Design requirements

As aforementioned, different performances can be achieved with the proposed design. The target for the configuration presented here is knee assistance.

A number of gait features are influenced by aging, such as decreased gait velocity (caused by a greater time spent in double support and decreased step length) [125] and increased stance time [126]. Elderly people have generally a more conservative gait pattern than healthy young subjects, consisting of a lower preferred walking speed [127] and shorter steps [128]. Considering data set described in [129], the maximum instantaneous power exerted by the knee joint during slow walking is

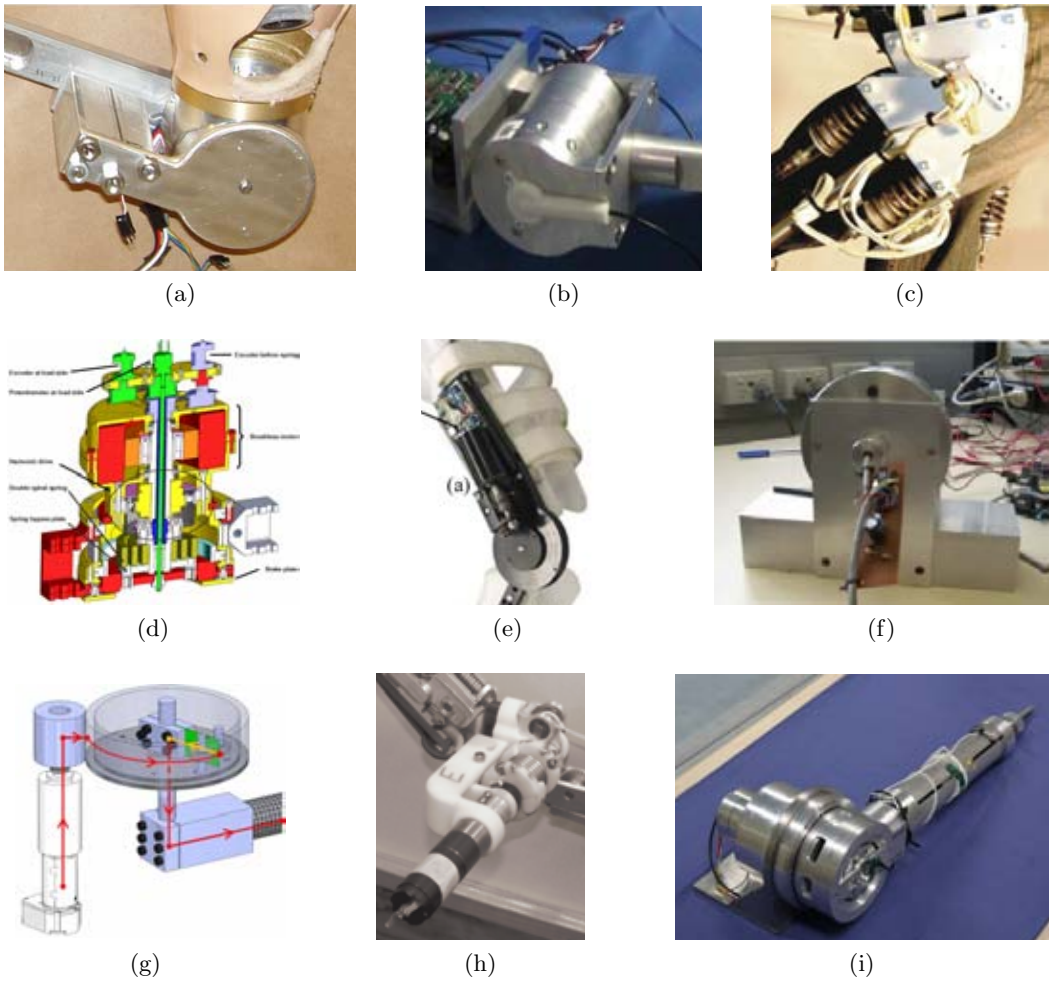

Figure 4.1: Rotary SEA prototypes: [50] (a); [51] (b); [52] (c); [56] (d); [54], (e); [55] (f); [57] (g); [58] (h); [59] (i).

Nevio Luigi Tagliamonte

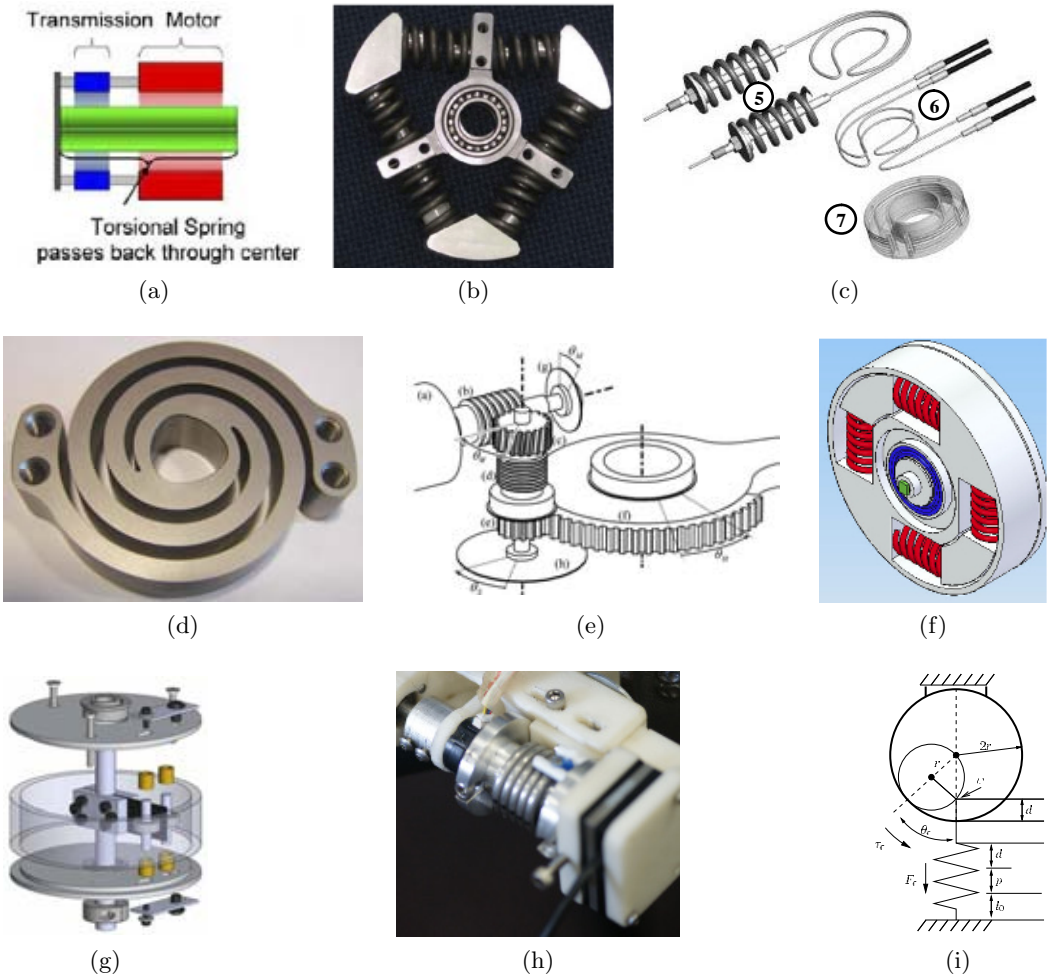

(a) (b) (c)

(d) (e) (f)

(g) (h) (i)

Figure 4.2: Elastic elements of the prototypes reported in Fig. 4.1: [50] (a); [51] (b); [52] (c); [56] (d); [54], (e); [55] (f); [57] (g); [58] (h); [59] (i).

about 40 W with a maximum torque of 29 N·m and an RMS value equal to 20 N·m. If 30% of the peak torque required during overground walking is willed to be provided by the actuator, a target of 10 N·m has to be selected as design requirement. The reduction in the duration of the swing phase also imposes that torque regulation needs to be fast enough to impart rapidly changing assistance levels during walking. To this aim, considering 90% of the power spectral density of knee torque profile from [129], a minimum bandwidth of 4 Hz is demanded for the torque control.

The stiffness of the series elastic element needs to be carefully selected in order to trade-off between performances, intrinsic transparency and safety. The compliant element is required to be verified against the maximum output torque supplied by the actuator and to provide a linear torque-deflection relationship both in static and dynamic conditions. Moreover, it should be directly connected to the load, so to avoid the effect of torque tracking fidelity reduction caused by transmissions non-linearities. Physical stiffness values of SEAs for locomotion assistance, as retrieved from a literature analysis may range from 100 to 300 N·m·rad^{-1} [130, 131, 56, 53]. Considering this assumption, in the present work, a stiffness value of 150 N·m·rad^{-1} was taken as specification for the actuator series elasticity (in section 4.2.1 more details about this choice will provided). Actuator dimensions and mass have to be reduced as much as possible; as design requirements a maximum weight 2 kg and a maximum encumbrance of 150 × 150 × 200 mm^3 were considered to limit bulkiness and avoid hindering human natural motion.

4.2 Prototype components

A 90 W brushless DC motor (Maxon EC90-flat) with a weight of 648 g, and a maximum continuous torque of 494 mN·m was selected. It is equipped with Hall sensors for current commutation and with a 500 cpt optical incremental encoder Avago HEDL5540 to measure motor rotation with a resolution of 0.18 deg (quadrature reading). A HD gear has been employed for its compactness, low weight, high positioning accuracy and high efficiency. The selected gearing is the CSD-20-50-2A-GR, with a reduction ratio of 50:1, a weight of 130 g, a thickness of 14 mm and a diameter of 70 mm. The CS is fixed to the frame, the WG is connected to the flat motor

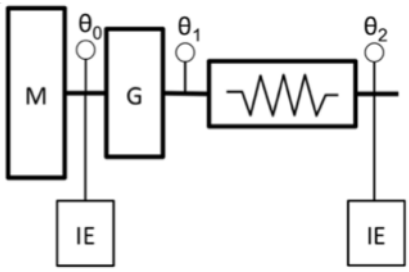

Figure 4.3: SEA sensorization: the motor (M) shaft rotation (θ_0) and the system output shaft rotation (θ_2) are measured using incremental encoders (IE) while the gear (G) output shaft rotation (θ_1) is not measured.

shaft while the FS is connected to the serial spring. This motor-gear combination guarantees a nominal speed of about 4 rad/s and a maximum continuous torque of about 20 N·m (twice the target value).

As mentioned in the previous section different arrangements can be achieved with small modifications: fixed the geometrical dimensions two Maxon motors with different electrical characteristics and three possible reduction ratio (50:1, 100:1 and 160:1) for the HD gear are available. The interchange of these components (6 possible configurations) does not cause any modification in the design. If some connection pieces are substituted also serial and parallel connections of two springs can be made, thus increasing to 18 the number of theoretically devisable configurations.

An ASM magnetic incremental encoder, composed by a PMIS4 reading sensor head and a PMIR4 magnetic code wheel, measures the actuator output rotation and, considering differential reading with respect to motor encoder, allowed estimating spring deflection. Actuator output measurement has a resolution of 32768 counts per turn ($3{\cdot}10^{-3}$ deg when using quadrature reading). In Fig. 4.3 the topological distribution of the sensors is reported: the motor (M) shaft rotation (θ_0) and the system output shaft rotation (θ_2) are measured using incremental encoders (IE) while the gear (G) output shaft rotation (θ_1) is not measured.

Fig. 4.5 depicts a cross section drawing of the proposed system while Fig. 4.4 shows a picture of the prototype. The overall dimensions are: 120 mm (diameter) × 165 mm (axial length) and the overall actuator mass is 1.8 kg.

Nevio Luigi Tagliamonte

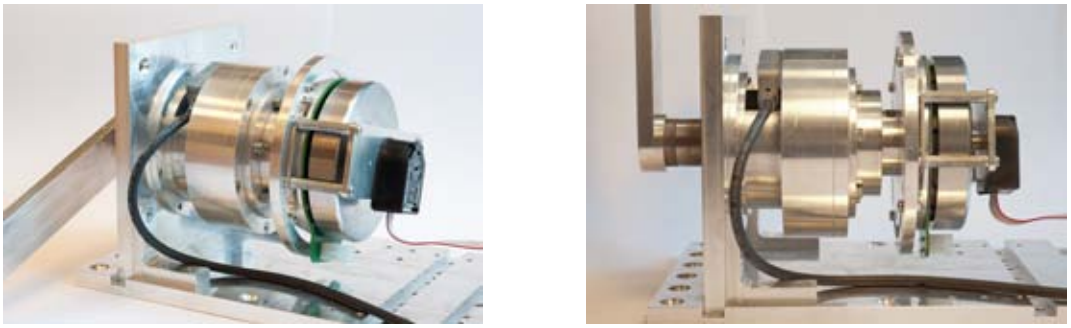

Figure 4.4: Picture of the assembled SEA prototype: the frame is fixed to an aluminum support, while the actuator output shaft is connected to a rectangular link.

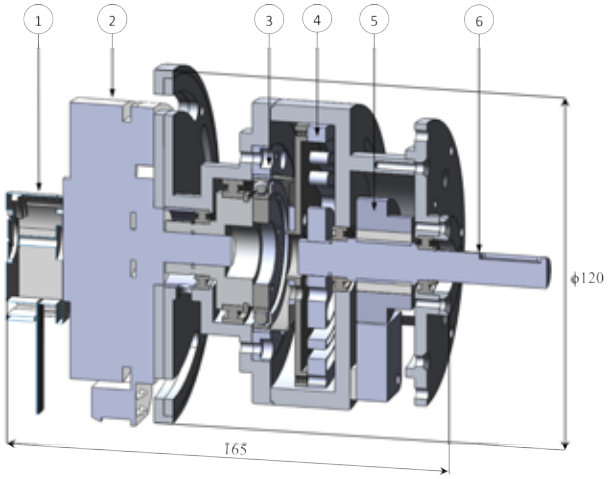

Figure 4.5: Cross section of the rotary SEA. 1: optical incremental encoder, 2: flat DC motor, 3: Harmonic Drive, 4: torsion spring, 5: magnetic incremental encoder, 6: output shaft. Dimensions: 120 mm (diameter) × 165 mm (axial length). Total mass: 1.8 kg.

Nevio Luigi Tagliamonte

4.2.1 Custom torsion spring

A stiffness of 150 N·m·rad^{-1} was considered as target value for the design of the torsion spring, as described in section 4.1. This value is in the range of data retrieved from a literature analysis on SEAs for gait assistance [130, 131, 56, 53]. Spring stiffness choice generally emerges as a trade-off between the need for intrinsic low impedance and torque control expected performances. Indeed, as already pointed out, due to motor velocity saturation high compliance causes a reduction of deliverable torque at a given frequency. The selected value is in the same order of magnitude of human knee stiffness [132] thus the system is not intrinsically perceived as to stiff from a human subject. At the same time 4-5 Hz bandwidth for 10 N·m delivered torque can be assured with velocity values which are within saturation limits of the selected gearmotor [47]. Elastic element properties also have an impact on the torque measurement quantization once fixed the resolution of selected rotation sensors. In the presented prototype a theoretical resolution of about 1 mN·m is selected. As mentioned above, SEA torque regulation can be achieved, for example, by employing position/velocity control of the motor. In order to avoid the use of complex non-linear control schemes and to allow homogeneous regulation capability above the whole range of deliverable torques, a linear torque-angle characteristic is desirable. Indeed, non-linear relationships would imply an increased sensitivity to motor control inaccuracies thus possibly implying high torques regulation errors.

The main challenge in the design of compliant elements for SEAs is the achievement of low stiffness while guaranteeing resistance to high torques (e.g. in the order of 10-50 N·m for typical applications in assistive robotics). Commercial compact solutions are often not able to simultaneously fulfill these requirements: simple beam flexures can be verified against high torques but they are excessively stiff; helical torsional springs provide low stiffness but they do not withstand torques required for human assistance purposes.

For this reason a custom monolithic disc-shaped design has been pursued, which also minimizes weight and dimensions, reducing the bulk in the radial direction and maintaining an acceptable thickness. This shape implies torque transfer to occur between an outer ring (diameter: 85 mm) and an inner ring (diameter: 12 mm).

Compliance is due to the interposition of flexible lamellae between the two rings which act as curved thin beams mainly undergoing pure bending load. The shape and dimensions of such flexible elements were designed through an iterative Finite Element Method (FEM) simulations-based design and optimization process.

In particular, different topological solutions were considered and morphological properties were optimized for each of them. The values of the *specific elastic energy* of the best solutions were compared to chose the optimized spring. The selected topology includes three replications (120 deg shifted with respect to the disc center) of two couples of arched lamellae. Fig. 4.6 depicts a general spring morphology based on this topology highlighting fixed and variable parameters. Letter are used for the optimized parameters while number indicate pre-defined dimensions in mm. Disc thickness is a design constraint and is set to 3 mm.

Figure 4.6: Drawing of a general spring morphology based on the selected topology with fixed and variable parameters. Letter are used for open parameters while number indicate fixed dimensions in mm. Disc thickness is a design constraint and is set to 3 mm. Radii of arches joining two different lamellae are not reported since are not independent variables.

Nevio Luigi Tagliamonte

Table 4.1: Morphological parameters of the optimized spring. α is in deg; all the other dimensions are in mm.

Parameters	Values
R_1	23
R_2	27
R_3	29.5
R_4	33
s_1	0.6
s_2	0.5
s_3	0.6
s_4	0.5
w_1	5
w_2	3
w_3	4
p_1	0.6
p_2	0.6
D_1	32
D_2	75
α	116

The morphological parameters of the best solution are reported in Table 4.1 while a picture of the prototype is shown in Fig. 4.7. According to FEM result this spring has stiffness of 153 $\mathrm{N \cdot m \cdot rad^{-1}}$ and it is verified for a torque of 10 $\mathrm{N \cdot m}$ with a safety factor of 1.4.

The spring was manufactured by Wired Electrical Discharge Machining (WEDM) of VACO 180T steel and it was subjected to an aging treatment of 4 hours at 482 °C, to guarantee the nominal yield stress value. Total dimensions of the compliant disc are 85 mm for the outer diameter and 6 mm for the thickness. The inner ring is connected to the FS of the WG while the outer ring is fixed to the SEA output shaft.

4.3 SEA control

4.3.1 Control hardware

The control hardware includes the following components:

Figure 4.7: Picture of the custom torsional spring. Dimensions: 85 mm external diameter, 12 mm internal ring diameter and 6 mm axial length. A shaped shaft-hub coupling is used as connection between the spring internal ring and the output shaft.

- Maxon EPOS2 50/5 control unit to drive the brushless DC motor, capable of providing up to 50 V constant voltage and 5 A continuous current (peak of 10 A for less than 1 s). It comprises interfaces with motor windings, Hall sensors and motor optical encoder.

- National Instruments (NI) CompactRIO-9022 embedded control and acquisition system, which includes a reconfigurable Field-Programmable Gate Array (FPGA) module and an embedded controller running LabVIEW Real Time (RT) (533 MHz processor, 2 GB non-volatile storage, 256 MB DDR2 memory). The device also includes a NI 9401 digital I/O module to acquire the quadrature signals from the output incremental encoder, and a NI 9853 high speed CAN module for communication with the EPOS2 control unit.

The control is hierarchically structured (from low to high level) as follows:

1. FPGA level: programmed (using LabVIEW FPGA software) to acquire SEA output encoder quadrature signals and to execute CAN bus low level com-

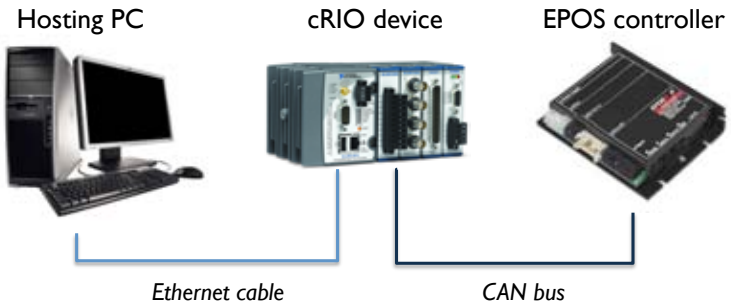

Figure 4.8: Connection of control hardware components for the SEA control.

munication with the EPOS2 controller (transmission of motor commands and reading of current, position and velocity motor data);

2. RT level: programmed (using LabVIEW RT software) to run torque and impedance controls; , programmed through LabVIEW RT software;

3. Host PC level: used to to write and deploy LabVIEW FPGA and RT code on the CompactRIO and as graphical interface to visualize transmitted and elaborated data.

Interconnection among the components of the control system are reported in Fig. 4.8

4.3.2 Control architecture

SEA torque regulation is performed by measuring the deflection of the elastic element, i.e. the difference between the SEA output angle θ_{out} and the gearmotor rotation θ_m. Said K_s spring stiffness and considering that the torque-deformation characteristic relation of the elastic element is well fitted by a linear relation, the torque delivered by the actuator can be estimated as $\tau = K_s(\theta_m - \theta_{out})$.

Different approaches to SEA torque control have been proposed, mainly classifiable depending on which physical variable is directly commanded to the actuator at the lowest level: current control and position/velocity control. Historically, first approaches involved directly controlling motor torque by regulating the current [48, 49].

In next studies it was proposed to substitute the low level current loop with a velocity loop nested in the external torque control loop, thus considering the motor as an ideal flow generator (*velocity-sourced SEA*) [55]. This approach allows to increase performances in terms of torque fidelity and to render a higher range of output impedance values, [123]. Moreover, comparison between inner velocity and position control loops are reported in [133] demonstrating that performances depend on the type and position of the employed sensors.

The control scheme used in the present work follows the approach proposed by [55] and [123] and similar to the one employed in the simulation study of section 3.4.3.3. A block diagram describing SEA torque control is reported in Fig. 4.9. The desired velocity command generated by the torque and impedance controllers, implemented on the CompactRIO, is transmitted to the velocity controller, implemented on the EPOS2 device, through the CAN bus (CANopen protocol). Both control loops run at 1 kHz.

The measured spring deflection signal is filtered through a second order lowpass Butterworth filter with a cut-off frequency of 40 Hz and torque is estimated taking into account a deadband of the torque-deflection characteristic due to backlash (see section 4.4.1). The computed torque is then fed back to the torque controller, closing the torque control loop.

The presented hardware architecture allows decentralizing computation, since motor winding current commutation (based on Hall sensors measurements) as well as velocity control (based on motor encoder measurement) are managed remotely with respect to the central control unit by the EPOS2 device. Low level acquisition/conditioning of encoder data and higher level torque/impedance control are managed by CompactRIO central unit.

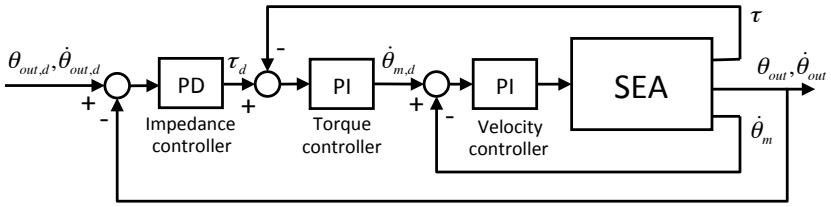

Figure 4.9: SEA torque control scheme. The delivered torque is measured as $\tau = K_s(\theta_m - \theta_{out})$, being θ_{out} the SEA output angle and θ_m the gear motor rotation. $\dot{\theta}_{m,d}$ is the desired motor velocity as generated by the torque controller.

4.4 Experimental characterization

4.4.1 Spring stiffness measurement

Experimental characterization of the designed spring was performed mounting it in the SEA assembly and connecting the output shaft to a torque sensor[1] (Lorenz Messtechnik GmbH DR-2, nominal measurable torque 50 N·m) fixed to the test-bed frame. To avoid spurious forces deriving from radial misalignments between SEA and sensor shafts, a flexible coupling (Rodoflex ATMK60L77, nominal torque 60 N·m) was interposed between them. With this arrangement the external ring of the spring could not move and the internal one was rotated by the motor while the applied torque was recorded by means of the torsiometer.

The SEA was commanded to track a position profile consisting in a sequence of steps (amplitude 0.2 deg, duration 2 s), including both loading/unloading directions and positive/negative rotations. A linear regression was performed between imposed rotations and measured torque values. The result is shown in shown in Fig. 4.11.

Two one-coefficient linear regressions, for positive and negative spring deflections were performed, imposing crossing of the origin. The two regression coefficients differed in less than 0.5% thus making reasonable to calculate a global stiffness value as their average, which turned out to be 119 $\mathrm{N} \cdot \mathrm{m} \cdot \mathrm{rad}^{-1}$. Backwards regression was then implemented on the so-determined profile (measured stiffness of 119 N ·

[1] Analog signal was acquired through the CompactRIO central unit device using a NI 9205 analog input module.

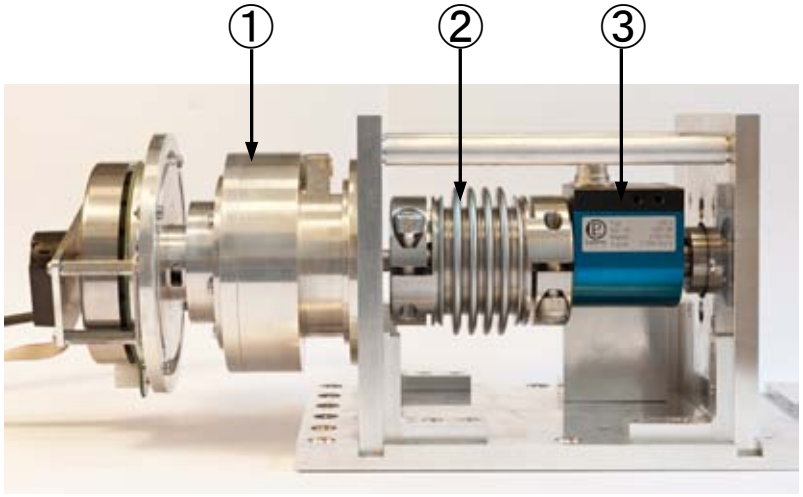

Figure 4.10: Test-bed used for spring characterization. 1: SEA, 2: flexible coupling, 3: torque sensor.

$\mathrm{m} \cdot \mathrm{rad}^{-1}$), giving R^2 coefficients higher than 0.99 for both positive and negative deflections.

The value of K_s determined experimentally is 22% lower than the one predicted by FEM simulations. Similar discrepancy (29%) was previously reported by other researchers using different FEM methods and different geometries [56] but similar material thus suggesting that maraging steel could have actual elastic properties quite different from the nominal ones, probably very sensitive to fabrication and aging treatment. Nevertheless, this discrepancy cannot be inputed to the compliance of the characterization setup: based on components datasheets, it could be determined that the equivalent undesired stiffness between the motor and the spring was around 20 times higher than the one to be measured (HD flexible spline stiffness: $1.1 \cdot 10^4$ N·m·rad^{-1} in the range of 0-7 N·m and $1.3 \cdot 10^4$ N·m/rad in the range of 7-25 N·m; torque sensor stiffness: $4,82 \cdot 10^3$ N·m·rad^{-1}; flexible coupling stiffness: $42 \cdot 10^3$ N·m·rad^{-1}).

The presence of a non-negligible backlash shown in 4.11 (amplitude 1 deg) was determined by fabrication inaccuracies in the shaped shaft-hub coupling of the elastic element. Despite of that a high linearity and low hysteresis were achieved.

Nevio Luigi Tagliamonte

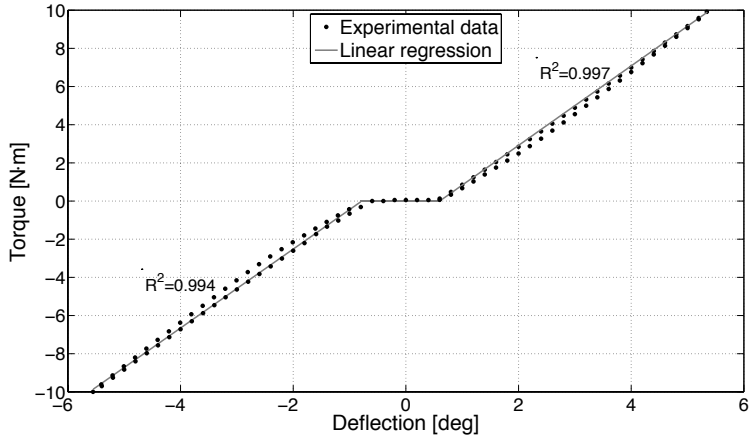

Figure 4.11: Experimental torque-angle characteristic of the torsion spring. Loading and unloading phases are reported, both for positive and negative deflection. R^2 coefficients refer to the fitting of both positive and negative torque-deflection curves to the global stiffness curve, reported in solid line.

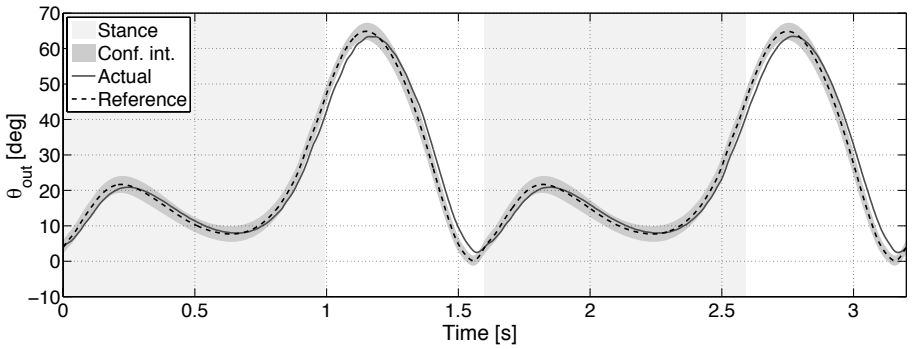

Figure 4.12: SEA position tracking for a typical knee profile during overground walking (gait cycle duration: 1.6 s), with superimposed confidence intervals ($p < 0.05$). RMS error is 2.7 deg.

4.4.2 Position control

As a preliminary validation of the described design, the actuator was position-controlled to track a representative knee angle profile during locomotion, as retrieved from the slow walking dataset in [129], for a gait cycle duration of 1.6 s, with the actuator output unloaded. Fig. 4.12 shows a position regulation performance in the described conditions, where an RMS error of 2.7 deg is obtained.

Nevio Luigi Tagliamonte

4.4.3 Torque control

Torque control performances of the developed SEA were characterized using the method proposed in [47], which involves the connection of the actuator output shaft to the ground frame (*locked output* conditions). In this configuration different metrics were considered to measure the performances of the torque controller, as described in the following sections.

4.4.3.1 Step response

PI torque controller gains were regulated based on the system response to a step commanded torque, in order to have an overshoot lower than 5% and a rise time (to span from 5% to 95% of the setpoint) lower than 10 ms. Fig. 4.13 shows the response of the system to commanded steps with different amplitudes: 3 and 10 N·m. The system responds with a 4% overshoot and with a maximum rise time of 6 ms, for the largest commanded input. Actuator non-linearities (motor velocity saturation) in the response to the largest input imply a 2 ms lag between the rise time calculated at 3 and 10 N·m.

Torque measurement has a theoretical quantization, introduced by the resolution of the encoders, of 5 mN·m (considering 119 N). However, the step responses measured in the real system had a higher maximum regime error, of 100 mN·m. This was caused by motor positioning inaccuracy introduced by velocity control, and by the backlash of the set-up. Nevertheless, this torque control resolution is considered adequate for applications involving human assistance [53].

4.4.3.2 Torque tracking fidelity

Preliminary experiments to assess torque control fidelity were carried out in *locked output* conditions, setting as desired torque for the actuator a sinusoidal signal and a chirp (sine sweep) stimulation, i.e. a sine signal with frequency linearly varying with time:

$$u(t) = A\sin[(at + b)t] \tag{4.1}$$

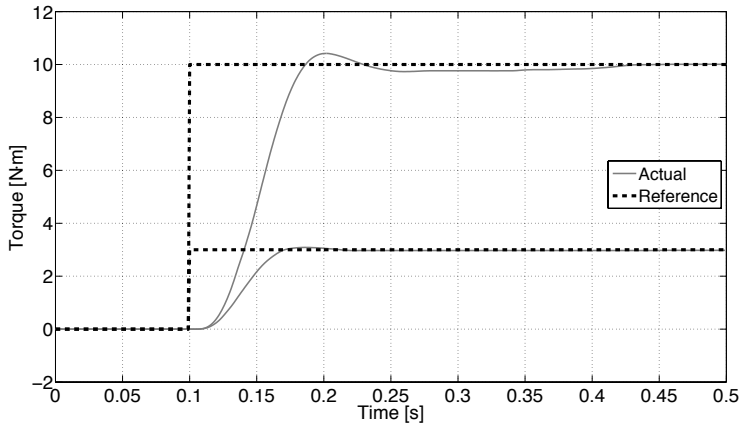

Figure 4.13: Response of the SEA to torque step commands (amplitude 3 N·m and 10 N·m, with locked actuator output.

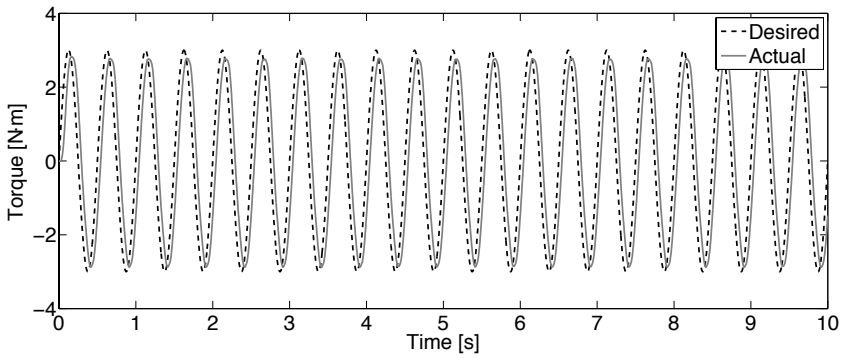

Figure 4.14: Steady-state response of the SEA to a torque reference sinusoid with amplitude 3 N·m (RMS: 2.12 N·m) and frequency 2 Hz.

with a and b constant values to be chosen depending on the desired frequency content in a given period.

Fig. 4.14 reports a representative test with the SEA commanded to track a sinusoidal desired torque with amplitude 3 N·m and frequency 2 Hz. In Fig. 4.15 a representative test with a chirp signal is reported: the commanded torque has 3 N·m amplitude and frequency wich spans from 0 to 3 Hz in 30 s.

It is worth noticing that deviations from the ideal tracking when crossing zero torque are due to backlash; these deviations are kept very small (even though 1 deg

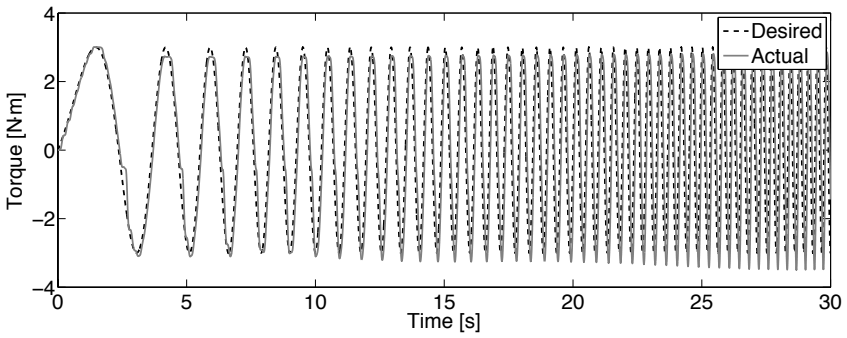

Figure 4.15: SEA response to a sine sweep desired torque with amplitude 3 N·m and frequency spanning from 0 to 3 Hz in 30 s.

backlash causes a theoretical dead zone of about 2 N·m) thanks to the deadband filtering of the encoder reading introduced in section 4.4.1.

4.4.3.3 Torque control bandwidth

Torque control bandwidth is defined as the transfer function between the desired torque τ_d and the actual torque τ delivered by the actuator, when the output is fixed [47]. In the frequency domain, it can be written as:

$$G_{tor}(f) = \frac{T(f)}{T_d(f)} \tag{4.2}$$

being $T(f)$ and $T_d(f)$ the Fourier transforms of τ and τ_d respectively.

To experimentally determine the transfer function $G_{tor}(f)$, the SEA was stimulated setting as desired torque τ_d a Schroeder multisine waveform [134]. This signal is a sum of N harmonically related sine waves:

$$u(t) = \sum_{k=1}^{N} A\cos(2\pi f_k t + \phi_k) \tag{4.3}$$

with phases $\phi_k = -k(k-1)\pi/N$ and frequencies $f_k = kf_0$, being f_0 the frequency resolution and $1/f_0$ the period of the signal (inverse of its duration). This multisine signal has been selected because of its flat spectrum in the excitation bandwidth and its low crest factor (defined as $|u_{max}|/u_{RMS}$).

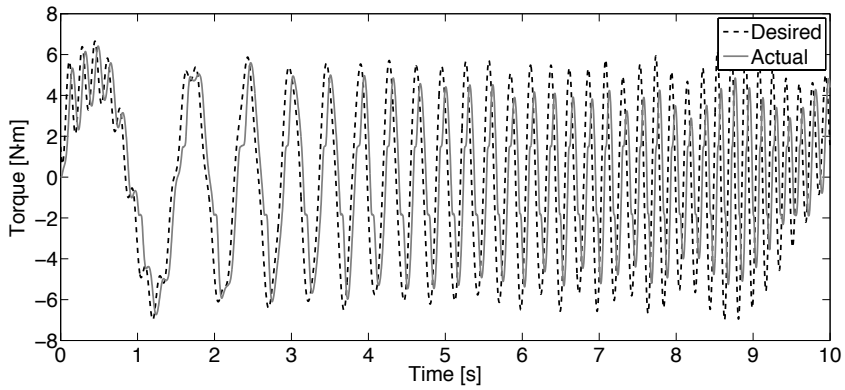

Figure 4.16: SEA response to a Shroeder multisine desired torque with a peak value of 7 N·m (RMS: 3.82 N·m) and frequency content of 0.1-6 Hz.

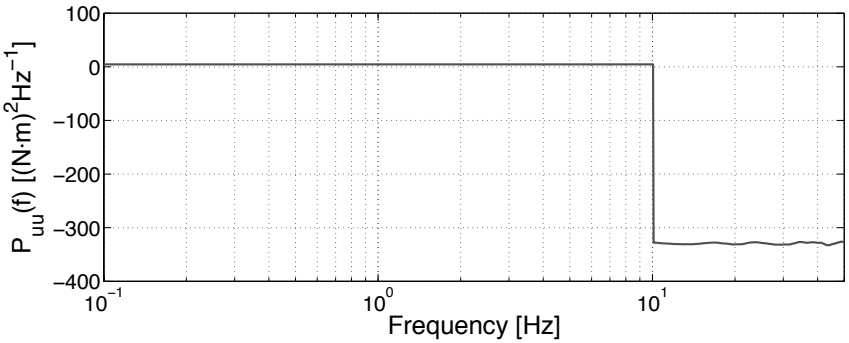

Figure 4.17: Power spectral density of the multisine signal used for characterization of maximum torque control performances. Power content is mostly comprised in the range 0.1-10 Hz with a flat spectrum.

In Fig. 4.16 a representative test is reported: the SEA is commanded to track a Shroeder multisine desired torque with a peak value of 7 N·m (corresponding to a RMS value of 3.82 N·m) and frequency content of 0.1-6 Hz.

For the experimental characterization of maximum performances the signal fed to the torque controller had f_0=0.1 Hz, N=100, and amplitude scaled to generate a peak torque of 10 N·m (corresponding to a RMS value of 5.45 N·m). This signal has a flat power spectral density between 0.1 and 10 Hz, and negligible power content above 10 Hz, as shown in Fig 4.19.

Being u and y input and output signal respectively, the related transfer function

can be estimated using non parametric system identification method [134] as follows:

$$\hat{G}(f) = \frac{P_{uy}(f)}{P_{uu}(f)} \tag{4.4}$$

with $P_{uy}(f)$ the cross-spectral density of the input and the output and $P_{uu}(f)$ the auto-spectral density of the input. To assess reliability of the estimation, the squared coherence function can be calculated as a measure (from 0 to 1) of the correlation between the input and output at each frequency:

$$Coh(f) = \frac{|P_{uy}(f)|^2}{P_{yy}(f)P_{uu}(f)} \tag{4.5}$$

in which P_{yy} is the auto-spectral density of the output.

Following this method the torque control transfer function $G_{tor}(f)$ can be estimated as:

$$\hat{G}_{tor}(f) = \frac{P_{\tau_d\tau}(f)}{P_{\tau_d\tau_d}(f)} \tag{4.6}$$

Figure 4.18 shows the performances of the implemented controller, demonstrating a maximum bandwidth (defined as the frequency at which signal amplitude is attenuated by 3 dB) of 5.3 Hz for a multisine reference signal with peak amplitude 10 N·m and frequency content 0.1-10 Hz.

This result can be considered reliable because of the high coherence value in the tested frequency range (higher than 0.9 up to 9 Hz) as shown in Fig. 4.19.

4.4.4 Impedance control

Characterization of impedance control was performed by manually perturbing the actuator output shaft through oscillatory movements manually imposed grasping the output link shown in Fig. 4.4. Said θ_{out} the position perturbation and τ the actuator torque response, mechanical impedance is defined in the frequency domain as:

$$Z(f) = \frac{T(f)}{\Theta_{out}(f)} \tag{4.7}$$

Impedance control was implemented by imposing position- and velocity-dependent torque fields around the desired kinematic status ($\theta_{out,d}$, $\dot{\theta}_{out,d}$) as follows:

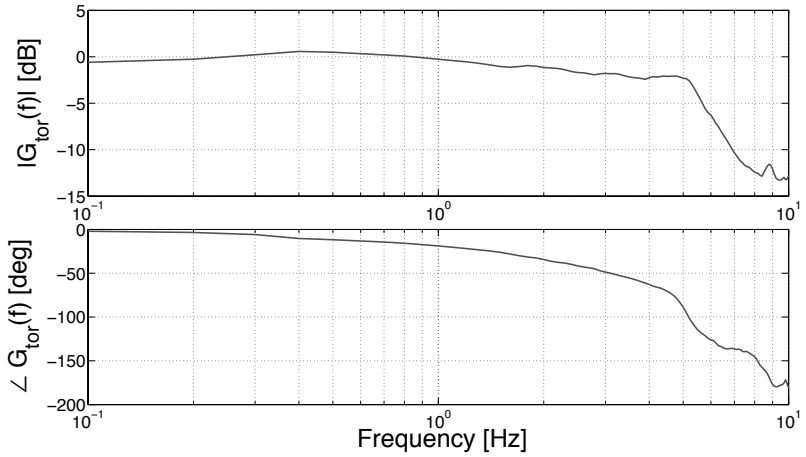

Figure 4.18: Bode diagram of torque control transfer function $\hat{G}_{tor}(f)$. Desired signal is a Schroeder multisine, peak amplitude 10 N·m (RMS value: 5.45 N·m). Torque control bandwidth, defined as the frequency at which signal amplitude is attenuated by 3 dB, is 5.3 Hz. At this frequency, the phase lag is 106 deg.

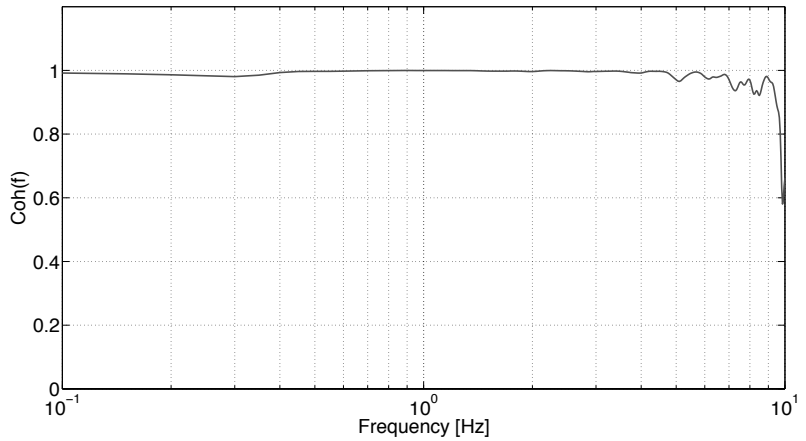

Figure 4.19: Squared coherence function related to the transfer function of Fig. 4.18. The high coherence value in the stimulated frequency range attests reliability for the maximum torque control performance test.

$$\tau(t_d) = -K_v[\theta_{out}(t) - \theta_{out,d}] - c_v[\dot{\theta}_{out}(t) - \dot{\theta}_{out,d}] \tag{4.8}$$

where K_v and c_v are the desired virtual stiffness and damping coefficients. Characterization of the performances of impedance control was performed first tackling the problem of rendering a pure stiffness K_v, and then rendering a desired damping c_v. Impedance transfer function was estimated using (4.4), i.e. considering θ_{out} as input signal and τ as output signal.

4.4.4.1 Stiffness control

In order to assess stiffness regulation performances, different tests were carried out, considering the control law expressed in (4.8), by setting $\theta_{out,d} = \dot{\theta}_{out,d} = 0$, $c_v = 0$, and varying K_v in the range $[0.25\,K_s,\ K_s]$, with increases of $0.25\,K_s$ (29.75 N·m·rad^{-1}).

In Fig. 4.20 transfer function estimation for the impedance in the case of stiffness control is reported. It can be seen that impedance regulation performances increase with the value of K_v[2]. Defining stiffness control bandwidth as the frequency where $\left|\frac{|Z(f)|-K_v}{K_v}\right| \geq 0.5$, a minimum bandwidth of around 1.5 Hz is obtained for $K_v = 0.25\,K_s$, while theoretically infinite bandwidth is obtained when $K_v = K_s$ (the impedance of the system reduces to the stiffness of the physical spring and the motor is quite idle). At frequencies lower than the stiffness control bandwidth, the actuator actually behaves as a pure spring, with phase lag of -180 deg.

Above the stiffness control bandwidth, attenuation of torque control is responsible for increased stiffness magnitude and for the reduction in phase lag, thus introducing damping behavior in the response. At higher frequencies, where the action of actuator control can be neglected, all curves converge again to a pure elastic behavior, with phase lag of -180 deg and virtual stiffness magnitude close to the stiffness of the physical spring K_s.

[2]Performances degradation in rendering a pure elastic behavior with stiffness much lower than the one of the physical spring was already experienced in the simulation study on the VIDA system (see section 3.4.4.2) and it is in line with literature results [53].

Nevio Luigi Tagliamonte

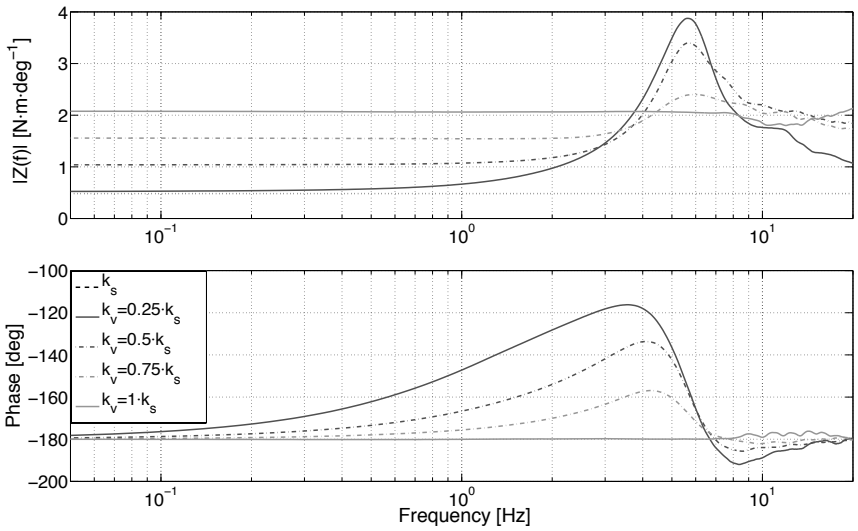

Figure 4.20: Bode diagram of estimated impedance, when rendering a pure elastic behavior with different virtual elastic constants K_v, defined as a fraction of the physical spring stiffness constant K_v of the SEA.

4.4.4.2 Damping control

A similar procedure was pursued to assess damping regulation performances, imposing the control law expressed in (4.8), by setting $\theta_{out,d} = \dot{\theta}_{out,d} = 0$, $K_v = 0$ and varying c_v in the range [0, 0.4] N·m·s·deg^{-1}, with increments of 0.1 N·m·s·deg^{-1}. The frequency content of the applied perturbation was negligible for frequencies above 2 Hz (manually applied position perturbations). The response of the system in the excited frequency range was estimated using (4.4). Moreover, for the sake of a more intuitive representation, the transfer function:

$$Y(f) = \frac{T(f)}{\Omega_{out}(f)} \tag{4.9}$$

was calculated and reported in Fig. 4.21 (instead of expression (4.7)), being $\Omega_{out}(f)$ the Fourier transform of the output velocity $\dot{\theta}_{out}(t)$.

The desired damping behavior is obtained at frequencies below 1 Hz, with a frequency-independent ratio between torque and velocity and a 180 deg phase lag. However, the damping value estimated by system identification is higher than the desired is reported in Fig. 4.21. The difference between estimated and expected

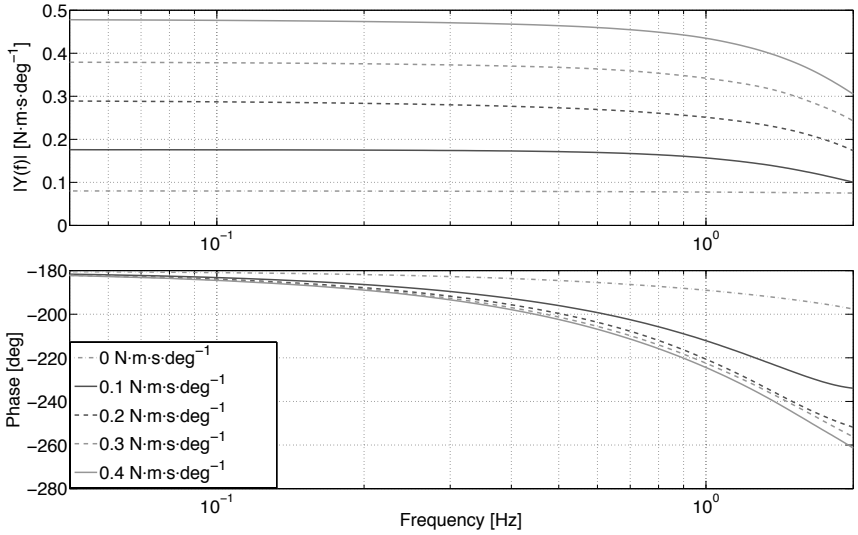

Figure 4.21: Bode diagram of the estimated transfer function $Y(f)$, when rendering a pure viscous behavior with different damping constants c_v.

damping at low frequencies is equal to 0.075 ± 0.002 N·m·s·deg^{-1}. This value is caused by the *parasitic* damping of the motor, as assessed in experiments where the actuator was commanded to track a null reference torque, thus demonstrating that intrinsic friction in the system is not completely compensated by the control. However, this residual damping is more than two orders of magnitude lower than that of human knee [132] and it can be assumed that it does not introduce significant drawbacks for the application selected for the presented SEA.

4.5 Conclusions

A compact rotary SEA for gait assistance applications was presented and its performances, being torque and impedance control implemented, were characterized. The chosen application field poses significant challenges to the design of an actuator, since it requires high performances in terms of both amplitude and bandwidth of torque regulation, still maintaining limited mass and inertia to minimally perturb the wearer's natural movements. SEA architecture introduces an important advantage in wearable robotics, since it provides intrinsic compliance in the transfer

of mechanical energy between actuation system and human limbs, even though it causes a degradation of torque regulation capabilities at high frequencies.

The presented system is a particular implementation of a more general modular architecture, and it fulfill a set of requirements for a knee assistive device defined on the basis of gait analysis data of elderly target users. A major novelty element of the proposed system is the compliant element, which was purposively optimized and fabricated, since no commercial component would have assured such a compact and lightweight design and respect of both low stiffness/high torque requirements. The manufactured spring has significantly lower stiffness than the simulated one, probably due to discrepancy between the elastic properties of the actual material and the nominal values used in the FEM simulations (it is worth recalling that similar results were also previously found in [53, 56]). Fabrication inaccuracies expectedly contributed to such discrepancy, given the torsional stiffness the sensitivity to the thickness of the lamellae.

A velocity-source type torque control scheme was implemented to regulate a maximum torque of 10 N·m with a bandwidth of 5 Hz. These performances were evaluated experimentally using non parametric system identification techniques. Impedance control was also implemented and response to externally applied perturbations were experimentally measured, demonstrating that the actuator is able to render virtual stiffness and damping fields in ranges potentially useful in human-robot interaction schemes for gait assistance.

4.6 A new design

In this section another SEA design currently under development will be briefly presented. This preliminary bench prototype is quite different from the one reported in the previous sections in terms of architecture and components and it designed to overcome its performance limitations. The system will be described and some tests on the spring stiffness measurement will be reported.

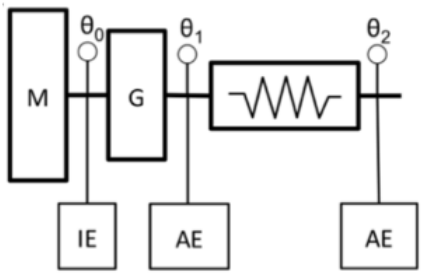

Figure 4.22: SEA sensorization based on absolute measurements: the motor (M) shaft rotation (θ_0) is measured using an incremental encoder (IE) while the gear (G) output shaft rotation (θ_1) and the SEA output shaft rotation (θ_2) are measured using absolute encoders (AE).

4.6.1 Prototype components

A 300 W brushless DC motor (Maxon EC4-pole 45) with a maximum continuous torque of 635 mN·m was used. It is equipped with Hall sensors for current commutation and with a 2048 counts per turns optical incremental encoder to measure motor rotation with a resolution of 0.044 deg (quadrature reading). A double stage reduction mechanism is employed: a 4.3:1 planetary gear (Maxon GP42) with 0.9 efficiency and a 15:1 hypoid gear with 0.85 efficiency. Total reduction ratio is 64.5:1 with 0.77 efficiency to get high back-drivability of the system. This motor-gear combination guarantees a nominal speed of 5.8 rad/s and a nominal torque of 30.5 N·m (a peak torque of a about 40 N·m is expected to be provided by the motor on the basis of estimated thermal limitations).

Two magnetic absolute encoders (Renishaw RM44, resolution: 0.044 deg) are directly connected to the two extremities of the elastic element. In Fig. 4.22 the whole system sensorization is reported: the motor (M) shaft rotation (θ_0) is measured using an incremental encoder (IE) while the gear (G) output shaft rotation (θ_1) and the SEA output shaft rotation (θ_2) are measured using absolute encoders (AE).

As for the previously presented prototype a monolithic disc-shaped design has been pursued for the elastic element. A stiffness of 200 N·m·rad^{-1} was considered as target value to be achieved using two equal compliant discs with stiffness 400 N·m·rad^{-1} serially connected. This choice was motivated by the highly demand-

Figure 4.23: Picture of the custom torsion springs composing the spring pack. Dimensions: 80 mm external diameter 10 mm axial length. A shaped shaft-hub coupling based on P3G polygon is used as connection between the two springs internal rings. Steel mechanical hard stops are visible.

ing requirement on the maximum loading torque. For each disc, compliance is due to four 90 deg spaced replications of flexible snaky lamellae, as shown in Fig. 4.23.

The shape and dimensions of such flexible elements were designed through an iterative FEM simulations-based design and optimization process. Static stress-strain analysis was performed considering W720 material (maraging steel 300, Young modulus 1.86 GPa, nominal yield stress 1.91 GPa and ultimate tensile strength 1.96 GPa). Considering a maximum torque of 40 N·m a deflection of 0.1025 rad was achieved for each of the two serial springs which results in a stiffness $K_{s,FEM} = 390$ N·m·rad^{-1}. The physical prototype was manufactured by WEDM; total dimensions of each compliant disc are 80 mm for the outer diameter and 10 mm for the thickness. The total spring pack, consisting of the serially connected discs has a thickness of 26 mm. It is worth noticing the use of a P3G polygon shaped internal ring to optimize springs interconnections minimizing backlash, and the introduction of mechanical hard stops to prevent possible breaking if torques higher than the maximum allowed ones are accidentally applied.

Fig. 4.24 depicts a 3D drawing of the proposed system while Fig. 4.25 shows a picture of the prototype. The overall dimensions are 335 × 164 × 90 mm^3 and the total actuator mass is 3.1 kg.

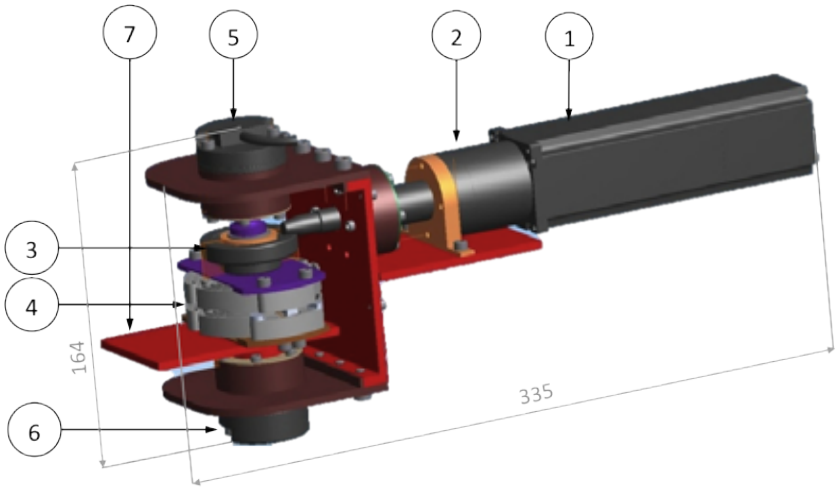

Figure 4.24: 3D drawing of the rotary SEA. 1: DC motor, 2: planetary gear, 3: hypoid gear, 4: spring pack, 5-6: absolute encoders, 7: output link. Dimensions: $335 \times 164 \times 90$ mm^3. Total mass: 3.1 kg.

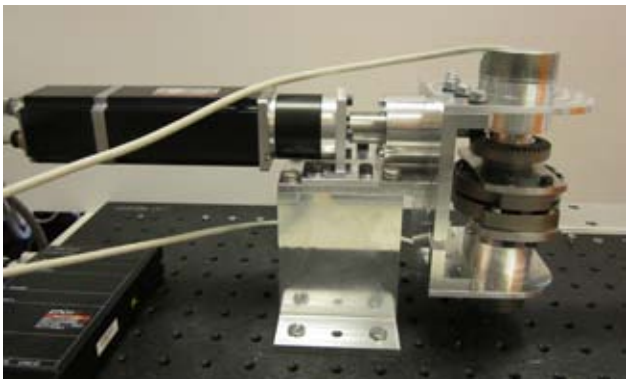

Figure 4.25: Picture of the assembled SEA prototype: the frame is fixed to an aluminum block, while the actuator output shaft is connected to a thin rectangular link..

Nevio Luigi Tagliamonte

4.6.1.1 Spring pack characterization

To experimentally evaluate torque-deflection characteristic of each spring, the test-bed reported in Fig. 4.26 was used. A gearmotor (Maxon EC 45 250 W plus planetary gear Maxon GP 52 C 126:1) equipped with an incremental encoder (Avago HEDL 9140, resolution 500 cpt), able to provide 45 N·m peak torque, was connected to the spring with an interposed torque sensor (Lorenz Messtechnik GmbH DR-2, nominal measurable torque 50 N·m). A flexible coupling (Rodoflex ATMK60L77, nominal torque 60 N·m) was also employed to avoid spurious forces due to possible misalignments. An incremental magnetic encoder (ASM, PMIS4 reading sensor head and PMIR4 magnetic code wheel, resolution 32768 cpt) was used to directly monitor spring internal ring rotation, while the external ring was kept fixed to the frame.

Characterization procedure consisted in commanding the gearmotor with a position ramps at 1 deg/s and reversing when 40 N·m torque was measured.

Results for the torque-deflection curves (fitted using linear regression) of the two spring pack components are reported in Fig. 4.27 (a maximum backlash of about ±1 deg can be noticed). The spring of Fig. 4.27a has a stiffness of 284 N·m·rad^{-1} for positive angles and 289 N·m·rad^{-1} for negative angles. The mean value of 287 N·m·rad^{-1} presents a 26% discrepancy with respect to the simulated one. The spring of Fig. 4.27b has a stiffness of 303 N·m·rad^{-1} for positive angles and 311 N·m·rad^{-1} for negative angles. The mean value of 307 N·m·rad^{-1} shows a 21% discrepancy with respect to the simulated one. The serial connection of these two elements produces a stiffness of 148 N·m·rad^{-1} with a total 24% discrepancy with respect to simulated value. This deviation is in accordance with results obtained in section 4.4.1 and with literature studies [56].

4.6.2 Conclusions

A new preliminary SEA design is described with several improvements with respect to the previously presented one. The use of a hypoid gear allows decentralizing motor mass from the output shaft axis (motor axis and output shaft axis are perpendicular) thus distributing the actuator weight alongside a human limb if the system is integrated in an active orthosis. A novel spring pack composed of two

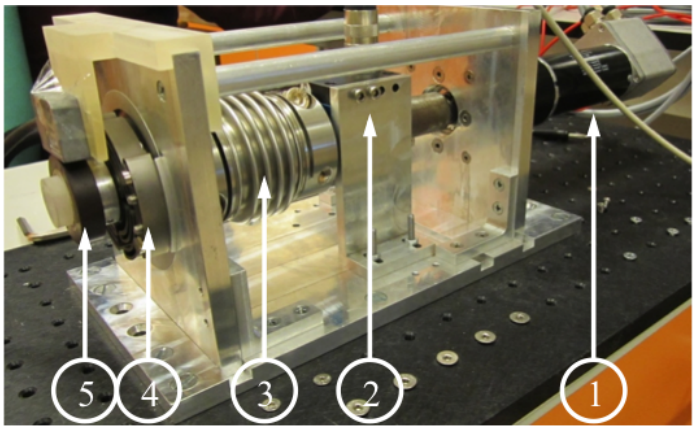

Figure 4.26: Test-bed for springs characterization. 1: gearmotor plus encoder, 2: torque sensor, 3: flexible coupling, 4: spring, 5: magnetic incremental encoder.

custom-shaped compliant steel discs (designed through FEM simulations) has been characterized using a dedicated test-bed, verifying resistance up to 40 N·m torque. Torque-deflection characteristic has been evaluated demonstrating high linearity and stiffness value which deviates of 26% and 21% from the simulated value (serial connection of the two springs causes a total deviation of 24% with respect to the expected value). Low backlash and high back-drivability are guaranteed by a P3G polygon shape coupling between springs and high efficiency of the planetary-hypoid gears transmission system. Two absolute encoder monitor rotations of the spring input and output shafts (i.e. transmission mechanism and SEA outputs respectively) thus excluding gearmotor backlash from torque measurement. Absolute readings provide simpler and more effective initialization procedure in measuring SEA output position and residual spring pack deflection. An extensive experimental characterization of performances, according to procedures presented in the previous sections, and an optimization of this bench prototype are planned as future work.

Nevio Luigi Tagliamonte

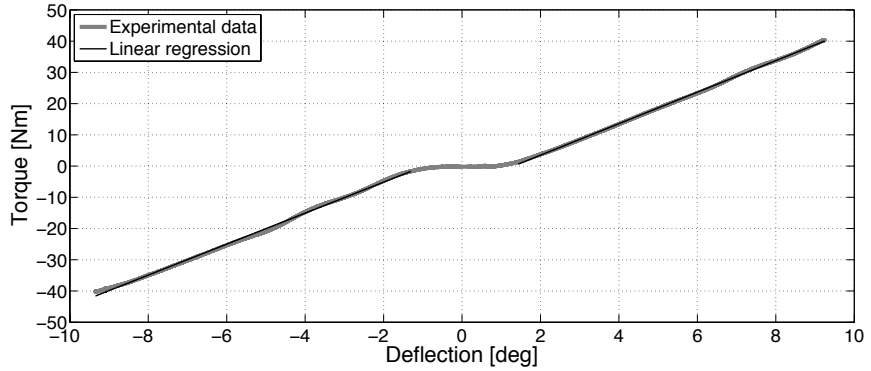

(a)

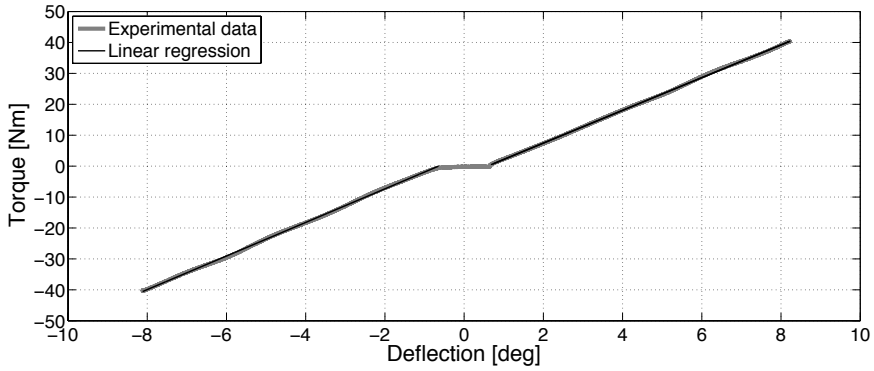

(b)

Figure 4.27: Torque-angle characteristics for the two series springs. (a) Spring 1: stiffness 284 N·m·rad^{-1} for positive angles and 289 N·m·rad^{-1} for negative angles. The mean value of 287 N·m·rad^{-1} shows a 26% discrepancy with respect to the simulated one. (b) Spring 2: stiffness 303 N·m·rad^{-1} for positive angles and 311 N·m·rad^{-1} for negative angles. The mean value of 307 N·m·rad^{-1} shows a 21% discrepancy with respect to the simulated one.

Chapter 5

Design and characterization of a passive Visco Elastic Joint

As presented in previous chapters useful behaviors can emerge from the interaction of robots with the environment and, in case of wearable rehabilitation or assistive machines, with the human body. As in the case of quasi-passive bipedal robots [4], for example, optimal dynamical properties can be attained if elastic components are properly exploited; the same can be assumed for damping elements, especially in the case of walking robots were masses have to opportunely decelerated in some gait phases. Hence the introduction of passive mechanical components (springs and dampers) in robotic joints can enable useful mechanical energy bouncing between a robot and the human body and stabilizing properties for the structure. Moreover, for rehabilitation machines elastic components can be employed to produce resistive torques for challenging the patient. In both cases different level of compliance and/or torque-angle characteristics can be required to achieve different to adapt to different patients and/or therapy. As described in the case of double actuation systems for impedance regulation (see chapter 3), these components add complexity to the design, which reverberates on increased mass and volume.

State-of-the-art solutions for robotic joints springs and dampers have been extensively presented in chapters 3 and 4. Here only a brief recalling will be reported. As it regards torsion springs, the approaches investigated so far can be grouped into:

i) systems using linear compression springs arranged so to produce torsion elasticity ([51, 53, 99, 135, 66]); *ii)* systems based on leaf springs ([81, 57, 84]); *iii)* systems using simple commercial torsion springs or flexible joints ([50, 54, 58, 64]); systems using custom-shaped compliant elements ([56, 53]).

As it regards dampers, they are often designed based on electrorheological [96, 97] or magnetorheological [98, 100] fluids. In these systems, the rheological properties of the fluid, and the resultant damping, are controlled through an electric or magnetic field. These solutions show some drawbacks in terms of large volume, high weight and mechanical complexity. An alternative approach focuses on frictional dampers, where energy is dissipated in the contact between moving parts. In this case damping can be modulated by modifying the contact of two surfaces [95, 101, 102]. These systems have the advantage of being compact and lightweight, but they may be expectedly affected by surfaces wearing.

In this chapter a compact rotary passive ViscoElastic Joint (pVEJ), comprising a torsion Stiffness module (Sm) and a torsion Damping module (Dm) acting in parallel on the output shaft is presented. The impedance of the system can be manually pre-set. This kind of joint can be used in wearable robots, wherever a torque-angle/velocity characteristic is properly selected for optimal energy exchange with the human body and the environment. For demonstration purposes some representative viscoelastic properties have been rendered in the presented prototype, considering values compatible with robots for gait assistance.

5.1 Design requirements

The pVEJ is intended as a passive (i.e. not actuated) joint for lower limbs active orthoses, in order to establish a dynamical coupling with the human body and the environment. For this reason, the target ranges for torsion stiffness and damping coefficients to be rendered by the pVEJ have been chosen to be of the same order of magnitude of those exhibited by the human lower limbs joints [136, 137]: the stiffness has to vary from 0 to 1.7 N m/deg, the damping from 0 to $3.5 \cdot 10^{-2}$ Nm s/deg. Moreover, in the intended application, as described in the previous section, torsion stiffness should not be constrained to be constant, but it should vary with joint

angle. For demonstration purposes, constant, linear and a quadratic stiffness-angle characteristic have been considered. A prototype with these three behaviors has been developed and tested within this thesis even though, as it will be shown in the following sections, other stiffness-angle relations can be easily considered, by purposively shaping an interchangeable cam disc. The maximum input torque is set to 50 Nm and dimensional constraints were fixed to 150 mm for the diameter and 100 mm for the axial length.

5.2 Concept and dimensioning

5.2.1 Stiffness module

The Sm is implemented using n linear compression springs connected between the joint shaft and n rollers sliding on cam profiles. This arrangement generates a centering elastic torque against an external rotation θ of the joint shaft. In Fig. 5.1 a schematic representation of one functional element of the Sm is depicted (only one spring k_m is represented). A desired stiffness-angle characteristic $k_\theta = f(\theta)$ can be achieved by opportunely selecting the shape of the cam $r(\theta)$. This profile can be derived equating the work associated with the application of an external torque and the variation in the elastic energy of the n springs.

By neglecting the radius of the cam follower rollers (*knife-edge* model), the cam profile $r(\theta)$, generating an arbitrary torsion stiffness k_θ, is:

$$r(\theta) = \sqrt{\frac{2}{n\,k_m} \int_0^\theta d\alpha \int_0^\theta k_\theta(\alpha) d\alpha} \tag{5.1}$$

The expression (5.1) corresponds to the *pitch curve* of the cam, which coincides to the *working curve* in the case of a knife-edge follower but not in the case of a roller follower. The effects of this simplification are discussed in the next sections.

Constant, linear and quadratic stiffness-angle characteristics can be obtained respectively by setting $k_\theta(\theta) = K$, $k_\theta(\theta) = A\theta$ and $k_\theta(\theta) = B\theta^2$ in (5.1) with K, A and B constant values. This substitution leads to:

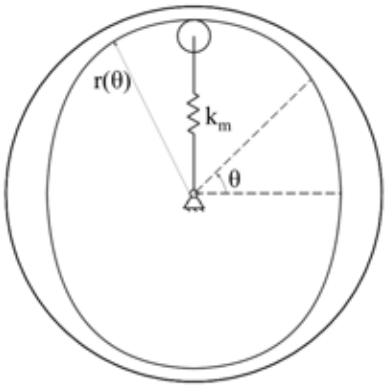

Figure 5.1: Schematic representation of one functional element of the torsion Sm, (only one linear spring is considered). k_m is the spring stiffness, θ is the shaft rotation and $r(\theta)$ is the cam profile.

$$r_{const}(\theta) = r_0 - \sqrt{\frac{K}{nk_m}}\theta \tag{5.2}$$

$$r_{lin}(\theta) = r_0 - \sqrt{\frac{A}{3nk_m}}\theta^{\frac{3}{2}} \tag{5.3}$$

$$r_{quad}(\theta) = r_0 - \sqrt{\frac{B}{6nk_m}}\theta^2 \tag{5.4}$$

where r_0 is the springs rest position. Expressions (5.2)-(5.4) are graphically represented through polar plot in Fig. 5.2.

5.2.2 Damping module

In the Dm the joint shaft is connected to a roller, pushed against a silicone tube filled with a viscous fluid (mineral oil). The tube endings are connected together, to form a circular closed circuit. In this way, the rotation of the shaft forces the circulation of the fluid in the tube. A localized pressure drop, adjustable manually by acting on a valve, produces viscous stresses which, in case of laminar flow, generate a resistive torque on the shaft proportional to the joint angular velocity. Figure 5.3 shows a schematic representation of the Dm.

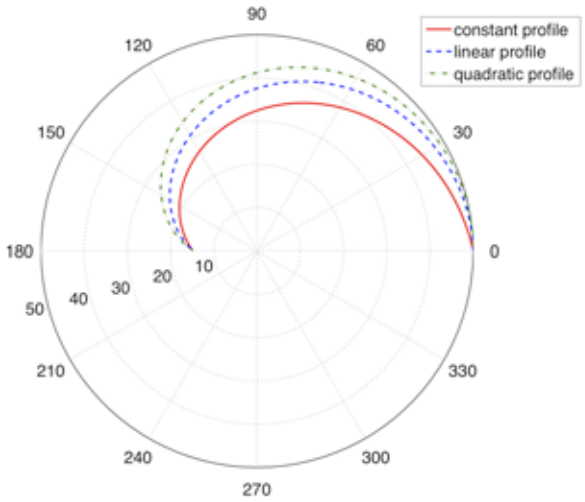

Figure 5.2: Graphical representation of expressions (5.2)-(5.4) for constant, linear and quadratic stiffness-angle characteristic of the Sm.

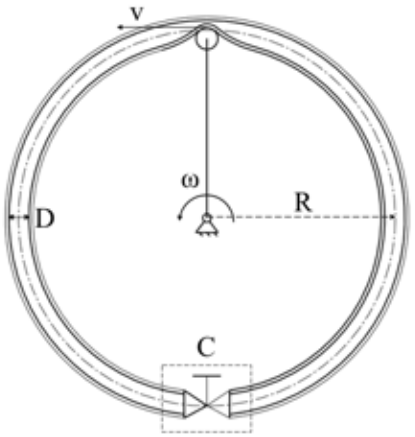

Figure 5.3: Schematic representation of the torsion Dm. ω is the angular velocity, R is the radius of curvature of the center line of the tube, D the inner diameter of the tube and v the linear velocity of the roller. The valve is schematized in block C.

When the valve is completely open the damping is minimum but not zero, because the circulation of the viscus fluid in the tube dissipates some energy. The minimum damping can be calculated equating the power associated to the shaft rotation and the power dissipated by fluid internal friction[1]. This leads to:

[1]Assuming laminar flow in the tube Poiseuille law can be used to express volumetric flow rate.

$$c_{min} = 16\pi^2 \mu R^3 \tag{5.5}$$

where R is the radius of curvature of the center line of the tube and μ is the dynamic viscosity of the fluid. Equation (5.5) accounts for fluid viscosity effects, but it neglects energy dissipation occurring during the hysteretic large deformations of the silicone tube. For this reason, (5.5) must be considered an under-estimation of the actual minimum value of the damping coefficient. The maximum achievable can be theoretically considered infinite if the lumen of the tube is completely closed. Clearly in the real prototype, silicon tube deformations always allow a small circulation of the fluid.

5.3 Prototype components

Fig. 5.4 shows an exploded view of the pVEJ. The prototype is depicted in Fig. 5.6; dimensions are: 115 mm (diameter) × 85 mm (axial length). The overall joint mass is 1.4 kg.

An ASM magnetic incremental encoder (reading sensor PMIS4, magnetic wheel PMIR4; resolution of 32768 counts per turn, 0.003 deg with quadrature reading) is mounted on the output shaft, with the reading part fixed to the joint frame and the magnetic wheel coupled to the rotating shaft.

5.3.1 Stiffness module

The Sm is implemented using 4 linear compression springs, each one pushing one roller on a segment of a cam. The desired stiffness can be achieved by shaping the cam profile according to (5.2)–(5.4).

In particular, once fixed the number and stiffness of the springs and the maximum rotation of the joint (± 27 deg), a stiffness of 1.7 N m/rad in correspondence of this extremal rotation is desired for the three analyzed characteristics. This choice leads to the calculation of stiffness coefficients, derived from (5.2)-(5.4), and of the joint maximum torque as reported in Table 5.1.

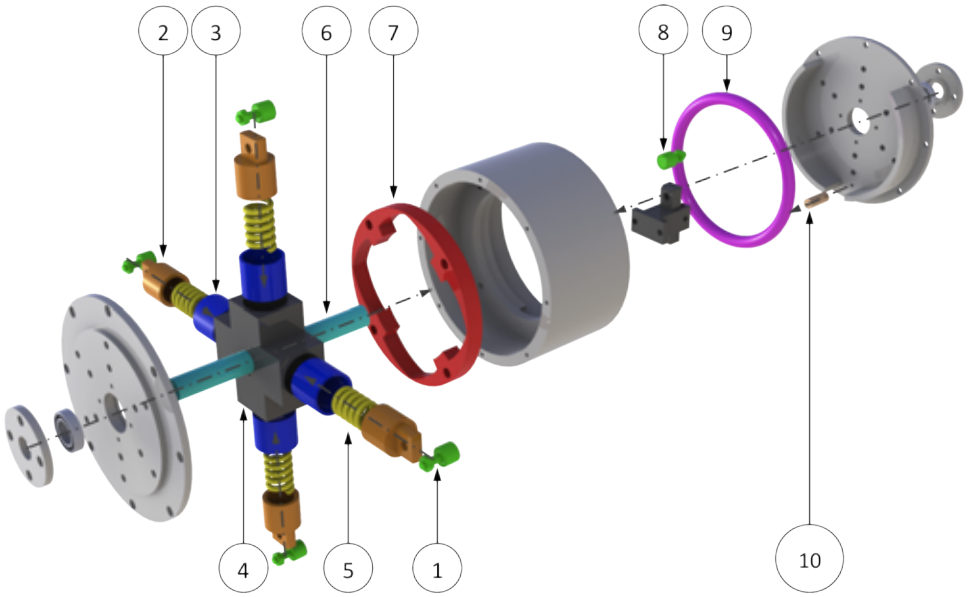

Figure 5.4: Exploded view of the pVEJ. 1: cam follower rollers, 2: roller-spring connectors, 3: bushings, 4: central hub, 5: linear compression springs, 6: joint shaft, 7: cam profiles, 8: fluid mover, 9: silicone tube, 10: pressure drop regulator.

Table 5.1: Properties of possible Sm module configurations considering constant, linear and quadratic stiffness-angle characteristics.

	Stiffness-angle characteristic $k_\theta(\theta)$		
	Constant: $k_\theta = K$	Linear: $k_\theta = A\theta$	Quadratic: $k_\theta = B\theta^2$
Stiffness parameter	$K = 1.745$ Nm/deg	$A = 6.4{\cdot}10^{-2}$ Nm/deg^2	$B = 2.5{\cdot}10^{-3}$ Nm/rad^3
Springs number n	4		
Max rotation	$\pm$ 27 deg		
Max torque	47 Nm	24 Nm	16 Nm

Nevio Luigi Tagliamonte

(a) (b) (c)

Figure 5.5: Cam disc of the Sm with constant (a), linear (b) and quadratic (c) stiffness-angle characteristic.

The prototype includes: a central hub (Fig. 5.4-4) rigidly connected to a shaft (Fig. 5.4-6); four harmonic steel springs with stiffness 140.9 N/mm (Fig. 5.4-5); four roller-spring connectors (Fig. 5.4-2); four cam follower rollers (Fig. 5.4-1); a disc with four internal cam profile segments (Fig. 5.4-7); four self-lubricating bushings (MU - Boccole Italia S.r.l.) (Fig. 5.4-3). The shaft is supported by two radial ball bearings. The joint elastic properties can be changed by replacing the cam-shaped discs and/or the number/stiffness of the compression springs. Three cam discs have been designed, corresponding to constant, linear and quadratic stiffness-angle characteristics (in Fig. 5.5 the manufactured discs are reported).

5.3.2 Damping module

The Dm is implemented by connecting the joint shaft to a roller (Fig. 5.4-8), which compresses a silicone tube filled with mineral oil (grade SAE 80w90; dynamic viscosity range at room temperature: 1.0 - 1.3 Pa s (Fig. 5.4-9). The tube has an outer diameter of 8 mm and an inner diameter of 5 mm. The radius R of the center line of the closed loop is 47 mm. The valve consists of a screw (metric, M4, pitch: 0.7 mm) which pushes a teflon cylinder on the tube, thus locally reducing its lumen. When the valve is fully open (minimum localized pressure drop, maximum tube lumen), the minimum value of the torsion damping is achieved. According to (5.5) the theoretical minimum damping, with the selected mineral oil, ranges from

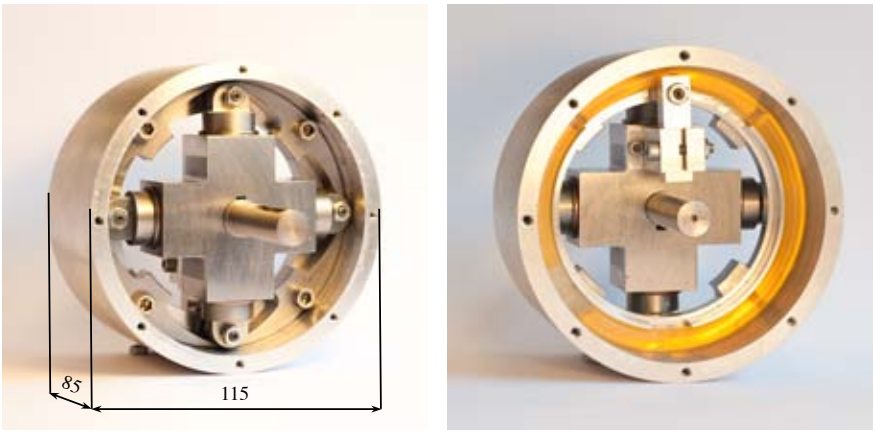

(a) (b)

Figure 5.6: Picture of the pVEJ prototype: Sm (a), Dm (b). Dimensions are in mm.

$2.8 \cdot 10^{-4}$ Nm s/deg to $3.7 \cdot 10^{-4}$ Nm s/deg.

5.4 Prototype characterization

To experimentally measure the stiffness and the damping of the pVEJ, the custom dynamometric test-bed already presented in chapter 4 was employed (Fig. 5.7).

The test-bed is equipped with a torque sensor (Lorenz Messtechnik GmbH DR-2, nominal measurable torque 50 Nm) connected between a gearmotor and the pVEJ. The gearmotor comprises a Maxon EC45 250 W brushless DC motor, a Maxon GP 52C planetary gear (reduction ratio 126:1) and an optical incremental encoder (Avago HEDL 9140, resolution: 0.18 deg). The maximum continuous deliverable torque is 30 N·m with a peak torque of 45 N·m. The flexible coupling (Rodoflex ATMK60L77, nominal torque 60 N·m) avoids spurious forces and radial misalignments between pVEJ and sensor shafts. The elements introduced between the gearmotor and the pVEJ do not negatively affect the measurements on the Sm, since, based on components datasheets, the equivalent undesired series elasticity between the gearmotor and the pVEJ is an order of magnitude (about 40 times) higher than the maximum one to be tested.

The motor is position/velocity-controlled using a Maxon EPOS2 50/5 control

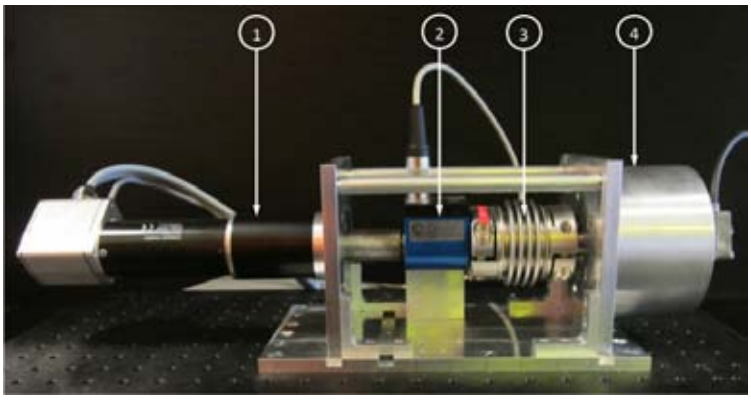

Figure 5.7: Dynamometric test-bed for pVEJ characterization. 1: gearmotor, 2: torque sensor, 3: flexible coupling, 4: pVEJ with encoder.

unit; high level commands are sent though the CompactRIO-9022 central control unit as already described in chapter 4.

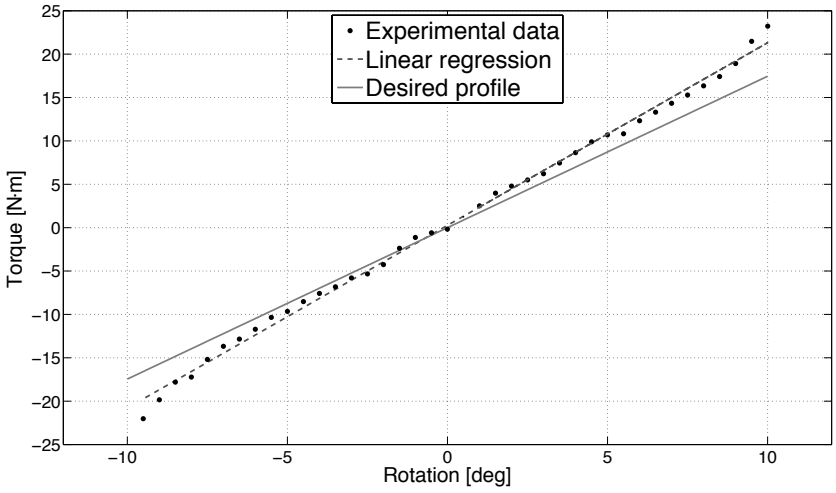

Figure 5.8: Torque-angle profile for the constant stiffness-angle characteristic of the Sm. Experimental data are regressed as $\tau = \hat{K}\,\theta$, with $\hat{K} = 2.105$ Nm/deg ($R^2 = 0.99$).

Nevio Luigi Tagliamonte

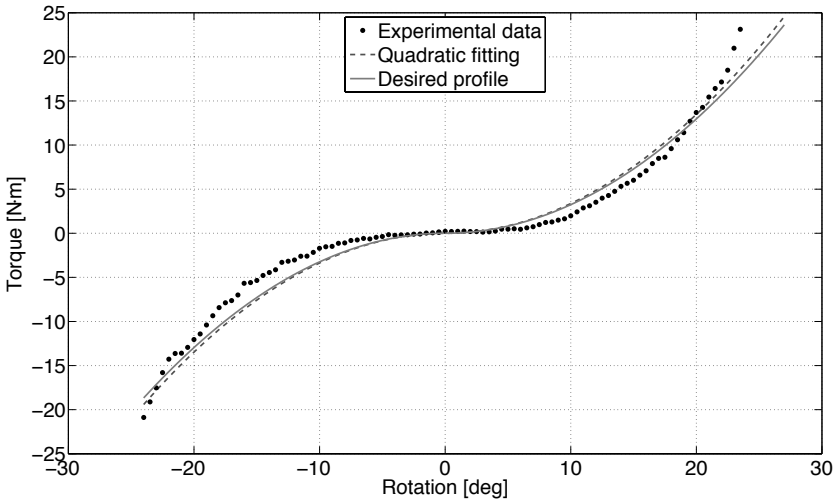

Figure 5.9: Torque.angle profile for the linear stiffness-angle characteristic of the Sm. Experimental data are regressed as $\tau = \frac{1}{2}\hat{A}\,\theta^2\,\mathrm{sign}(\theta)$, with $\hat{A} = 0.066$ Nm deg^{-2} ($R^2 = 0.96$).

5.4.1 Stiffness module

For the characterization of the Sm, the Dm was unmounted and the test gear-motor was commanded to track a position profile consisting of a sequence of steps (amplitude 0.5 deg, duration 2 s), starting from the position where the pVEJ applied a null torque. For each step of imposed rotation, torque values measured through the torque sensor during steady state were averaged, resulting in the torque-rotation curves shown in Figures 5.8 – 5.10.

The characteristic for the constant stiffness cam profile is shown in Fig. 5.8. Linear regression of the experimental data in the form $\tau = \hat{K}\,\theta$ resulted in a stiffness estimation $\hat{K} = 2.105$ Nm/deg, which differs from the desired one ($K = 1.745$ Nm/deg) by 20%. The linear regression provided a R^2 coefficient of 0.99.

Curve fitting was performed also on the experimental data of the linear stiffness profile. A regression in the form $\tau = \frac{1}{2}\hat{A}\,\theta^2\,\mathrm{sign}(\theta)$ was performed to determine the A coefficient introduced in section 5.2. The estimated value $\hat{A} = 0.066$ Nm deg^{-2} differs by only 3% from the desired value ($6.4 \cdot 10^{-2}$ Nm deg^{-2}). The R^2 coefficient of the fitting was 0.96.

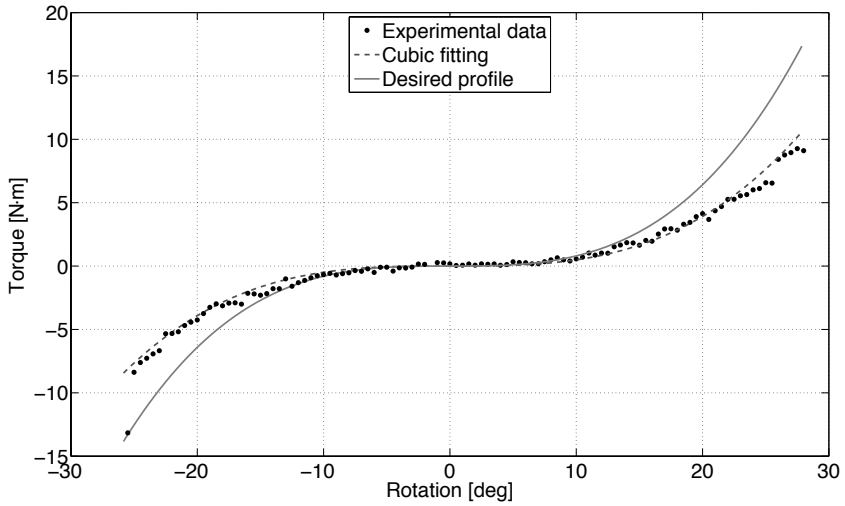

Figure 5.10: Torque-angle profile for the quadratic stiffness-angle characteristic of the Sm. Experimental data are regressed as $\tau = \frac{1}{3}\hat{B}\,\theta^3$, with $\hat{B} = 1.47{\cdot}10^{-3}$ Nm deg^{-3} ($R^2 = 0.97$).

Fitting of the experimental data of the quadratic stiffness profile was performed to estimate the B parameter of the expression introduced in section 5.2 using relation $\tau = \frac{1}{3}\hat{B}\,\theta^3$. Cubic regression estimated a parameter value $\hat{B} = 1.47{\cdot}10^{-3}$ Nm deg^{-3} differing by around 50% from the desired value of 2.5 $\cdot 10^{-3}$ Nm deg^{-3}. The overall goodness of fit of the cubic model was however demonstrated by the high R^2 coefficient obtained in the fitting, which equals to 0.97. In contrast, quadratic fitting of the same experimental data had a lower R^2 coefficient (0.93).

5.4.2 Damping module

The Dm was characterized with the linear springs unmounted to exclude the elastic effect of the Sm. Characterization procedure consisted in rotating the pVEJ shaft with a constant velocity in the range [5, 35] deg/s with increases of 5 deg/s. A torque-velocity regression in the form $\tau = \hat{c}\,\dot{\theta}$ was performed. This test was repeated at three valve positions. Let δ indicate the linear displacement of the screw, $\delta = 0$ mm corresponds to the case when the valve is fully open, while $\delta = 1.4$ mm and $\delta = 2.1$ mm correspond to 2 and 3 turns of the screw, respectively.

In Fig. 5.11 torque-velocity fitting of the experimental data for these three con-

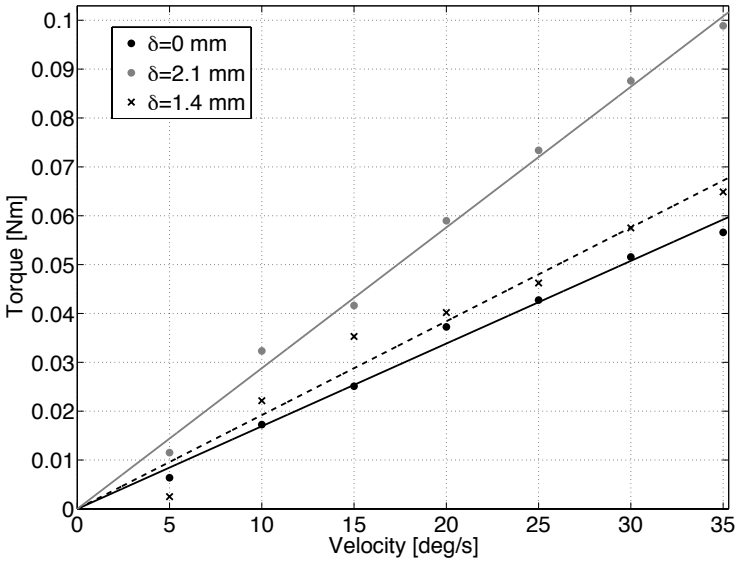

Figure 5.11: Torque-angular velocity characteristics for the Dm. The slopes of the curves represent the torsion damping coefficients for the three different valve regulations. For $\delta = 0$ mm $\hat{c}_{min} = 1.69{\cdot}10^{-3}$ Nm s/deg ($R^2 = 0.99$); for $\delta = 1.4$ mm $\hat{c} = 1.92{\cdot}\ 10^{-3}$ Nm s/deg ($R^2 = 0.96$); δ= 2.1 mm $\hat{c} = 2.88{\cdot}\ 10^{-3}$ Nm s/deg ($R^2 = 0.99$).

ditions are reported.

The slopes of the curves are but the damping coefficients; in particular, for $\delta =$ 0 mm the estimated damping is $\hat{c}_{min} = 1.69{\cdot}10^{-3}$ Nm s/deg with a R^2 coefficient of 0.98. For δ= 1.4 mm $\hat{c} = 1.92{\cdot}10^{-3}$ Nm s/deg with R^2 equal to 0.96. In the case of $\delta = 2.1$ mm $\hat{c} = 2.88{\cdot}\ 10^{-3}$ Nm s/deg with a R^2 coefficient of 0.99.

5.5 Discussion and conclusions

The prototype of a passive rotary mechanical device was presented, which integrates a torsion spring and damper acting in parallel on the same output shaft. The system is compact and lightweight, and it allows an easy modification of the mechanical impedance by replacing a single component or regulating a screw valve. Characterization of the the submodules (Sm and Dm) was performed. For the Sm, constant, linear and quadratic stiffness-angle profiles were correctly rendered (as demonstrated by the high R^2 coefficient in regressions) with stiffness values differing

from the expected ones by 3% to 50%. Such discrepancy is due to two main causes: *i)* approximation used in (5.1), where a knife-edge model for the cam follower was adopted, thus neglecting the radius of the roller (5 mm in the prototype). The discrepancy can be reduced at design time by using a model that takes into account the radius of the cam follower. The high values of R^2, though, demonstrate that the desired behaviors (i.e. linear, quadratic or cubic) were attained up to a multiplicative constant, which can be easily set experimentally.

With regards to the Dm, the high R^2 values for the three tests performed demonstrate the capability of the system to behave as a torsion damper with a good accuracy. Moreover, the possibility of modifying the damping coefficient through a simple valve regulation has been demonstrated. Of note, the damping coefficient, measured when the valve is fully open, is one order of magnitude higher than the minimum theoretical value, evaluated using (5.5). The difference between the experimental and theoretical values is likely due to simplifications introduced in the analytical calculation. In particular, in the prototype the damping is higher than the theoretical one because: *i)* energy losses associated to tube compression increases the resultant damping action; *ii)* a further localized pressure drop occurs at the connector between the two ends of the tube. Nonetheless, the experimentally obtained damping coefficient is still one order of magnitude smaller than the target one (section 5.2). Higher values can be achieved by further closing the valve, although the robustness of the silicone tube must be verified against the fluidic pressures that would build in it. Other options may include the use oils with a higher viscosity.

Chapter 6

Conclusions

The development of robotic systems for pHRI in rehabilitation and assistive applications demands for advanced solutions in terms of mechanical structure, actuation system and control strategies. To cope with complexity of the human body and of the neural adaptation mechanisms several issues such as safety, dynamical adaptability, biomechanical and neuromotor compatibility have to be handled.

This thesis provides contributions for the improvement of pHRI with respect to two topics: the analysis of human intrinsic motor strategies and effects of robots perturbations (Part I), the design of components (passive and active joints) for compliant wearable robots (Part II).

Neural mechanisms underlying human motor control in pHRI have to be understood to design robots not hindering physiological motion and neural strategies adopted by the brain. In this regards, the thesis presented a work on human wrist movements during kinematically redundant pointing tasks in free motion and during the interaction with a state-of-the-art highly back-drivable robot which is currently used for post-stroke neurorehabilitation therapy. During assessment a constraining behavior was demonstrated and the effects of system mechanical impedance reduction were analyzed by means of a basic direct force control scheme. After reducing robot impedance subjects regained natural motor behavior with features similar to the ones exhibited during free motion. The work demonstrated the need of coping with *neural strategies* in performing motor tasks, which are not properly taken into

account in current design of rehabilitation robots and it emphasized the possibility of minimizing perturbations to human natural motion even using simple solutions like a well known direct force control approach.

Intrinsic dynamical properties of robots can greatly benefit from the use of compliant actuators and passive joints with visco-elastic properties, especially for optimal interaction with the external environment and human body. In this regards, this thesis dealt with the analysis of rotary double actuation compliant systems used to separately control position and impedance in different application fields. A classification was introduced, including three main categories: *serial*, *parallel* and *physically controllable impedance*. A critical analysis of the relevant features of each presented architecture was carried out, identifying some common traits for the introduced categories. The overview and comparison of these systems can represent a general guideline for future designs of actuators. On this basis a new actuation system, Variable Impedance Differential Actuator (VIDA), was proposed. Based on an electromechanical model of the system, expected performances in different conditions were evaluated through simulations. The system comprised two active elements serially connected through a differential transmission to regulate position and impedance through two distinct SISO controls of the two input output shafts.

New prototypes of active and passive joints were also presented and performances were experimentally verified. The proposed rotary SEA is a particular implementation of a more general modular architecture, and it fulfills requirements of a knee assistive device. A major novelty element of the system is the compliant element which was purposively designed and fabricated. Lower stiffness than expected was experimentally experienced probably due to discrepancy between nominal and actual properties of the employed material and to fabrication inaccuracies. A velocity-sourced type torque control scheme was implemented to regulate a maximum torque of 10 N·m with a bandwidth of 5 Hz. These performances were evaluated experimentally using non parametric system identification techniques. Impedance control was also implemented and response to externally applied perturbations were measured, demonstrating the capability of rendering virtual stiffness and damping fields

in ranges compatible with human assistance applications. A preliminary design of a more powerful SEA, with motor mass decentralized with respect to the spring and the output shaft, was also described and the characterization of the elastic elements was reported.

A purely mechanical rotary passive ViscoElastic Joint (pVEJ) was presented, which integrated a torsion spring (Stiffness module, Sm) and damper (Damping module, Dm) acting in parallel. The system allows an easy pre-set of the mechanical impedance by replacing a single component and regulating viscous friction through a valve. Experimental characterization of the submodules was performed. For the Sm, constant, linear and quadratic stiffness-angle profiles were correctly rendered, with stiffness values slightly differing from the expected ones due to approximations of the analytical model used for cam design and to fabrication inaccuracies. The capability of the Dm to behave as a torsion damper also with regulable properties was assessed. The experimental minimum damping was found to be one order of magnitude higher than the theoretical value. This discrepancy was likely due to to simplifications introduced in the analytical calculation. In particular, in the prototype energy losses associated to tube compression and a further localized pressure drop occurring at the connector between the two ends of the tube increased the resultant damping action.

6.1 Future works

Starting from the presented thesis, many activities can be foreseen as future works. The design of novel machines optimizing human-robot interaction in assistance and rehabilitation applications can leverage guidelines introduced here regarding *i)* robots compatibility with human neural strategies underlying motor tasks, and *ii)* variable impedance actuators designs, based on their classification and comparative analysis. Moreover, developed and tested compact active and passive components, i.e. rotary SEAs and pVEJ can be included in wearable robots with compliant structural properties.

Regarding specific activities reported in this thesis, a more extensive investigation is planned on human-robot interaction during pointing tasks with the wrist. The pre-

sented method could allow to examine the effects of different levels of back-drivability on human natural movements and to point out which is the range of impedance values able to avoid constraining behaviors, thus suggesting new requirements for the design of rehabilitation robots which currently only consider biomechanical aspects.

Developed active and passive joints will be used in the research framework of the European Project EVRYON[1]. The project explores a novel design methodology for wearable robots with the aim of embedding proper mechanical properties (*structural embodied intelligence*) so that the intrinsic human-robot coupling can elicit a target physiological movement as emerging dynamics; the methodology is applied to the development of a robot for gait assistance. This design is pursued using co-optimization computational methods where robot morphology (topological links-joints interconnections and kinematic/dynamic properties) and control undergo an artificial evolution. Co-evolutionary algorithms run in a physics-based simulation environment where human body is modeled (based on real biomechanical data) and robot morphology/control features are opportunely parametrized and encoded. Based on the results of the co-optimization process, an actual prototype is going to be developed, including components described in this thesis. In particular, the presented bench SEA prototype, with distributed architecture, will be optimized and experimentally characterized to be integrated in the hip and knee flexion/extension modules. A CAD drawing of the robot currently under development is reported in Fig. 6.1.

Moreover, an activity recently started in thigh collaboration with the Laboratory of Bioinspired Robotics (BIOROB) of the École Polytechnique Fédérale de Lausanne (EPFL), aims at applying the mentioned co-evolutionary approach to design a system able to assist knee movements in sitting condition while exploiting its own intrinsic dynamics coupled to that of the human leg. The design of this 1-DOF system is meant to be a simplified *proof of concept* of the proposed methodology and it can represent an important starting point to understand potentialities and limitations of the approach. In the prototype to be developed, the rotary SEA presented in this thesis will be employed (see Fig. 6.2).

The same actuator is expected to be included also in a wearable active orthosis

[1]FP7 FET Proactive Initiative Embodied Intelligence of the European Commission, project no. ICT-2007.8.5-231451 - EVRYON (EVolving morphologies for human-Robot sYmbiotic interactiON).

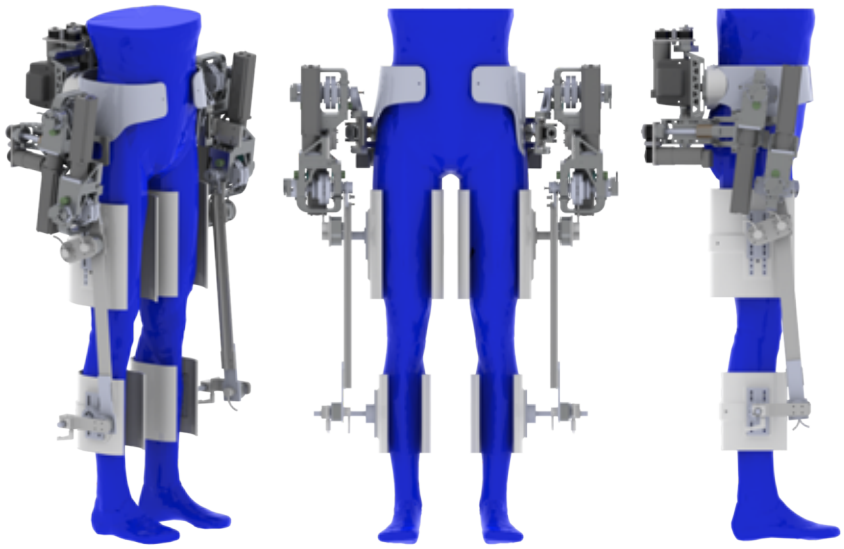

Figure 6.1: CAD drawing of the robot under development within the framework of the EVRYON project: the design is guided by co-evolutionary simulations. For the knee and hip flexion/extension modules, optimized versions of the presented distributed SEAs are employed.

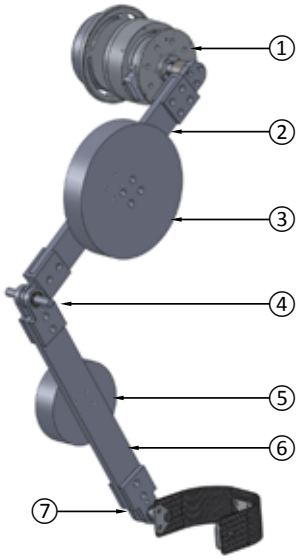

Figure 6.2: CAD drawing of a representative morphology for a knee assistive robot designed through co-evolutionary optimization method. The presented SEA is included. 1: SEA, 2, 6: links, 3, 5: additional masses, 4: elastic joint, 7: passive joint.

Nevio Luigi Tagliamonte

Figure 6.3: CAD drawing of an assistive knee orthosis integrating the presented SEA.

for knee assistance during overground walking, as represented in Fig. 6.3.

For these applications further characterization tests will be performed, also considering in details coupled stability issues and verifying effectiveness of the system within an actual human robot-interaction scenario.

Regarding the pVEJ device, an on-line damping control system will be introduced by connecting the pressure regulator to a motor. Further experimental activities could include the analysis of damping capability in the case of fluids with higher viscosity, and a dynamical characterization of the system to evaluate inertial properties and other sources of damping/elasticity. Therefore, since the prototype has been mainly developed for demonstration purposes, a further optimization of mass and weight can be pursued to improve integration in actual wearable robot designs. Possible uses as passive series element of active joints can be foreseen.

Nevio Luigi Tagliamonte

Appendix A

Kinematics of the InMotion^3 wrist robot

In section 2.2.1 kinematic operators for the InMotion^3 robot were used. Here more details are reported, based on the kinematic scheme of Fig. 2.4.

Let $\boldsymbol{p}_{ij}$ indicate the 3×1 position vector of the origin of frame j from the origin of frame i and $\boldsymbol{R}_{ij}$ the 3×3 rotation matrix describing the orientation of frame j with respect to frame i. The related *homogeneous representation* is given by the matrix:

$$\boldsymbol{g}_{ij} = \begin{bmatrix} \boldsymbol{R}_{ij} & \boldsymbol{p}_{ij} \\ \boldsymbol{0} & 1 \end{bmatrix} \tag{A.1}$$

In particular, for the three frames of Fig. 2.4:

$$\boldsymbol{g}_{o1} = \begin{bmatrix} \cos(\mathrm{t}_1) & 0 & \sin(\mathrm{t}_1) & 0 \\ \sin(\mathrm{t}_1) & 0 & -\cos(\mathrm{t}_1) & 0 \\ 0 & 1 & 0 & (l+d) \\ 0 & 0 & 0 & 1 \end{bmatrix} \tag{A.2}$$

$$\boldsymbol{g}_{12} = \begin{bmatrix} -\sin(\mathrm{t}_2) & 0 & -\cos(\mathrm{t}_2) & a \\ \cos(\mathrm{t}_2) & 0 & -\sin(\mathrm{t}_2) & 0 \\ 0 & -1 & 0 & 0 \\ 0 & 0 & 0 & 1 \end{bmatrix} \tag{A.3}$$

Nevio Luigi Tagliamonte

$$\boldsymbol{g}_{2s} = \begin{bmatrix} \cos(\mathrm{t}_3) & -\sin(\mathrm{t}_3) & 0 & b\cos(\mathrm{t}_3) \\ \sin(\mathrm{t}_3) & \cos(\mathrm{t}_3) & 0 & b\sin(\mathrm{t}_3) \\ 0 & 0 & 1 & c \\ 0 & 0 & 0 & 1 \end{bmatrix} \tag{A.4}$$

and

$$\boldsymbol{g}_{os} = \boldsymbol{g}_{o1}(\mathrm{t}_1)\boldsymbol{g}_{12}(\mathrm{t}_2)\boldsymbol{g}_{2s}(\mathrm{t}_3) \tag{A.5}$$

$$\boldsymbol{g}_{o2} = \boldsymbol{g}_{o1}(\mathrm{t}_1)\boldsymbol{g}_{12}(\mathrm{t}_2) \tag{A.6}$$

A.1 Direct kinematics

Based on (A.1), direct kinematics in terms of $\boldsymbol{R}_{os}$ matrix and $\boldsymbol{p}_{os}$ vector (as introduced in section 2.2.1) can be written as:

$$\begin{aligned}
\boldsymbol{R}_{os}[1,1] &= -\sin(\mathrm{t}_1)\sin(\mathrm{t}_3) - \cos(\mathrm{t}_1)\cos(\mathrm{t}_3)\sin(\mathrm{t}_2) \\
\boldsymbol{R}_{os}[1,2] &= \cos(\mathrm{t}_1)\sin(\mathrm{t}_2)\sin(\mathrm{t}_3) - \cos(\mathrm{t}_3)\sin(\mathrm{t}_1) \\
\boldsymbol{R}_{os}[1,3] &= -\cos(\mathrm{t}_1)\cos(\mathrm{t}_2) \\
\boldsymbol{R}_{os}[2,1] &= \cos(\mathrm{t}_1)\sin(\mathrm{t}_3) - \cos(\mathrm{t}_3)\sin(\mathrm{t}_1)\sin(\mathrm{t}_2) \\
\boldsymbol{R}_{os}[2,2] &= \cos(\mathrm{t}_1)\cos(\mathrm{t}_3) + \sin(\mathrm{t}_1)\sin(\mathrm{t}_2)\sin(\mathrm{t}_3) \\
\boldsymbol{R}_{os}[2,3] &= -\cos(\mathrm{t}_2)\sin(\mathrm{t}_1) \\
\boldsymbol{R}_{os}[3,1] &= \cos(\mathrm{t}_2)\cos(\mathrm{t}_3) \\
\boldsymbol{R}_{os}[3,2] &= -\cos(\mathrm{t}_2)\sin(\mathrm{t}_3) \\
\boldsymbol{R}_{os}[3,3] &= -\sin(\mathrm{t}_2) \\
\boldsymbol{p}_{os}[1,1] &= a\cos(\mathrm{t}_1) - c\cos(\mathrm{t}_1)\cos(\mathrm{t}_2) - b\sin(\mathrm{t}_1)\sin(\mathrm{t}_3) - b\cos(\mathrm{t}_1)\cos(\mathrm{t}_3)\sin(\mathrm{t}_2) \\
\boldsymbol{p}_{os}[2,1] &= a\sin(\mathrm{t}_1) + b\cos(\mathrm{t}_1)\sin(\mathrm{t}_3) - c\cos(\mathrm{t}_2)\sin(\mathrm{t}_1) - b\cos(\mathrm{t}_3)\sin(\mathrm{t}_1)\sin(\mathrm{t}_2) \\
\boldsymbol{p}_{os}[3,1] &= d + l - c\sin(\mathrm{t}_2) + b\cos(\mathrm{t}_2)\cos(\mathrm{t}_3)
\end{aligned}$$

A.2 Jacobian matrix

Jacobian matrix is calculated as reported in [138]:

$$\boldsymbol{J} = \begin{bmatrix} \boldsymbol{z}_o \wedge (\boldsymbol{p}_{os} - \boldsymbol{p}_o) & \boldsymbol{z}_1 \wedge (\boldsymbol{p}_{os} - \boldsymbol{p}_{o1}) & \boldsymbol{z}_2 \wedge (\boldsymbol{p}_{os} - \boldsymbol{p}_{o2}) \\ \boldsymbol{z}_o & \boldsymbol{z}_1 & \boldsymbol{z}_2 \end{bmatrix} \tag{A.7}$$

in which

$$\boldsymbol{z}_o = \begin{bmatrix} 0 & 0 & 1 \end{bmatrix}^T \tag{A.8}$$

$$\boldsymbol{z}_1 = \begin{bmatrix} \boldsymbol{g}_{o1}[1,3] & \boldsymbol{g}_{o1}[2,3] & \boldsymbol{g}_{o1}[3,3] \end{bmatrix}^T \tag{A.9}$$

$$\boldsymbol{z}_2 = \begin{bmatrix} \boldsymbol{g}_{o2}[1,3] & \boldsymbol{g}_{o2}[2,3] & \boldsymbol{g}_{o2}[3,3] \end{bmatrix}^T \tag{A.10}$$

$$\boldsymbol{p}_o = \begin{bmatrix} 0 & 0 & 0 \end{bmatrix}^T \tag{A.11}$$

$$\boldsymbol{p}_{o1} = \begin{bmatrix} \boldsymbol{g}_{o1}[1,4] & \boldsymbol{g}_{o1}[2,4] & \boldsymbol{g}_{o1}[3,4] \end{bmatrix}^T \tag{A.12}$$

$$\boldsymbol{p}_{o2} = \begin{bmatrix} \boldsymbol{g}_{o2}[1,4] & \boldsymbol{g}_{o2}[2,4] & \boldsymbol{g}_{o2}[3,4] \end{bmatrix}^T \tag{A.13}$$

The resulting elements of the matrix (A.7) are:

$$
\begin{aligned}
\boldsymbol{J}[1,1] &= c\cos(t_2)\sin(t_1) - b\cos(t_1)\sin(t_3) - a\sin(t_1) + b\cos(t_3)\sin(t_1)\sin(t_2)\\
\boldsymbol{J}[1,2] &= \cos(t_1)[c\sin(t_2) - b\cos(t_2)\cos(t_3)]\\
\boldsymbol{J}[1,3] &= \cos(t_2)\sin(t_1)[c\sin(t_2) - b\cos(t_2)\cos(t_3)] - \sin(t_2)[c\cos(t_2)\sin(t_1) +\\
&- b\cos(t_1)\sin(t_3) + b\cos(t_3)\sin(t_1)\sin(t_2)]\\
\boldsymbol{J}[2,1] &= a\cos(t_1) - c\cos(t_1)\cos(t_2) - b\sin(t_1)\sin(t_3) - b\cos(t_1)\cos(t_3)\sin(t_2)\\
\boldsymbol{J}[2,2] &= \sin(t_1)[c\sin(t_2) - b\cos(t_2)\cos(t_3)]\\
\boldsymbol{J}[2,3] &= \sin(t_2)[c\cos(t_1)\cos(t_2) + b\sin(t_1)\sin(t_3) + b\cos(t_1)\cos(t_3)\sin(t_2)] +\\
&- \cos(t_1)\cos(t_2)[c\sin(t_2) - b\cos(t_2)\cos(t_3)]\\
\boldsymbol{J}[3,2] &= \sin(t_1)[a\sin(t_1) + b\cos(t_1)\sin(t_3) - c\cos(t_2)\sin(t_1) - b\cos(t_3)\sin(t_1)\sin(t_2)] +\\
&- \cos(t_1)[c\cos(t_1)\cos(t_2) - a\cos(t_1) + b\sin(t_1)\sin(t_3) + b\cos(t_1)\cos(t_3)\sin(t_2)]\\
\boldsymbol{J}[3,3] &= \cos(t_1)\cos(t_2)[c\cos(t_2)\sin(t_1) - b\cos(t_1)\sin(t_3) + b\cos(t_3)\sin(t_1)\sin(t_2)] +\\
&- \cos(t_2)\sin(t_1)[c\cos(t_1)\cos(t_2) + b\sin(t_1)\sin(t_3) + b\cos(t_1)\cos(t_3)\sin(t_2)]\\
\boldsymbol{J}[4,2] &= \sin(t_1)\\
\boldsymbol{J}[4,3] &= -\cos(t_1)\cos(t_2)\\
\boldsymbol{J}[5,2] &= -\cos(t_1)\\
\boldsymbol{J}[5,3] &= -\cos(t_2)\sin(t_1)\\
\boldsymbol{J}[6,1] &= 1\\
\boldsymbol{J}[6,3] &= -\sin(t_2)\\
\boldsymbol{J}[3,1] &= \boldsymbol{J}[4,1] = \boldsymbol{J}[5,1] = \boldsymbol{J}[6,2] = 0
\end{aligned}
$$

A.3 Adjoint matrix

According to (2.11) the elements of the adjoint matrix are:

$$
\begin{aligned}
\boldsymbol{Ad}_{g_{os}}[1,1] &= -\sin(t_1)\sin(t_3) - \cos(t_1)\cos(t_3)\sin(t_2) \\
\boldsymbol{Ad}_{g_{os}}[1,2] &= \cos(t_1)\sin(t_2)\sin(t_3) - \cos(t_3)\sin(t_1), -\cos(t_1)\cos(t_2) \\
\boldsymbol{Ad}_{g_{os}}[1,3] &= -\cos(t_1)\cos(t_2) \\
\boldsymbol{Ad}_{g_{os}}[1,5] &= c\sin(t_2) - l - d - b\cos(t_2)\cos(t_3) \\
\boldsymbol{Ad}_{g_{os}}[1,6] &= a\sin(t_1) + b\cos(t_1)\sin(t_3) - c\cos(t_2)\sin(t_1) - b\cos(t_3)\sin(t_1)\sin(t_2) \\
\boldsymbol{Ad}_{g_{os}}[2,1] &= \cos(t_1)\sin(t_3) - \cos(t_3)\sin(t_1)\sin(t_2) \\
\boldsymbol{Ad}_{g_{os}}[2,1] &= \cos(t_1)\cos(t_3) + \sin(t_1)\sin(t_2)\sin(t_3) \\
\boldsymbol{Ad}_{g_{os}}[2,3] &= -\cos(t_2)\sin(t_1) \\
\boldsymbol{Ad}_{g_{os}}[2,4] &= d + l - c\sin(t_2) + b\cos(t_2)\cos(t_3) \\
\boldsymbol{Ad}_{g_{os}}[2,6] &= c\cos(t_1)\cos(t_2) - a\cos(t_1) + b\sin(t_1)\sin(t_3) + b\cos(t_1)\cos(t_3)\sin(t_2) \\
\boldsymbol{Ad}_{g_{os}}[3,1] &= \cos(t_2)\cos(t_3) \\
\boldsymbol{Ad}_{g_{os}}[3,2] &= -\cos(t_2)\sin(t_3) \\
\boldsymbol{Ad}_{g_{os}}[3,3] &= -\sin(t_2) \\
\boldsymbol{Ad}_{g_{os}}[3,4] &= c\cos(t_2)\sin(t_1) - b\cos(t_1)\sin(t_3) - a\sin(t_1) + b\cos(t_3)\sin(t_1)\sin(t_2) \\
\boldsymbol{Ad}_{g_{os}}[3,5] &= a\cos(t_1) - c\cos(t_1)\cos(t_2) - b\sin(t_1)\sin(t_3) - b\cos(t_1)\cos(t_3)\sin(t_2) \\
\boldsymbol{Ad}_{g_{os}}[4,4] &= -\sin(t_1)\sin(t_3) - \cos(t_1)\cos(t_3)\sin(t_2) \\
\boldsymbol{Ad}_{g_{os}}[4,5] &= \cos(t_1)\sin(t_2)\sin(t_3) - \cos(t_3)\sin(t_1) \\
\boldsymbol{Ad}_{g_{os}}[4,6] &= -\cos(t_1)\cos(t_2) \\
\boldsymbol{Ad}_{g_{os}}[5,4] &= \cos(t_1)\sin(t_3) - \cos(t_3)\sin(t_1)\sin(t_2) \\
\boldsymbol{Ad}_{g_{os}}[5,5] &= \cos(t_1)\cos(t_3) + \sin(t_1)\sin(t_2)\sin(t_3) \\
\boldsymbol{Ad}_{g_{os}}[5,6] &= -\cos(t_2)\sin(t_1) \\
\boldsymbol{Ad}_{g_{os}}[6,4] &= \cos(t_2)\cos(t_3) \\
\boldsymbol{Ad}_{g_{os}}[6,5] &= -\cos(t_2)\sin(t_3) \\
\boldsymbol{Ad}_{g_{os}}[6,6] &= -\sin(t_2) \\
\boldsymbol{Ad}_{g_{os}}[1,4] &= \boldsymbol{Ad}_{g_{os}}[2,5] = \boldsymbol{Ad}_{g_{os}}[3,6] = \boldsymbol{Ad}_{g_{os}}[4,1] = \boldsymbol{Ad}_{g_{os}}[4,2] = \boldsymbol{Ad}_{g_{os}}[4,3] \\
&= \boldsymbol{Ad}_{g_{os}}[5,1] = \boldsymbol{Ad}_{g_{os}}[5,2] = \boldsymbol{Ad}_{g_{os}}[5,3] = \boldsymbol{Ad}_{g_{os}}[6,1] = \boldsymbol{Ad}_{g_{os}}[6,2] \\
&= \boldsymbol{Ad}_{g_{os}}[6,3] = 0
\end{aligned}
$$

List of Publications

Journal papers

1. **N. L. Tagliamonte**, M. Scorcia, D. Formica, D. Campolo, E. Guglielmelli, "Effects of Impedance Reduction of a Robot for Wrist Rehabilitation on Human Motor Strategies in Healthy Subjects during Pointing Tasks, *Advanced Robotics - special issue on Physical Human-Robot Interaction Through Force Interface*, vol. 25, pp. 537-562, 2011.

2. **N. L. Tagliamonte**, F. Sergi, D. Accoto, G. Carpino, E. Guglielmelli "Double actuation architectures for varying impedance in compliant robots", submitted to *Mechatronics*.

3. F. Sergi, D. Accoto, **N. L. Tagliamonte**, G. Carpino, E. Guglielmelli, "A systematic graph-based method for the kinematic synthesis of non-anthropomorphic wearable robots for the lower limbs", *Journal of Frontiers of Mechanical Engineering*, vol. 6, no. 1, pp. 61-70, 2011.

4. G. Carpino, D. Accoto, F. Sergi, **N. L. Tagliamonte**, E. Guglielmelli, "A Novel Compact Torsional Spring for Modular Series Elastic Actuators for Assistive Wearable Robots", submitted to *Journal of Mechanical Design*.

Peer-reviewed international conference papers

1. **N. L. Tagliamonte**, D. Formica, D. Campolo, E. Guglielmelli, "Coping with Intrinsic Constraints of Neural Origin in the Design of Rehabilitation Robots: a Preliminary Study, *The 4th International IEEE/EMBS Conference on Neural Engineering (NER)*, Antalya, Turkey, April 2009, pp. 124-127.

2. **N. L. Tagliamonte**, F. Sergi, G. Carpino, D. Accoto, E. Guglielmelli, "Design of a Variable Impedance Differential Actuator for Wearable Robotics Applications", *Pro-*

ceedings of the IEEE/RSJ International Conference on Intelligent Robots and Systems (IROS), Taipei, Taiwan, October 2010.

3. **N. L. Tagliamonte**, M. Scorcia, D. Formica, D. Campolo, E. Guglielmelli, "Force Control of a Robot for Wrist Rehabilitation: towards Coping with Human Intrinsic Constraints, *Proceedings of the IEEE/RSJ International Conference on Intelligent Robots and Systems (IROS), Taipei, Taiwan*, October 2010.

4. D. Accoto, **N. L. Tagliamonte**,G. Carpino, F. Sergi, M. Di Palo, E. Guglielmelli, "A Novel Modular Passive Viscoelastic Joint for Wearable Robots", accepted to *IEEE International Conference on Robotics and Automation (ICRA) St. Paul, Minnesota, USA*, May 2012.

5. F. Sergi, D. Accoto, **N. L. Tagliamonte**, G. Carpino, E. Guglielmelli, "Graph-based methodology for the kinematic synthesis of wearable assistive robots for the lower limbs", *32nd International Conference of the IEEE Engineering in Medicine and Biology Society (EMBC), Buenos Aires, Argentina*, September 2010.

6. F. Sergi, D. Accoto, **N. L. Tagliamonte**, G. Carpino, L. Pathiyil, E. Guglielmelli, "A systematic graph- based method for the kinematic synthesis of non anthropomorphic wearable robots", *IEEE International Conference on Cybernetics and Intelligent Systems - Robotics, Automation and Mechatronics, Singapore*, June 2010.

7. G. Carpino, D. Accoto, M. Di Palo, **N. L. Tagliamonte**, F. Sergi, E. Guglielmelli, "Design of a Rotary Passive Viscoelastic Joint for Wearable Robots", *Proceedings of the International Conference of Rehabilitation Robotics (ICORR), Zurich, Switzerland*, July 2011.

8. M. Scorcia, D. Formica, **N. L. Tagliamonte**, D. Campolo, E. Guglielmelli, "Effects on human motor strategies of physical interaction with a force-controlled wrist rehabilitation robot", *IEEE/RAS-EMBS International Conference on Biomedical Robotics and Biomechatronics (BIOROB), Tokyo, Japan*, September 2010.

9. F. Sergi, D. Accoto,G. Carpino, **N. L. Tagliamonte**, E. Guglielmelli, "Development and Characterization of a Compact Rotary Series Elastic Actuator for Knee Assistance During Overground Walking", submitted to *IEEE/RAS-EMBS International Conference on Biomedical Robotics and Biomechatronics (BIOROB)*, Rome, Italy, June 2012.

Nevio Luigi Tagliamonte

Abstracts in international conferences

1. **N. L. Tagliamonte**, M. Scorcia, D. Formica, D. Campolo, E. Guglielmelli, "Force Control of a Robot for Wrist Rehabilitation: towards Coping with Human Intrinsic Contraints, *The Seventh IARP Workshop on Technical Challenges for Dependable Robots in Human Environments, Toulouse, France*, June 2010.
2. D. Accoto, **N. L. Tagliamonte**, F. Sergi, G. Carpino, E. Guglielmelli, "VIDA: a Variable Impedance Differential Actuator", *Workshop on New variable impedance actuators for the next generation of robots, International Conference on Robotics and Automation (ICRA), Anchorage, AK, USA*, May 2010.
3. D. Accoto, G. Carpino, **N. L. Tagliamonte**, M. Di Palo, F. Sergi, E. Guglielmelli, "Active and Passive Devices for Tuning Impedance in Wearable Robotics, *Workshop on Biologically-inspired Actuation at the International Conference on Robotics and Automation (ICRA), Shangai, China*, May 2011.
4. D. Accoto, F. Sergi, G. Carpino, **N. L. Tagliamonte**, E. Guglielmelli, "A design methodology for neurorehabilitative and assistive wearable robots incorporating embodied intelligence", *14th European Congress on Clinical Neurophysiology (ECCN), Rome, Italy*, May 2011.

Peer-reviewed national conference papers

1. **N. L. Tagliamonte**, F. Sergi, D. Accoto, G. Carpino, E. Guglielmelli, "Modellazione e Controllo di Un Attuatore Differenziale ad Impedenza Variabile per Robot Esoscheletrici", *Neuroriabilitazione robotica dell'arto superiore, Genova, Italy*, December 2009.
2. **N. L. Tagliamonte**, M. Scorcia, D. Formica, D. Campolo, E. Guglielmelli, "Controllo di Forza di un Robot per la Neuroriabilitazione del Polso per il Rispetto dei Vincoli di Natura Neurale, *Neuroriabilitazione Robotica dell'Arto Superiore, Genova, Italy*, December 2009.
3. M. Scorcia, D.Formica, **N. L. Tagliamonte**, D. Campolo, E. Guglielmelli, "Coping with intrinsic constraints: force control for a wrist rehabilitation robot, *Secondo Congresso Nazionale di Bioingegneria, Torino, Italy*, July 2010.
4. G. Carpino, F. Sergi, D. Accoto, E. Fischetti, **N. L. Tagliamonte**, E. Guglielmelli, "Design di giunti rotoidali per robot indossabili non antropomorfi", *Neuroriabilitazione Robotica dell'Arto Superiore, Genova, Italy*, December 2009.

Nevio Luigi Tagliamonte

Technical reports

1. **N. L. Tagliamonte**, G. Carpino, F. Sergi, M. Di Palo, D. Accoto and E. Guglielmelli, "Development of VIJs", *Deliverable 5.2 of the Evryon-EEU-Project, FP7-ICT-2007.8.5-231451*, January 2011.

2. F. Sergi, G. Carpino, **N. L. Tagliamonte**, D. Accoto and E. Guglielmelli, "Basic contraints on robot design", *Deliverable 5.1 of the Evryon-EEU-Project, FP7-ICT-2007.8.5-231451*, July 2009.

3. G. Carpino, A. Toth, **N. L. Tagliamonte**, S. M. M. De Rossi, T. Lenzi, N. Vitiello, "Report on the basicrequirementsofthedesign of theactivelycontrolledhip module", *Deliverable 9.1 of the Evryon-EEU-Project, FP7-ICT-2007.8.5-231451*, October 2010.

Nevio Luigi Tagliamonte

Bibliography

[1] D Tweed and T Vilis. Geometric relations of eye position and velocity vectors during saccades. *Vision Research*, 30(1):111–127, 1990.

[2] D. G Liebermann, A Biess, J Friedman, C. C. A. M Gielen, and T Flash. Intrinsic joint kinematic planning. i: Reassessing the listing's law constraint in the control of three-dimensional arm movements. *Exp Brain Res*, 171(2):139–154, May 2006.

[3] Domenico Campolo, Domenico Formica, Eugenio Guglielmelli, and Flavio Keller. Kinematic analysis of the human wrist during pointing tasks. *Exp Brain Res*, 201(3):561–573, Mar 2010.

[4] Steve Collins, Andy Ruina, Russ Tedrake, and Martijn Wisse. Efficient Bipedal Robots Based on Passive-Dynamic Walkers. *Science*, 307(5712):1082–1085, February 2005.

[5] Rolf Pfeifer, Max Lungarella, and Fumiya Iida. Self-organization, embodiment, and biologically inspired robotics. *Science*, 318(5853):1088–1093, 2007.

[6] D. E. Whitney. Historical perspective and state of the art in robot force control. *Int. J. Rob. Res.*, 6:3–14, March 1987.

[7] J. Kenneth Salisbury. Active stiffness control of a manipulator in cartesian coordinates. 19:95–100, December 1980.

[8] N Hogan. Impedance control: An approach to manipulation: Parts I, II, and III. *Journal of Dynamics Systems, Measurement, and Control*, 107:1–24, 1985.

[9] M. H. Raibert and J. J. Craig. Hybrid Position/Force Control of Manipulators. *Trans. ASME J. Dyn. Sys., Meas., & Contr.*, 102, 1981.

[10] Judith D Schaechter. Motor rehabilitation and brain plasticity after hemiparetic stroke. *Prog Neurobiol*, 73(1):61–72, May 2004.

[11] Robert Teasell, Nestor A Bayona, and Jamie Bitensky. Plasticity and reorganization of the brain post stroke. *Top Stroke Rehabil*, 12(3):11–26, Aug 2005.

[12] H Krebs, N Hogan, M Aisen, and B Volpe. Robot-aided neurorehabilitation. *Rehabilitation Engineering, IEEE Transactions on*, 6(1):75 – 87, 1998.

[13] Robert Riener, Lars Lünenburger, and Gery Colombo. Human-centered robotics applied to gait training and assessment. *J Rehabil Res Dev*, 43(5):679, Jan 2006.

[14] D Reinkensmeyer, N Hogan, HI Krebs, SL Lehman, and PS Lum. Rehabilitators, robots and guides: new tools for neurological rehabilitation. In J Winters and PE Crago, editors, *Biomechanics and Neural Control of Posture and Movement*. Springer, Berlin, 2000.

[15] Hermano I Krebs, Mark Ferraro, Stephen P Buerger, Miranda J Newbery, Antonio Makiyama, Michael Sandmann, Daniel Lynch, Bruce T Volpe, and Neville Hogan. Rehabilitation robotics: pilot trial of a spatial extension for mit-manus. *JNER*, 1(1):5, Oct 2004.

[16] David J Reinkensmeyer, Leonard E Kahn, Michele Averbuch, Alicia Mckenna-Cole, Brian D Schmit, and W Zev Rymer. Understanding and treating arm movement impairment after chronic brain injury: Progress with the arm guide. *J Rehabil Res Dev*, 37(6):653–662, 2000.

[17] D Campolo, D Accoto, D Formica, and E Guglielmelli. Intrinsic constraints of neural origin: Assessment and application to rehabilitation robotics. *Robotics, IEEE Transactions on*, 25(3):492 – 501, 2009.

[18] A.M.F Wong. Listing's law: clinical significance and implications for neural control. *Survey of ophthalmology*, 49(6):563–575, 2004.

[19] M Fetter, T Haslwanter, H Misslich, and D Tweed. *Three-dimensional Kinematics of the Eye, Head and Limb Movements*. Harwood, Amsterdam, 1997.

[20] H Krebs, B Volpe, D Williams, J Celestino, S Charles, D Lynch, and N Hogan. Robot-aided neurorehabilitation: A robot for wrist rehabilitation. *Neural Systems and Rehabilitation Engineering, IEEE Transactions on*, 15(3):327 – 335, 2007.

[21] Reza Shadmehr and Ferdinando A. Mussa-Ivaldi. Adaptive Representation of Dynamics during Learning of a Motor Task. *The Journal of Neuroscience*, 14(5):3208–3224, 1994.

Nevio Luigi Tagliamonte

[22] Opher Donchin, Joseph T. Francis, and Reza Shadmehr. Quantifying generalization from trial-by-trial behavior of adaptive systems that learn with basis functions: theory and experiments in human motor control. *The Journal of neuroscience : the official journal of the Society for Neuroscience*, 23(27):9032–9045, October 2003.

[23] Jörn Diedrichsen, Olivier White, Darren Newman, and Níall Lally. Use-Dependent and Error-Based Learning of Motor Behaviors. *The Journal of Neuroscience*, 30(15):5159–5166, April 2010.

[24] N Tagliamonte, D Formica, D Campolo, and E Guglielmelli. Coping with intrinsic constraints of neural origin in the design of rehabilitation robots: A preliminary study. *Neural Engineering, 2009. NER '09. 4th International IEEE/EMBS Conference on*, pages 124 – 127, 2009.

[25] O Khatib. Inertial properties in robotic manipulation: An object-level framework. *International Journal of Robotics Research*, 14(1):19–36, 1995.

[26] R Volpe and P Khosla. A theoretical and experimental investigation of explicit force control strategies for manipulators. *Automatic Control, IEEE Transactions on*, 38(11):1634 – 1650, 1993.

[27] Richard M Murray, Zexiang Li, and S S Sastry. *A Mathematical Introduction to Robotic Manipulation*. CRC Press, Boca Raton, FL, 2005.

[28] E. Colgate and N. Hogan. An analysis of contact instability in terms of passive physical equivalents. In *Robotics and Automation, 1989. Proceedings., 1989 IEEE International Conference on*, pages 404 –409 vol.1, may 1989.

[29] S. Eppinger and W. Seering. Understanding bandwidth limitations in robot force control. In *Robotics and Automation. Proceedings. 1987 IEEE International Conference on*, volume 4, pages 904 – 909, mar 1987.

[30] W. S. Newman. Stability and performance limits of interaction controllers. *Journal of Dynamic Systems, Measurement, and Control*, 114(4):563–570, 1992.

[31] N. Hogan. Controlling impedance at the man/machine interface. In *Robotics and Automation, 1989. Proceedings., 1989 IEEE International Conference on*, pages 1626 –1631 vol.3, may 1989.

Nevio Luigi Tagliamonte

[32] S. P. Buerger. Stable, high-force, low-impedance robotic actuators for human-interactive machines. *Ph.D. dissertation, Massachusetts Inst. Technol. (MIT), Cambridge*, 2005.

[33] Hermano I. Krebs, Mark Ferraro, Stephen P. Buerger, Miranda J. Newbery, Antonio Makiyama, Michael Sandmann, Daniel Lynch, Bruce T. Volpe, and Neville Hogan. Rehabilitation robotics: pilot trial of a spatial extension for MIT-Manus. *J Neuroengineering Rehabil*, 1(1), October 2004.

[34] A De Santis, B Siciliano, A De Luca, and A Bicchi. An atlas of physical human–robot interaction. *Mechanism and Machine Theory*, 43:253–270, Feb 2008.

[35] L Pfeffer, O Khatib, and J Hake. Joint torque sensory feedback in the control of a PUMA manipulator. *Robotics and Automation, IEEE Transactions on*, 5(4):418 – 425, 1989.

[36] A Albu-Schaffer, O Eiberger, M Grebenstein, S Haddadin, C Ott, T Wimbock, S Wolf, and G Hirzinger. Soft robotics. *Robotics & Automation Magazine, IEEE*, 15(3):20 – 30, 2008.

[37] R Filippini, S Sen, and A Bicchi. Toward soft robots you can depend on. *Robotics & Automation Magazine, IEEE*, 15(3):31 – 41, 2008.

[38] E Guglielmelli, M Johnson, and T Shibata. Guest editorial special issue on rehabilitation robotics. *Robotics, IEEE Transactions on*, 25(3):477 – 480, 2009.

[39] M Ishikawa, Paavo V Komi, Michael J Grey, Vesa Lepola, and Gert-Peter Bruggemann. Muscle-tendon interaction and elastic energy usage in human walking. *Journal of Applied Physiology*, 99(2):603–608, Aug 2005.

[40] S Au, P Dilworth, and H Herr. An ankle-foot emulation system for the study of human walking biomechanics. *Robotics and Automation, 2006. ICRA 2006. Proceedings 2006 IEEE International Conference on*, pages 2939 – 2945, 2006.

[41] M H Raibert. Hopping in legged systems–modeling and simulation for the 2D one-legged case. *IEEE Trans. Systems, Man, and Cybernetics*, 14:451–463, 1984.

[42] N Vitiello, E Cattin, S Roccella, F Giovacchini, F Vecchi, MC Carrozza, and P Dario. The NEURARM: towards a platform for joint neuroscience experiments on human motion control theories. *Intelligent Robots and Systems, 2007. IROS 2007. IEEE/RSJ International Conference on*, pages 1852–1857, 2007.

Nevio Luigi Tagliamonte

[43] Y Mukaibo, S Park, and T Maeno. Equilibrium point control of a robot arm with a double actuator joint. *International Simposium on Robotics and Automation*, 2004.

[44] A G Feldman. Functional tuning of the nervous system with control of movement or maintenance of steady posture, II: controllable parameters of the muscles. *Biophysics*, 11:565–578, 1966.

[45] A Bicchi and G Tonietti. Fast and "soft-arm" tactics [robot arm design]. *Robotics & Automation Magazine, IEEE*, 11(2):22 – 33, 2004.

[46] S Haddadin, A Albu-Schaffer, A De Luca, and G Hirzinger. Collision detection and reaction: A contribution to safe physical human-robot interaction. *Intelligent Robots and Systems, 2008. IROS 2008. IEEE/RSJ International Conference on*, pages 3356 – 3363, 2008.

[47] D Robinson. Design and analysis of series elasticity in closed-loop actuator force control. *Ph.D. dissertation, Massachusetts Inst. Technol. (MIT), Cambridge*, 2000.

[48] G Pratt and M Williamson. Series elastic actuators. *Intelligent Robots and Systems 95. 'Human Robot Interaction and Cooperative Robots', Proceedings. 1995 IEEE/RSJ International Conference on*, 1:399 – 406 vol.1, 1995.

[49] G Pratt, P Willisson, C Bolton, and A Hofman. Late motor processing in low-impedance robots: impedance control of series-elastic actuators. *American Control Conference, 2004. Proceedings of the 2004*, 4:3245 – 3251 vol.4, 2004.

[50] J Sensinger and R Weir. User-modulated impedance control of a prosthetic elbow in unconstrained, perturbed motion. *Biomedical Engineering, IEEE Transactions on*, 55(3):1043 – 1055, 2008.

[51] N Tsagarakis, M Laffranchi, B Vanderborght, and D Caldwell. A compact soft actuator unit for small scale human friendly robots. *Robotics and Automation, 2009. ICRA '09. IEEE International Conference on*, pages 4356 – 4362, 2009.

[52] J Veneman, R Ekkelenkamp, R Kruidhof, F van der Helm, and H van der Kooij. Design of a series elastic- and bowden cable-based actuation system for use as torque-actuator in exoskeleton-type training. *Rehabilitation Robotics, 2005. ICORR 2005. 9th International Conference on*, pages 496 – 499, 2005.

Nevio Luigi Tagliamonte

[53] A Stienen, E Hekman, H ter Braak, A Aalsma, F van der Helm, and H van der Kooij. Design of a rotational hydroelastic actuator for a powered exoskeleton for upper limb rehabilitation. *Biomedical Engineering, IEEE Transactions on*, 57(3):728 – 735, 2010.

[54] K Kong, J Bae, and M Tomizuka. A compact rotary series elastic actuator for human assistive systems. *Mechatronics, IEEE/ASME Transactions on*, PP(99):1 – 10, 2011.

[55] G Wyeth. Control issues for velocity sourced series elastic actuators. *Proceedings of Australasian Conference on Robotics and Automation 2006*, 2006.

[56] C Lagoda, A Schouten, A Stienen, E Hekman, and H van der Kooij. Design of an electric series elastic actuated joint for robotic gait rehabilitation training. *Biomedical Robotics and Biomechatronics (BioRob), 2010 3rd IEEE RAS and EMBS International Conference on*, pages 21 – 26, 2010.

[57] E Campbell, Z Kong, W Hered, A Lynch, M O'Malley, and J McLurkin. Design of a low-cost series elastic actuator for multi-robot manipulation. *Robotics and Automation (ICRA), 2011 IEEE International Conference on*, pages 5395 – 5400, 2011.

[58] Daniel Ragonesi, Sunil Agrawal, Whitney Sample, and Tariq Rahman. Series elastic actuator control of a powered exoskeleton. pages 3515–3518, Jun 2011.

[59] Ivar Thorson and Darwin Caldwell. A nonlinear series elastic actuator for highly dynamic motions. *Intelligent Robots and Systems (IROS), 2011 IEEE/RSJ International Conference on*, pages 390 – 394, 2011.

[60] N Hogan and P C Breedveld. The physical basis of analogies in physical system models. In Robert H. Bishop, editor, *The mechatronics handbook*. CRC Press, 1st edition, 2002.

[61] M Catalano, R Schiavi, and A Bicchi. Mechanism design for variable stiffness actuation based on enumeration and analysis of performance. *Robotics and Automation (ICRA), 2010 IEEE International Conference on*, pages 3285 – 3291, 2010.

[62] R Van Ham, T Sugar, B Vanderborght, K Hollander, and D Lefeber. Compliant actuator designs. *Robotics & Automation Magazine, IEEE*, 16(3):81 – 94, 2009.

[63] Byeong-Sang Kim, Jae-Bok Song, and Jung-Jun Park. A serial-type dual actuator unit with planetary gear train: Basic design and applications. *Mechatronics, IEEE/ASME Transactions on*, 15(1):108 – 116, 2010.

Nevio Luigi Tagliamonte

[64] M Lauria, MA Legault, MA Lavoie, and F Michaud. Differential elastic actuator for robotic interaction tasks. *Robotics and Automation, 2008. ICRA 2008. IEEE International Conference on*, pages 3606–3611, 2008.

[65] S Wolf, O Eiberger, and G Hirzinger. The DLR FSJ: Energy based design of a variable stiffness joint. *Robotics and Automation (ICRA), 2011 IEEE International Conference on*, pages 5082 – 5088, 2011.

[66] S Wolf and G Hirzinger. A new variable stiffness design: Matching requirements of the next robot generation. *Robotics and Automation, 2008. ICRA 2008. IEEE International Conference on*, pages 1741–1746, 2008.

[67] JW Hurst, JE Chestnutt, and AA Rizzi. An actuator with physically variable stiffness for highly dynamic legged locomotion. *Robotics and Automation, 2004. Proceedings. ICRA'04. 2004 IEEE International Conference on*, 5:4662–4667, 2004.

[68] O Eiberger, S Haddadin, M Weis, A Albu-Schäffer, and G Hirzinger. On joint design with intrinsic variable compliance: derivation of the DLR QA-Joint. *Robotics and Automation (ICRA), 2010 IEEE International Conference on*, pages 1687–1694, 2010.

[69] A Sharon, N Hogan, and D Hardt. High bandwidth force regulation and inertia reduction using a macro/micro manipulator system. *Robotics and Automation, 1988. Proceedings., 1988 IEEE International Conference on*, pages 126 – 132 vol.1, 1988.

[70] M Zinn, O Khatib, B Roth, and J Salisbury. Playing it safe [human-friendly robots]. *Robotics & Automation Magazine, IEEE*, 11(2):12 – 21, 2004.

[71] D Vischer and O Khatib. Design and development of high-performance torque-controlled joints. *Robotics and Automation, IEEE Transactions on*, 11(4):537 – 544, 1995.

[72] J Morrell and J Salisbury. Parallel coupled actuators for high performance force control: a micro-macro concept. *Intelligent Robots and Systems 95. 'Human Robot Interaction and Cooperative Robots', Proceedings. 1995 IEEE/RSJ International Conference on*, 1:391 – 398 vol.1, 1995.

[73] B Yi and R Freeman. Geometric characteristics of antagonistic stiffness in redundantly actuated mechanisms. *Robotics and Automation, 1993. Proceedings., 1993 IEEE International Conference on*, pages 654 – 661 vol.2, 1993.

Nevio Luigi Tagliamonte

[74] C English and D Russell. Mechanics and stiffness limitations of a variable stiffness actuator for use in prosthetic limbs. *Mechanism and Machine Theory*, 34:7–25, 1999.

[75] F Petit, M Chalon, W Friedl, M Grebenstein, A Schäffer, and G Hirzinger. Bidirectional antagonistic variable stiffness actuation: Analysis, design & implementation. *Robotics and Automation (ICRA), 2010 IEEE International Conference on*, pages 4189 – 4196, 2010.

[76] S Migliore, E Brown, and S DeWeerth. Biologically inspired joint stiffness control. *Robotics and Automation, 2005. ICRA 2005. Proceedings of the 2005 IEEE International Conference on*, pages 4508 – 4513, 2005.

[77] K Koganezawa. Mechanical stiffness control for antagonistically driven joints. *Intelligent Robots and Systems, 2005. (IROS 2005). 2005 IEEE/RSJ International Conference on*, pages 1544 – 1551, 2005.

[78] T Sonoda, Y Nishida, AAF Nassiraei, and K Ishii. Development of antagonistic wire-driven joint employing kinematic transmission mechanism. *Journal of Automation, Mobile Robotics & Intelligent Systems*, 4:62–70, 2010.

[79] C English and D Russell. Implementation of variable joint stiffness through antagonistic actuation using rolamite springs. *Mechanism and Machine Theory*, 34(1):27–40, 1999.

[80] D Mitrovic, S Klanke, and S Vijayakumar. Learning impedance control of antagonistic systems based on stochastic optimization principles. *The International Journal of Robotics Research*, 30(5):556–573, Apr 2011.

[81] Junho Choi, Seonghun Hong, Woosub Lee, and Sungchul Kang;. A variable stiffness joint using leaf springs for robot manipulators. *Robotics and Automation, 2009. ICRA '09. IEEE International Conference on*, pages 4363 – 4368, 2009.

[82] R Schiavi, G Grioli, S Sen, and A Bicchi. VSA-II: a novel prototype of variable stiffness actuator for safe and performing robots interacting with humans. *Robotics and Automation, 2008. ICRA 2008. IEEE International Conference on*, pages 2171 – 2176, 2008.

[83] G Tonietti, R Schiavi, and A Bicchi. Design and control of a variable stiffness actuator for safe and fast physical human/robot interaction. *Robotics and Automation, 2005.*

Nevio Luigi Tagliamonte

ICRA 2005. Proceedings of the 2005 IEEE International Conference on, pages 526 – 531, 2005.

[84] T Morita and S Sugano. Development of 4-DOF manipulator using mechanical impedance adjuster. *Robotics and Automation, 1996. Proceedings., 1996 IEEE International Conference on*, 4:2902 – 2907 vol.4, 1996.

[85] K Hollander, T Sugar, and D Herring. Adjustable robotic tendon using a 'Jack Spring'™. *Rehabilitation Robotics, 2005. ICORR 2005. 9th International Conference on*, pages 113 – 118, 2005.

[86] R Ghorbani and Q Wu. Adjustable stiffness artificial tendons: Conceptual design and energetics study in bipedal walking robots. *Mechanism and Machine Theory*, 44(1):140–161, Jan 2009.

[87] R Van Ham, B Vanderborght, M Van Damme, B Verrelst, and D Lefeber. MACCEPA: the actuator with adaptable compliance for dynamic walking bipeds. *Climbing and Walking Robots*, pages 759–766, 2006.

[88] B Vanderborght, N Tsagarakis, C Semini, R Van Ham, and D Caldwell. MACCEPA 2.0: Adjustable compliant actuator with stiffening characteristic for energy efficient hopping. *Robotics and Automation, 2009. ICRA '09. IEEE International Conference on*, pages 544 – 549, 2009.

[89] R Van Ham, B Vanderborght, M Van Damme, V Grosu, and D Lefeber. Maccepa, the mechanically adjustable compliance and controllable equilibrium position actuator: different design options. *Robotics and Automation (ICRA), 2011 IEEE International Conference on, Workshop on Biologically-Inspired Actuation*, 2011.

[90] Byeong-Sang Kim and Jae-Bok Song. Hybrid dual actuator unit: A design of a variable stiffness actuator based on an adjustable moment arm mechanism. *Robotics and Automation (ICRA), 2010 IEEE International Conference on*, pages 1655 – 1660, 2010.

[91] N Tsagarikis, A Jafari, and D Caldwell. A novel variable stiffness actuator: Minimizing the energy requirements for the stiffness regulation. *Engineering in Medicine and Biology Society (EMBC), 2010 Annual International Conference of the IEEE*, pages 1275 – 1278, 2010.

[92] R Ghorbani and W Qiong. Environmental-interaction robotic systems: Compliant actuation approach. *International Journal of Advanced Robotic Systems*, 4(1):81–92, Jan 2007.

Nevio Luigi Tagliamonte

[93] N G Tsagarakis A Jafari and D G Caldwell. AwAS-II: A new actuator with adjustable stiffness based on the novel principle of adaptable pivot point and variable lever ratio. *Robotics and Automation (ICRA), 2011 IEEE International Conference on*, pages 4638 – 4643, 2011.

[94] H V Quy, L Aryananda, F I Sheikh, F Casanova, and R Pfeifer. A novel mechanism for varying stiffness via changing transmission angle. *Robotics and Automation (ICRA), 2011 IEEE International Conference on*, pages 5076 – 5081, 2011.

[95] M Laffranchi, N.G Tsagarakis, and D.G Caldwell. A variable physical damping actuator (VPDA) for compliant robotic joints. *Robotics and Automation (ICRA), 2010 IEEE International Conference on*, pages 1668–1674, 2010.

[96] Jianjun Li, Dewen Jin, Xiaoning Zhang, Jichuan Zhang, and W Gruver. An electrorheological fluid damper for robots. *Robotics and Automation, 1995. Proceedings., 1995 IEEE International Conference on*, 3:2631 – 2636 vol.3, 1995.

[97] N Takesue, Guoguang Zhang, M Sakaguchi, Junji Furusho, and Y Kiyosawa. Development and analysis of actuator with ER damper. *Robotics and Automation, 2000. Proceedings. ICRA '00. IEEE International Conference on*, 2:1328 – 1333 vol.2, 2000.

[98] M Unsal, C Niezrecki, and C Crane. Two semi-active approaches for vibration isolation: piezoelectric friction damper and magnetorheological damper. *Mechatronics, 2004. ICM '04. Proceedings of the IEEE International Conference on*, pages 60 – 65, 2004.

[99] S Yoon, S Kang, S Kim, Y Kim, M Kim, and C Lee. Safe arm with MR-based passive compliant joints and visco-elastic covering for service robot applications. *Intelligent Robots and Systems, 2003. (IROS 2003). Proceedings. 2003 IEEE/RSJ International Conference on*, 3:2191 – 2196 vol.3, 2003.

[100] A S Shafer and M R Kermani. Design and validation of a magneto-rheological clutch for practical control applications in human-friendly manipulation. *Robotics and Automation (ICRA), 2011 IEEE International Conference on*, pages 4266 – 4271, 2011.

[101] R Farris and M Goldfarb. Design of a multi-disc electromechanical modulated dissipator. *Robotics and Automation (ICRA), 2010 IEEE International Conference on*, pages 2189 – 2196, 2010.

[102] N Lauzier and C Gosselin. Series clutch actuators for safe physical human-robot interaction. *Robotics and Automation (ICRA), 2011 IEEE International Conference on*, pages 5401 – 5406, 2011.

Nevio Luigi Tagliamonte

[103] M Laffranchi, N Tsagarakis, and D G Caldwell. A compact compliant actuator (CompAct^{TM}) with variable physical damping. *Robotics and Automation (ICRA), 2011 IEEE International Conference on*, pages 4644 – 4650, 2011.

[104] Y Ikegami, K Nagai, R Loureiro, and W Harwin. Design of redundant drive joint with adjustable stiffness and damping mechanism to improve joint admittance. *Rehabilitation Robotics, 2009. ICORR 2009. IEEE International Conference on*, pages 202 – 210, 2009.

[105] L Visser, R Carloni, R Unal, and S Stramigioli. Modeling and design of energy efficient variable stiffness actuators. *Robotics and Automation (ICRA), 2010 IEEE International Conference on*, pages 3273 – 3278, 2010.

[106] C Mavroidis, J Nikitczuk, B Weinberg, G Danaher, K Jensen, P Pelletier, J Prugnarola, R Stuart, R Arango, and M Leahey. Smart portable rehabilitation devices. *Journal of NeuroEngineering and Rehabilitation*, 2(1):18, 2005.

[107] Jinzhou Chen and Wei-Hsin Liao;. A leg exoskeleton utilizing a magnetorheological actuator. *Robotics and Biomimetics, 2006. ROBIO '06. IEEE International Conference on*, pages 824 – 829, 2006.

[108] T Kikuchi, S Tanida, K Otsuki, T Yasuda, and J Furusho. Development of third-generation intelligently controllable ankle-foot orthosis with compact MR fluid brake. *Robotics and Automation (ICRA), 2010 IEEE International Conference on*, pages 2209 – 2214, 2010.

[109] G Carpino, D Accoto, M Di Palo, N L Tagliamonte, F Sergi, and E Guglielmelli. Design of a rotary passive viscoelastic joint for wearable robots. *IEEE International Conference on Rehabilitation Robotics*, 2011.

[110] Ching-Ping Chou and B Hannaford. Measurement and modeling of McKibben pneumatic artificial muscles. *Robotics and Automation, IEEE Transactions on*, 12(1):90 – 102, 1996.

[111] F Daerden and D Lefeber. The concept and design of pleated pneumatic artificial muscles. *International Journal of Fluid Power*, 2(3):41–50, 2001.

[112] F Vitale, D Accoto, L Turchetti, S Indini, M Annesini, and E Guglielmelli. Low-temperature H_2O_2-powered actuators for biorobotics: Thermodynamic and kinetic

Nevio Luigi Tagliamonte

analysis. *Robotics and Automation (ICRA), 2010 IEEE International Conference on*, pages 2197 – 2202, 2010.

[113] K Fite, T Withrow, Xiangrong Shen, K Wait, J Mitchell, and M Goldfarb. A gas-actuated anthropomorphic prosthesis for transhumeral amputees. *Robotics, IEEE Transactions on*, 24(1):159 – 169, 2008.

[114] S.K Au, J Weber, and H Herr. Powered ankle–foot prosthesis improves walking metabolic economy. *IEEE Trans. Robot.*, 25(1):51–66, Feb 2009.

[115] D P Ferris, K Liang, and C.T Farley. Runners adjust leg stiffness for thier first step on a new running surface. *Journal of Biomechanics*, pages 787–794, Jun 1999.

[116] Hiroaki Hobara, Koh Inoue, Tetsuro Muraoka, Kohei Omuro, Masanori Sakamoto, and Kazuyuki Kanosue. Leg stiffness adjustment for a range of hopping frequencies in humans. *Journal of Biomechanics*, 43(3):506–511, Feb 2010.

[117] P L Gribble, L I Mullin, N Cothros, and A Mattar. Role of cocontraction in arm movement accuracy. *Journal of Neurophysiology*, pages 2396–2405, 2003.

[118] Kyu-Jin Cho and H Asada. Architecture design of a multiaxis cellular actuator array using segmented binary control of shape memory alloy. *Robotics, IEEE Transactions on*, 22(4):831 – 843, 2006.

[119] H Horiguchi, K Imagawa, T Hoshino, Y Akiyama, and K Morishima. Fabrication and evaluation of reconstructed cardiac tissue and its application to bio-actuated microdevices. *NanoBioscience, IEEE Transactions on*, 8(4):349 – 355, 2009.

[120] A. W Feinberg, A Feigel, S. S Shevkoplyas, S Sheehy, G. M Whitesides, and K. K Parker. Muscular thin films for building actuators and powering devices. *Science*, 317(5843):1366–1370, Sep 2007.

[121] L Lemmer and B Kiss. Modeling, identification, and control of harmonic drives for mobile vehicles. *EEE International Conference on Mechatronics*, pages 369–374, 2006.

[122] Heike Vallery, Ralf Ekkelenkamp, Herman van der Kooij, and Martin Buss. Passive and accurate torque control of series elastic actuators. In *IROS*, pages 3534–3538. IEEE, 2007.

[123] H Vallery, J Veneman, E van Asseldonk, R Ekkelenkamp, M Buss, and H van der Kooij. Compliant actuation of rehabilitation robots: benefits and limitations of series elastic actuators. *IEEE Robotics & Automation Magazine*, 15(3):60–69, 2008.

Nevio Luigi Tagliamonte

[124] G Pratt. Legged robots at MIT: what's new since raibert? *IEEE Robotics & Automation Magazine*, 7(3):15 – 19, 2000.

[125] James Oat JudgeRoy, B. Davis, and Sylvia Ounpuu. Step length reductions in advanced age: The role of ankle and hip kinetics. *The Journals of Gerontology Series A: Biological Sciences and Medical Sciences*, 51(6):303–312, 1996.

[126] M. Patricia Murray, Ross C. Kory, and Bertha H. Clarkson. Walking patterns in healthy old men. *Journal of Gerontology*, 24(2):169–178, 1969.

[127] J. Rose and J.G. Gamble. *Human Walking*. Eds. Lippincott USA, 2005.

[128] Hylton B. Menz, Stephen R. Lord, and Richard C. Fitzpatrick. Age-related differences in walking stability. *Age and Ageing*, 32(2):137–142, 2003.

[129] D.A. Winter. *Biomechanics and Motor Control of Human Movement*. Wiley, 2009.

[130] J F Veneman, R Ekkelenkamp, R Kruidhof, F van der Helm, and H van der Kooij. A series elastic- and bowden-cable-based actuation system for use as torque actuator in exoskeleton-type robots. *The International Journal of Robotics Research*, 25(3):261–281, 2006.

[131] K Kong, J Bae, and M Tomizuka. A compact rotary series elastic actuator for knee joint assistive system. *Robotics and Automation (ICRA), 2010 IEEE International Conference on*, pages 2940–2945, 2010.

[132] Li-Qun Zhang, Gordon Nuber, Jesse Butler, Mark Bowen, and William Z. Rymer. In vivo human knee joint dynamic properties as functions of muscle contraction and joint position. *Journal of Biomechanics*, 31(1):71 – 76, 1998.

[133] Jonathon W. Sensinger and Richard F. ff. Weir. Improvements to series elastic actuators. In *Mechatronic and Embedded Systems and Applications, Proceedings of the 2nd IEEE/ASME International Conference on*, pages 1 –7, aug. 2006.

[134] R. Pintelon and J. Schoukens. *System identification: a frequency domain approach*. IEEE Press, 2001.

[135] G Wyeth. Demonstrating the safety and performance of a velocity sourced series elastic actuator. *Proc. IEEE International Conference on Robotics and Automation*, pages 3642 – 3647, 2008.

Nevio Luigi Tagliamonte

[136] Li-Qun Zhang, Gordon Nuber, Jesse Butler, Mark Bowen, and William Z. Rymer. In vivo human knee joint dynamic properties as functions of muscle contraction and joint position. *Journal of Biomechanics*, 31(1):71 – 76, 1997.

[137] Ian D. Loram and Martin Lakie. Direct measurement of human ankle stiffness during quiet standing: the intrinsic mechanical stiffness is insufficient for stability. *The Journal of Physiology*, 545(3):1041–1053, 2002.

[138] Lorenzo Sciavicco and Bruno Siciliano. *Modelling and Control of Robot Manipulators (Advanced Textbooks in Control and Signal Processing)*. Springer, 2nd edition, January 2005.

Nevio Luigi Tagliamonte